Combining Geophysics and Basin Modeling to Develop a Thermal Model in an Offshore Block, Mexican Gulf of Mexico

Constraining Source Rock Maturity Through OAT Sensitivity Analyses of Key Inputs

Company Supervisors: Susan Weniger & Hussein Ali // Wintershall Dea GmbH

Academic Supervisors: Florian Wellmann (RWTH Aachen) & Deyan Draganov (TU Delft) // IDEA League

Mahad Nadeem Janjua

MSc Thesis Project

Summer Semester 2021

Confidentiality Declaration

With my signature, I certify that this thesis report has been structured and written in alignment with the confidentiality requirements of Wintershall Dea GmbH. This includes retaining the secrecy of the company's information, such as:

1. Name(s) of licensed concession(s).

2. Location(s) of the concession(s).

3. Locations of the available dataset(s).

4. Depths of the (subsurface) data from available dataset(s).

5. Depths of the (subsurface) models constructed based on available dataset(s).

Any resemblance of the assigned arbitrary labels to other licensed concessions or leads belonging to either Wintershall Dea GmbH or any other company is completely coincidental.

Name: **Mahad Nadeem Janjua**

Signature   Place, Date

Abstract

The recent discovery of the *Zama* field in offshore Sureste Basin in the southern Gulf of Mexico has piqued interest in the Mexican petroleum industry regarding the hydrocarbon potential within the region. In this study, a deposition-only thermal model was developed in an area of interest (AOI) in this region. Using structural input obtained from seismic interpretation conducted in Petrel$^{©}$, the model was constructed and simulated in PetroMod$^{©}$ to acquire initial estimates of the maturities of the Tithonian J100 source rock in the AOI in terms of the maturity parameters Vitrinite Reflectance ($\%R_0$) and Transformation Ratio (TR). A *one-at-a-time* (OAT) sensitivity analysis approach was also undertaken to assess the impact of uncertainties in some inputs in isolation on the output maturity in order to identify key uncertain input parameters.

Based on the modelling results, at the C-1 well location of interest within the AOI, the source rock was simulated to be within the wet gas generation window based on simulated $\%R_0$ values in the present, having emerged into oil window between 41 - 27 Ma (late Eocene-Oligocene) and into the wet gas window between 6 - 0.5 Ma (late Miocene-Pleistocene). Across the wider AOI, present-day $\%R_0$ values indicate the predominant presence of late oil to wet gas generation windows, with most of the source rock across the AOI having emerged into the oil generation window between 23 Ma and 11.6 Ma (early to middle Miocene). The highest uncertainties in simulated $\%R_0$ values were associated with uncertainties in the Bajocian (J60) autochtonous salt sequence thickness distribution, and with the maturity models used for model simulation.

At the C-1 well location, TR values of 95 % to near 100 % in the present indicate that most of the kerogen (source rock organic matter) has already been converted into hydrocarbons, with kerogen conversion initiated between 55 - 48 Ma at the location. Across the wider AOI, average present-day TR values in the range of 81 - 97 % were simulated. The highest uncertainties in simulated TR values were also associated with uncertainties in the Bajocian (J60) autochtonous salt sequence thickness distribution, and with the source rock maturation kinetics input used for model simulation.

The timing of maturation of the J100 source rock at the C-1 well location - assumed to have been constrained by the OAT sensitivity analyses results for simplicity - in relation to the timing of other petroleum system elements and processes indicated by literature, suggests that hydrocarbon accumulations charged from the Tithonian source rock in the reservoir intervals in the well vicinity are possible i.e. presence of hydrocarbon accumulations cannot be ruled out based only on maturation timing considerations.

Acknowledgments

Contents

Chapter 1

Introduction

Preface I - Study Motivation and Relevance

The recent discovery of the *Zama* field, the world's largest offshore shallow water discovery in the past 20 years (Garduno, 2020), in 2017 in offshore *Sureste Basin* in the southern Gulf of Mexico has piqued further interest in the petroleum industry in Mexico regarding the hydrocarbon potential within the region for newer plays and profitable prospects. To this end, new frontier exploration areas in the region are now the subject of numerous industry projects and studies to understand various aspects of the subsurface petroleum system(s) that are yet unknown in order to minimize risks during later drilling for petroleum discoveries. This is one such study, which is focused on developing an understanding of the the maturities of a source rock of interest in a specific area of interest in the basin, since no such publicly available prior work has been conducted in the area.

The term "petroleum system" is an encompassing term that refers to the various petroleum system elements, such as source, reservoirs, cap/seal, and overburden rocks; the term also encompasses the interrelation of the petroleum system elements through the various petroleum system processes, such as hydrocarbon generation, migration, trap formation and accumulation (Littke et al., 2008; Magoon & Dow, 1994). The interaction of these aforementioned elements and processes needs to occur favorably in time and space such that hydrocarbon accumulations can successfully occur (Al-Hajeri et al., 2009). A source rock has organic matter embedded within it which undergoes chemical alterations to generate hydrocarbons (oil and/or gas) when exposed to elevated temperatures. This alteration process, commonly referred to as *cracking*, leads to the *maturation* of the source rock as it gets depleted over time of its hydrocarbon generation potential. The extent of source rock maturity can be measured through various maturity indicators. One such indicator is *Vitrinite Reflectance* ($\%R_0$). Vitrinite is a common organic substance found in sedimentary rocks, which in simple terms exhibits an increase in reflectance of incident light on its surface as it is exposed to elevated temperatures (Teichmüller, 1989). Therefore, since $\%R_0$ is "generally correlated with source rock maturation and the stage of oil and gas generation" (Hantschel & Kauerauf, 2009), it can be used as a reliable source rock maturity indicator (Dow, 1977). Similarly, *Transformation Ratio* (TR) is another key maturity indicator which describes the ratio of organic matter (also known as *kerogen*) that has been cracked/converted to hydrocarbons upon heating to the total initial amount of organic matter (Waples & Tobey, 2017). Such source rock maturity indications are of critical importance since:

1. They can serve as indicators for the type(s) of hydrocarbons being generated (oil and/or gas), if any, at various points in time including the present. This is possible with $\%R_0$.

2. In the broader context, they allow for placing constraints on the possibility of oil and/or gas accumulations by limiting the temporal and spatial windows within which other petroleum system elements and processes need to have emerged and occurred, respectively.

Estimating the spatial distribution of maturity through time is, however, not a straightforward process for a number of reasons. Firstly, in order to acquire *true* source maturity assessments, values for various maturity indicators need to be attained via geochemical analyses of core samples obtained from drilled wells. In frontier exploration areas, however, well and core data is often sparsely available and at sparse depth intervals, the latter not always overlapping with source rock depth intervals. This entails that a true picture of the spatial distribution of the (present-day) maturity values is very difficult to obtain while relying solely on the approach described. Secondly, from present-day maturity indicator values alone and without the aid of any modelling studies, it is not possible to extract any information regarding the timing of maturation, which is of critical importance, as discussed above.

To this end, a thermal modelling approach is commonly undertaken in industry operations, which essentially is an

aim-specific branch of basin and petroleum systems modelling (Al-Hajeri et al., 2009) and deals with reconstructing the thermal histories over geological timescales of the various stratigraphic layers of a sedimentary basin. This approach is the focus of Preface II.

Preface II - Thermal Modelling General Workflow

While the specific details of the thermal modelling scheme followed for this study are the focus of chapter 2, it suffices here to provide a brief introduction into the workflow of a general thermal modelling scheme with the principle aim of contextualizing the information provided later in this chapter; readers interested in further details regarding thermal modelling - or basin and petroleum system modelling in general - are referred to literature works such as Hantschel & Kauerauf (2009) and (Al-Hajeri et al., 2009).

Firstly, a thermal model requires a structural input for subsurface representation in the present-day, which is followed by property assignments to the delineated layers, such as age information, lithology, source rock maturation kinetics etc. The subsurface structural input can be acquired through interpretation of processed geophysical data e.g. processed (2D/3D) reflection seismic, gravity, electromagnetic data etc. (Al-Hajeri et al., 2009). Property assignment can be sourced from field data (e.g. well log data, core analysis data etc.) or literature studies (typically in the absence of field data) (Hantschel & Kauerauf, 2009). Such a model is then simulated through time to account for various geological processes - such as sediment deposition, burial, compaction etc. - and their corresponding effects on rock properties - such as porosities, thermal conductivities etc. Thermal conditions to which the model is exposed to through time during such a simulation are governed by (thermal) boundary conditions, the values for which in geologically realistic scenarios often vary through time (Hantschel & Kauerauf, 2009). Values for various thermal parameters of interest (including maturity indicators) at different time steps of interest are then calculated based on these simulations.

Commonly, the input parameters used for such a model are uncertain and involve a number of assumptions (Al-Hajeri et al., 2009); to account for this, *sensitivity analyses* can be conducted to understand the impact of possible variations in the values of these input parameters on the output parameter(s) of interest (Wainwright et al., 2014). This is useful to identify key input parameters that contribute largest uncertainties to modelling results. A number of approaches are possible for such analyses, and the approach undertaken for this study in particular is one of the focuses of chapter 2.

With the context and motivation behind this study explained, and a brief description regarding the thermal modelling approach provided, the following sections and associated subsections of the chapter will introduce the necessary background information and prior/available input data for the thermal modelling scheme for this study. In section 1.1, the Sureste Basin is introduced as the basin hosting the area of interest. In the branching subsections, brief descriptions are provided for the main source rock of interest (central to this study) as well as for the relevant tectonic events and tectono-stratigraphic sequences. Available data necessary for the modelling scheme for this study is the subject of the proceeding section 1.2. Lastly, the chapter is concluded with an outline of the specific objectives of this study in section 1.3.

1.1   The Sureste Basin

Geographic Location and Spatial Extent   The *Sureste Basin*, meaning Southeast Basin, is located in the southern Gulf of Mexico (GOM) region and forms the adjoining southern part of United States GOM shelf-slope basin known as the *Central Louann Salt Basin*. In the context of this study, the Sureste Basin is defined following its widest understood spatial extent based on studies such as Shann et al. (2020). This includes both onshore and offshore areas of southern Mexico (see figure 1.1) and covers sub-basins identified in numerous literature studies as individual basins, such as the *Campeche Salt Basin* and *Yucatán Salt Basin* (Hudec et al., 2013; Hudec & Norton, 2019), as well as the *Macuspana*, *Comalcalco*, *Pilar* and *Pescadores* sub-basins (Ambrose et al., 2003; Davison et al., 2021; Shann et al., 2020). The Sureste Basin also encompasses subdivided regions published in literature based on distinct geological features, including the *Pilar Reforma Akal Trend* (e.g. see figure 1 in Davison et al. (2021)) which separates the Comalcalco and Macuspana sub-basins. According to Shann et al. (2020), defining the spatial extent of the Sureste Basin as such is warranted, since a common set of geological formation and petroleum systems can be traced across the basin, which in turn is linked to the fact that the entire basin area shares a common tectonic evolution scheme. Explicit definition of the Sureste Basin in terms of naming is also necessary at the outset owing to the fact that there exists a well known problem in the on- and offshore Gulf of Mexico regions regarding an abundance of published names for basins and geological features, already pointed out early on in Salvador (1991). Even for the Sureste Basin as defined in this study, though the name Sureste Basin has recently been adopted as the standard for the basin by Pemex (Mexican state-owned Petroleum company) and Comisión Nacional de Hidrocarburos (National Hydrocarbons Commmission) in Mexico (Davison et al., 2021), a number of alternative names have been previously used in published
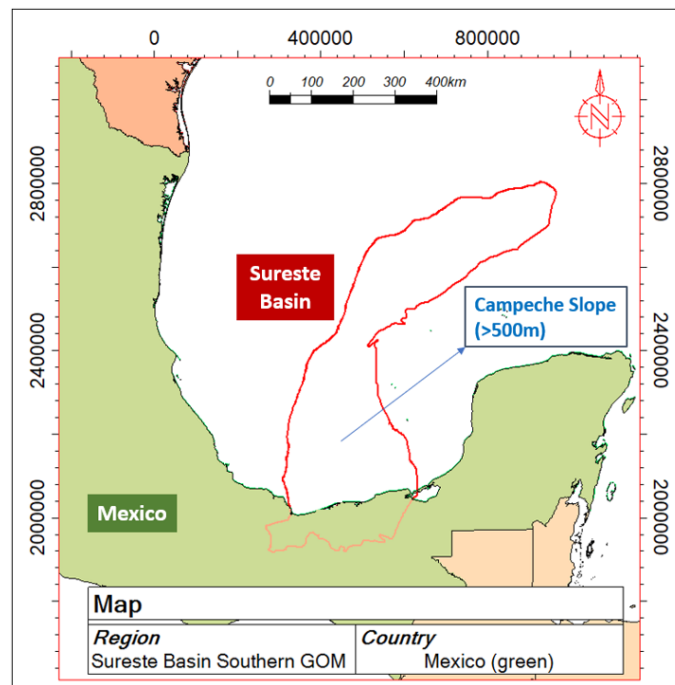
Figure 1.1: **Geographic Location and Spatial Extent of the Sureste Basin**. The Sureste Basin is outlined in red. The Campeche slope is the general area in the offshore part of the basin where present-day water depths exceed 500 m.

literature, such as *Isthmian Salt Basin* Hudec et al. (2013); Hudec & Norton (2019), *Cuenca de Campeche* (Campeche Basin) and *Cuenca Salina* (Davison et al., 2021).

Sureste Basin - A Super Basin   The Sureste Basin is widely regarded as one of the most prolific super basins in the world. According to D. Brown (2018), 230 documented discoveries in regions of the basin with less 200 m of water depth to date have yielded approximately 55 billion barrels of oil equivalent (boe), of which 15 billion boe are accounted for by the supergiant *Cantarell* oil field discovered in 1979. In that context, the basin's offshore regions potentially present areas of considerable petroleum potential still to be tested, especially considering the fact that less than 15 wells have been drilled so far in water depths > 500 m in the *Campeche* slope area of the basin (Shann et al., 2020).

The term *super basin* has been suggested for sedimentary basins with high hydrocarbon potential. More specifically, they are characterized by at least 5 billion boe cumulative production and at least 5 billion boe remaining recoverable resources, as well as by geological and non-geological factors such as the presence of at least two source rocks, stacked reservoir formations, a regional seal or a series of seals, readily available exploration and production infrastructure, established oil field service sectors, sufficient volumes of data, and open access to markets for supply and distribution (Fryklund & Stark, 2020; Whaley, 2019). Shann et al. (2020) argued for the qualification of the Sureste Basin as a super basin based on all aforementioned criteria. The study placed emphasis on the basin's endowment with multiple source rocks including the organic-rich and high potential Late Jurassic (Tithonian age) Edzna Formation (see subsection 1.1.3 for more details), pointed to the presence of at least 10 stacked potential reservoir-seal pairs that each average more than 100 m thickness and can be traced across the basin, and highlighted the presence of allochtonous salt bodies leading to high structural complexity, which in turn leads to a wide trap diversity in the basin. From a non-geological perspective, considerable data from numerous onshore and shallow offshore wells coupled with the benefits attained from analogues from the highly explored United States GOM shelf-slope basin provide a solid foundation for geoscientific predictions in untested regions and structures (Shann et al., 2020).

1.1.1   Study Area

The area of interest (AOI) for this study is located offshore in the Campeche slope of the Sureste Basin in the eastern portion of block X, a licensed area for Wintershall Dea GmbH and partners. The total area of the AOI is *ca.* 860 km^2. This area is shown on figure 1.2 as the blue highlighted area inside the larger block X area (outlined in orange).
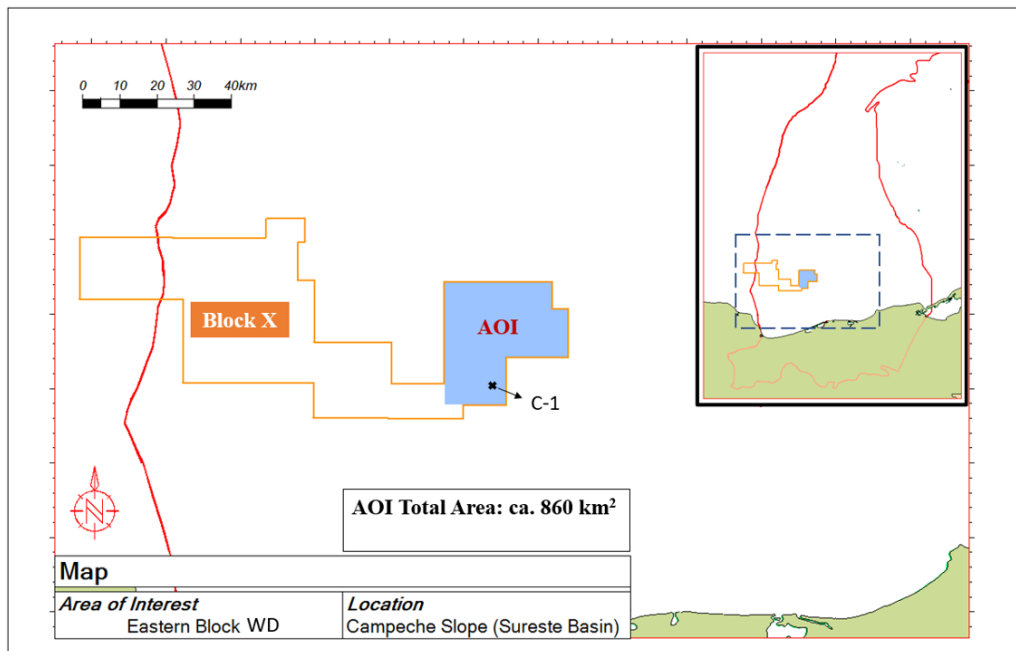
Figure 1.2: **Area of Interest (AOI) for this study**. The AOI is highlighted in blue as the eastern portion of block X located on the Campeche slope in the offshore part of Sureste Basin.

1.1.2   Key Tectonic Events and Basin Formation

The Gulf of Mexico has undergone complex tectonic evolution, with a number of regional tectonic events impacting the structural framework of the basin. Detailed descriptions and discussions of the key tectonic and other regional deformation events relevant for the Sureste Basin have been made in a number of literature studies, such as Salvador (1987), J. L. Pindell (1993), Oviedo-Perez (1996), J. L. Pindell & Kennan (2009), Kneller & Johnson (2011), and Comisión Nacional de Hidrocarburos (2019) to name a few. Understanding these events is not only critical for understanding the present-day structural settings in the wider basin area and in particular the AOI, but also for establishing constraints on the thermal history in the AOI (see subsection 2.2.5). The events detailed in this subsection are sourced from the aforementioned studies and the cited studies therein only, unless otherwise explicitly stated.

Rifting Events   The first event of relevance was an active rifting event initiated in the Triassic - approximately 240 Ma according to Davison et al. (2021) - which was related to the breakup of the Western Equatorial Pangaea, during which the North American plate separated from the South American plate (the Yucatán block included) and the African plate (Buffler & Sawyer, 1985). As a result of continental rifting, extensive graben structures developed that provided the accommodation space for the formation of the Sureste Basin. The reported duration of this rifting event has shown discrepancies in published studies, and varying end rift ages of ca. 170 Ma (Bajocian) (Davison et al., 2021), ca. 163 Ma (Callovian) (R. J. Padilla y Sánchez, 2007; Hudec et al., 2013) and ca. 152 Ma (Kimmeridgian) (Shann et al., 2020) have been suggested. Regardless of these discrepancies, the total duration of the rifting event can still be considered an unusually long duration for active rifting (Davison et al., 2021).

A second rifting event associated with seafloor spreading in the GOM initiated in the Oxfordian (D. E. Bird et al., 2005; Nguyen & Mann, 2016); this led to the development of conjugated passive margins in the northern and southern parts of the GOM from the large initial sag basin, as the generation of oceanic crust began in the central GOM. The seafloor spreading was tied to anticlockwise rotation of the Yucatán block (see figure 1.5) of approximately 39 ° from its pre-rift position (R. Padilla y Sánchez, 2014), and this occurred along two rotation poles (see figure 1 in Shann et al. (2020)). J. L. Pindell & Kennan (2009) ascertained the end-rift age of this event to be Barremian (approx. 130 Ma), although an alternative age of approx. 140 Ma has also been suggested (Davison et al., 2021). While this rifting event is of critical importance in terms of its effect on crustal and thermal evolution in the central GOM, the AOI was not impacted by the seafloor spreading or the associated crustal thinning. The oceanic crust generation occurred outside of the Sureste Basin limits (see figures 1.3 and 1.5), whereas the AOI lies well within these limits (figure 1.2). Once rifting ceased, the tectonic conditions remained stable in the southern GOM during the Early and Late Cretaceous period, and thermal subsidence that had already ensued in the Late Jurassic-Early Cretaceous continued in the basin till the Late Cretaceous (Cenomanian) (Aquino-López, 2004; Snedden et al., 2014).
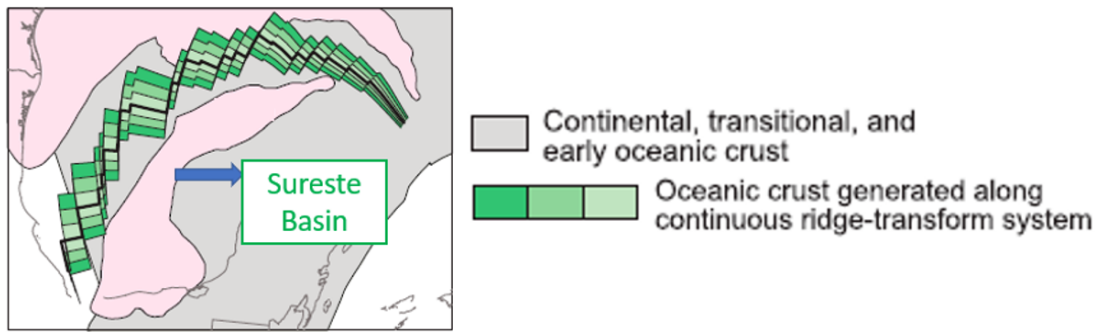
Figure 1.3: **Limits of the oceanic and transitional crust generated during the seafloor spreading in the GOM**. The AOI can be understood to exist solely on top of continental crust.
Modified from: Hudec & Norton (2019).

Compressional Events   The first key compressional event was the *Laramide* orogeny that occurred in west-central part of the United States from approximately 75 Ma to 35 Ma (P. Bird, 1998), though the precise ages and duration of the orogenic event are still in dispute; start and end ages in the ranges of 95 - 70 Ma and 55 - 35 Ma, respectively, have been proposed in available literature (English & Johnston, 2004; Shann et al., 2020). According to the Comisión Nacional de Hidrocarburos (2019), the progression of deformation (predominantly oriented in the north-south direction) associated with this event into the Sureste Basin is detectable through clear structural and stratigraphic markers in the Eocene, such as high-angle reverse/thrust faults, strike-slip faults, and observable thickness variations in the depositional packages in the region (see subsection 2.1.3).

According to J. Pindell & Miranda (2011), there was a lack of tectonic activity in the basin from the Eocene-Oligocene to Early Miocene, subsequent to the deformation associated with the Laramide orogeny. Soon after, the relatively short-lived *Chiapaneco* orogeny event in the Middle Miocene occurred which was associated with the formation of Chiapas folded belt (south of the Sureste Basin), which is arguably the most important compressional event in the Sureste Basin. The compressional deformation from the orogenic event can be observed widely in the basin as extensive folding oriented predominantly in the northwest-southeast direction that caused widespread vertical stacking of formations through extensive thrust faulting (see figure 1.4). This deformation also resulted in local erosional unconformities and mobilized the extensive vertical migration of the Jurassic salt to form allochtonous salt bodies (see subsection 1.1.3). Details regarding the tectonic events leading up to the orogeny are well summarized in Davison et al. (2021). Shann et al. (2020) stated that the duration of this event can be relatively precisely estimated to be of the Serravallian age (13.8 Ma to 11.6 Ma) of the Middle Miocene through biostratigraphic ties.
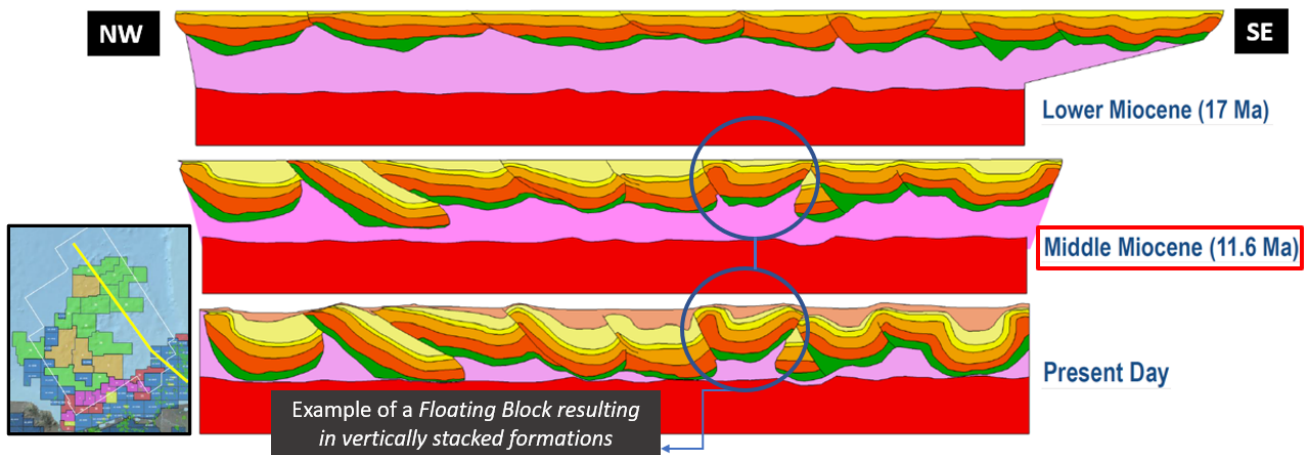
Figure 1.4: **Vertical stacking and *floating block* emergence with the Middle Miocene Chiapaneco event.** Structural evolution of a northwest-southeast trending 2D cross-section from the Lower Miocene to the present day of a 2D cross-section in the Campeche slope shows that the Chiapaneco event resulted in extensive folding and thrust faulting, resulting in vertical stacking and *floating block* formation. The evolution shown is based on structural palinspatic restoration with salt movement considered.
Modified from: Snyder & Ysaccis (2018).

1.1.3   Key Tectono-Stratigraphic Sequences

A stratigraphic sub-division of the Mesozoic-Cenozoic age basin fill as laid out by Shann et al. (2020) will be followed for the purpose of this study. Such a sub-division separates the sedimentary fill into a set of tectono-sequences that can be distinctly identified in on- and offshore seismic data based on structural and stratigraphic indicators that can be linked to the tectonic phase impacting the basin at the time of deposition. To this end, the alphanumerical nomenclature adopted by Shann et al. (2020) will be used for this study as well. The aim of this subsection is to introduce the 16 tectono-sequences of interest from oldest to youngest in terms of their facies distribution and general age fit. Brief descriptions of paleo-depositional environments are included for their relevance in placing constraints on the paleowater depths in their respective paleo-depositional environments. Limited descriptions regarding geological processes leading to sourcing of sediments are provided since this is beyond the scope of this study; interested readers are encouraged to read cited studies.

Triassic-Lower Jurassic Clastics - J50 (Subsalt Sequence)   The deposition of the J50 sequence coincided with the initial breakup of the Western Equatorial Pangaea. Facies information for this sequence is largely derived from onshore outcrops and from a few wells drilled onshore, since the small number of wells drilled offshore whose results are publicly available have not penetrated this sequence (Rodríguez del Ángel, 2012). This sequence is expected to be dominated by sand-prone red beds (Perez Gutierrez, 2007; Shann et al., 2020), and was likely deposited in a terrestrial environment since paleogeographic reconstructions constructed by R. J. Padilla y Sánchez (2007) show that the present-day offshore regions of the Sureste Basin were likely not submerged underwater during the Triassic-Lower Jurassic (see figure 1 in the appendix).

Middle Jurassic Salt - J60   Tectonic/plate restorations in the GOM region suggest that the J60 salt sequence was widely deposited as a single salt body (Hudec & Norton, 2019) during the Pangaean continental breakup. During this time, the Pacific ocean transgressed into the GOM region and occupied wide regions with hypersaline water. With minimal circulation, extensive evaporite deposition occurred (Perez Gutierrez, 2007) in the Bajocian age which was dominated by halite (Davison et al., 2021). As the seafloor spreading event initiated, the evaporite basin separated into what are presently known as the Central Louann Salt Basin and the Sureste Basin. See figure 1.5 for a visual representation of this evolution. It is important to note that until recently, J60 salt was thought to be of Callovian age; this was only recently re-dated to Bajocian by J. Pindell et al. (2019). It is this J60 salt sequence that formed the widespread allochtonous salt bodies after extensive vertical movement during the Chiapaneco compressional event.
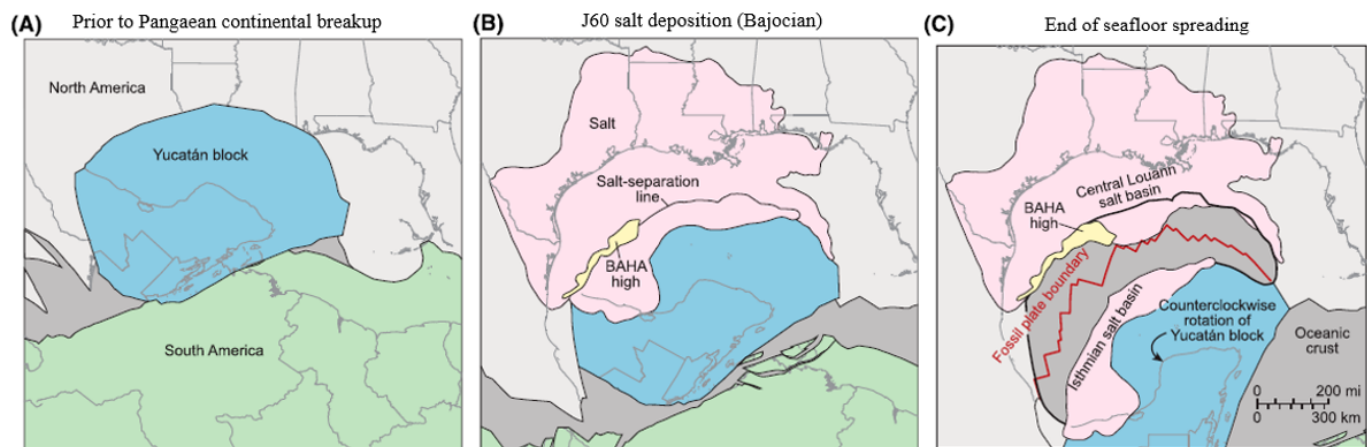
Figure 1.5: **J60 salt deposition and evolution from the Late Triassic to the Middle Jurassic**. Salt deposition occurred in the Bajocian post the Pangaean continental breakup as a single body. The seafloor spreading associated with the Yucatán block anticlockwise rotation proceeded to separate the evaporite basin into what the Central Louann Salt Basin (USA) and the Isthmian Salt Basin or Sureste Basin (Mexico).
Modified from: Hudec & Norton (2019).

Oxfordian Clastics - J80   Angeles-Aquino & Cantu-Chapa (2001) and Cantu-Chapa (2009) provided a detailed lithostratigraphic description of the sedimentary fill from the Oxfordian to the Tithonian age in the Campeche shelf of the Sureste Basin based on 50 exploratory wells drilled and their acquired log responses. What was referred to as the *Ek-Balam* group in the study, the Oxfordian J80 deposits were subdivided into three lithologically well defined sub-units of considerable thicknesses. The lowest sub-unit is comprised of clayey and sandy wackestone to packstone

with intercalated evaporites. The middle sub-unit consists of mudstones and calcareous sandstones. The upper sub-unit is characterized by sandy limestones grading into calcareous sandstone and anhydrite. This is in agreement with the generalized lithology for the Oxfordian reported by Mitra et al. (2006) for the Campeche slope as interbedded limestones, shales and sandstones. The J80 sequence was deposited in a very shallow shelf setting, according to the paleogeographic map constructed by Shann et al. (2020) (see figure 2 in the appendix).

Kimmeridgian Carbonates - J90   Angeles-Aquino & Cantu-Chapa (2001) and Cantu-Chapa (2009) subdivided the Kimmeridgian J90 sequence into four sub-units that alternated between predominantly terrigenous and carbonaceous (marine) lithologies. The lowest sub-unit comprises predominantly of mudstone and sandy shales with sparsely interbedded sandstones, anhydrite and microdolomite. The lower-middle carbonaceous sub-unit consists mainly of dolomite, limestone with isolated interbeds of sandy shales and mudstones. The upper-middle terrigenous sub-unit is characterized by mudstones and sandy shales with interbedded dolomitic limestones and dolomite. Lastly, the upper sub-unit directly underlying the Tithonian J100 sequence consists largely of dolomite and oolitic limestones. This detailed description is in alignment with the more general stratigraphic description for the J90 sequence by Mitra et al. (2006), who suggested that of the two distinct sections of the sequence, the lower is dominated by dolomites and shaly limestones while the upper section comprises of oolitic limestone and dolomitic limestone. According to the paleogeographic map from Shann et al. (2020), the J90 sequence was deposited in a marine basinal setting (see figure 3 in the appendix).

Tithonian Source Rock - J100 (Edzna or Pimienta Formation)   The Tithonian J00 sequence, also commonly referred to as the *Edzna* or *Pimienta* Formation, was characterized by Santamaria Orozco (2000) as an organic-rich source rock with high generation potential (detailed discussion in subsection 1.1.4) that is comprised of shaly and chalky limestone mixed with marl and shale. The lithostratigraphy of the sequence can be subdivided into three distinct sub-units (Angeles-Aquino & Cantu-Chapa, 2001; Cantu-Chapa, 2009). The lowest sub-unit consists of clayey lime mudstones with intervals of black shale. The middle sub-unit, ascertained as the thickest sub-unit of the sequence on average while being the main source rock unit of the J100 sequence (Perez Gutierrez, 2007), is comprised predominantly of sandy black shales interspersed with organic-rich clayey limestones. The upper sub-unit is characterized by clayey lime mudstones. These sub-units are present almost everywhere, and hence have been correlated over long distances in the Campeche shelf where well data is available (Cant-Chapa & Ortuo-Maldonado, 2003). According to Shann et al. (2020), the J100 sequence is characterized by a slope environment at the time of deposition (see J100 paleogeographic map in figure 4 in the appendix). Comisión Nacional de Hidrocarburos (2019) stated that during the Tithonian source rock deposition, the Sureste Basin was tectonically stable enough to support relatively similar lithological features in the sequence throughout the basin.

Lower, Middle and Upper Cretaceous Carbonates - K50, K80 and K100   According to Mitra et al. (2006), the Lower Cretaceous K50 sequence is dominated by shaly limestone and dolomite in the Campeche slope, while the Middle Cretaceous K80 consists primarily of shaly limestone. The Upper Cretaceous K100 sequence shows a stark change in the lithology and is characterized by carbonate breccias (Shann et al., 2020; Mitra et al., 2006). Such brecciation of dolomitized limestones has been attributed widely across published literature studies to the *Chicxulub* meteorite impact (Davison et al., 2021), which has been very precisely dated to have occurred at the present-day coast of the Yucatán block at $66.038 \pm 0.025/0.049\,Ma$ (Renne et al., 2013). This event marked the end of the Cretaceous as well as the extinction of approximately $60\,\%$ of Cretaceous species (Davison et al., 2021). For a very useful visualization of the magnitude of the impact, see Davison (2019). This impact broke down and displaced large volumes of underlying sequences that deposited widely over the GOM (Davison et al., 2021). In terms of the paleo-depositional environments of the K50, K80 and K100 sequences, the paleogeographic maps for Barremian age (Lower Cretaceous) and for Turonian-Maastrichtian age (Middle-Upper Cretaceous) from R. J. Padilla y Sánchez (2007) as well as the paleogeographic map for the K80 Middle Cretaceous sequence from Shann et al. (2020) indicate marine, basinal depositional settings for the duration of the Cretaceous period in the AOI (see figures 5, 6, and 7 in the appendix). According to Comisión Nacional de Hidrocarburos (2019), the general sedimentary regime in the Sureste Basin transitioned from carbonates to siliciclastics at the end of the Upper Cretaceous period, which was associated with the uplift of the *Sierra Madre Oriental* in northeastern Mexico.

Paleocene-Early Eocene Clastics - T20   The T20 sequence, according to Shann et al. (2020) is characterized by a regional shale which is mappable across the Sureste Basin as a very continuous marine flooding event. Mitra et al. (2006) offered a more detailed lithology from the Campeche slope, identifying a breccia layer lying underneath the regional (calcareous) shale. The paleogeographic map from R. J. Padilla y Sánchez (2007) for the beginning of Paleocene age (see figure 8 in the appendix) shows the onset of the regional shale deposition at the slopes of southern,

southeastern, western and north margins of the GOM. From this paleogeographic map, the AOI can be estimated to likely be in a marine, basinal depositional environment.

Upper Eocene Carbonaceous Clastics - T30   The T30 sequence is dominated by calcareous shales with some calcarenites in the Campeche slope (Mitra et al., 2006). In offshore 3D seismic data, the top of this sequence can be identified and interpreted as a strong (peak) reflector (due to the presence of considerable carbonate content) with the aid of other structural and stratigraphic markers associated with the Laramide orogeny (see subsection 1.1.2). The paleo-depositional environment indicated by the paleogeographic map for Late Eocene from R. J. Padilla y Sánchez (2007) shows comparatively lower water depths in the AOI during this time compared to the Paleocene (see figure 9 in the appendix), though the predominant deposition of shales still indicates marine depositional settings.

Oligocene Clastics - T40   The Oligocene T40 sequence marks a notable progressive shift in paleo-depositional environments towards a slope setting, as can be deduced from the paleogeographic map for T40 presented in Shann et al. (2020) (see figure 10 in the appendix). In the AOI, the T40 sequence is estimated to be dominated by turbiditic sand deposits (Shann et al., 2020), particularly to the west-southwest, while calcareous shales and marls are likely also present in the north-northeast portion of the AOI (Mitra et al., 2006; Shann et al., 2020).

Lower Miocene Clastics - T52 (Pre-kinematic)   Clastic sandy sediments continue to dominate the deposited sequences into the Lower Miocene (Shann et al., 2020), as the T52 sequence is characterized by turbiditic deposits. In the offshore 3D seismic dataset in the AOI, the T52 sequence appears as the sequence underlying the syn-kinematic Middle Miocene T55 sequence. It has a relatively constant thickness and its base horizon is characterized by observable distortions in continuity of the seismic reflectors, which is associated with mass transport units (MTUs) (turbiditic channels and downslope fan lobes) according to Shann et al. (2020). Mitra et al. (2006) suggest that in the Campeche slope, the lower segment of T52 sequence likely has carbonate content, suggesting the presence of calcareous shales. According to Valois et al. (2009), what made up the shelf margin of the Sureste Basin in the Lower Miocene is located onshore in the present, indicating slightly deeper paleo-water depths in the Lower Miocene than in the present.

Middle Miocene Clastics - T55 (Syn-kinematic)   Easily identifiable in offshore 3D seismic data as a sequence with clear wedge-like depositional trends, the T55 sequence deposition coincides with the start of extensive vertical salt movement to form allochtonous bodies that pushed out towards the paleo-seafloor Shann et al. (2020). For this reason, the T55 sequence is also referred to as the syn-kinematic sequence. In terms of the lithology of the sequence, sandy sediments dominate the sequence, with some presence of calcareous shale also expected (Mitra et al., 2006).

Upper Miocene Clastics - T50 (Post-kinematic)   The Upper Miocene T50 sequence is the deepest interval for which well data results are publicly available in regions that can be considered representative of the AOI for this study. According to Shann et al. (2020), the Cox-1 and Zama-1 wells drilled to the southwest and northeast to the AOI, respectively, revealed quartz-rich sands in the T50 interval. This is in accordance with general lithologies of interbedded sandstones and shales in the Campeche slope suggested by Mitra et al. (2006). The paleogeographic map from R. J. Padilla y Sánchez (2007) (see figure 11 in the appendix) suggests a slope depositional setting in the AOI, with paleo-water depths inferred to be notably higher compared to the present. What constitute present-day GOM onshore areas in Mexico were submerged under water, thereby prompting shaly and sandy sediment deposition.

Pliocene-Lower Pleistocene and Upper Pleistocene-Holocene Clastics - T90 and T100   The Pliocene-Lower Pleistocene T90 sequence can be inferred from Mitra et al. (2006) to be dominated by siliciclastic sandy shale deposits in the AOI, and such a depositional trend continued towards the present for the deposition of the Upper Pleistocene-Holocene T100 sequence, which consists of fine-grained sandstones with some interstratifications of thin-layered shales and siltstones (Comisión Nacional de Hidrocarburos, 2019; Perez Gutierrez, 2007). The paleo-water depth during the deposition of the T90 and T100 sequences is estimated to be very close to the present-day water depth observed in the AOI, which varies close to 500 m on average, as is visible in offshore 3D seismic data (see figure 1.2.3).

A generalized stratigraphic column for the Campeche shelfal and slope region is shown in figure 1.6. Note that the age of the J60 salt sequence has be modified to represent the recently re-dated age (Bajocian).

1.1.4   Edzna Formation - Tithonian Source Rock

The J100 is widely understood as the most important source rock formation in the Sureste Basin, owing to its wide spatial distribution, relatively greater average thickness compared to other source rocks, favorable properties, and
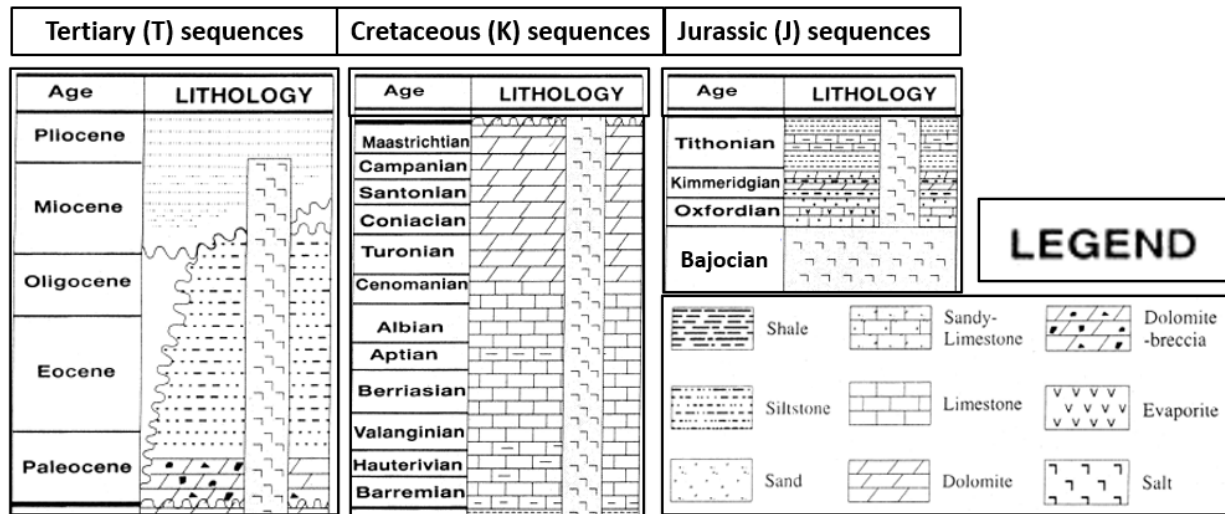
Figure 1.6: **Generalized stratigraphy in the Campeche shelfal and slope regions.**
Modified from: Santamarıa-Orozco et al. (1998).

dominating signature in oil fluids data recorded (Shann et al., 2020). Owing to these factors, the J100 is the source rock of interest for this study (see section 1.3). The three other source rocks in the basin are of the Oxfordian (J80), Early Cretaceous (K50), and Early Miocene (T52) age, and interested readers are encouraged to read further studies e.g. Shann (2021) and Shann et al. (2020).

Thickness Distribution   Cant-Chapa & Ortuo-Maldonado (2003) reported Tithonian source rock thicknesses varying from 62 m to 120 m in the northeastern Campeche shelf area, increasing to 393 m in the central marine area of the Sureste Basin. In deepwater GOM, average thicknesses that have been reported in many studies are in the order of 200 m (Cole et al., 2001, 1999; Shann et al., 2020). These values fall in alignment with a reported Tithonian source rock thickness variation from 50 m to 450 m with an average of 200 m in the Campeche area (Santamaria Orozco, 2000).

Kerogen Type, TOC and HI   The Tithonian source rock has been studied to have Type-IIS kerogen (Santamarıa-Orozco et al., 1998; Clegg et al., 1998). Type-II kerogen is solid, insoluble organic matter stored within sedimentary rocks that has been deposited in marine depositional environments and is oil-prone i.e. upon thermal maturation, this kerogen type predominantly yields oil, though gas expulsion is also expected at higher maturities. Type-IIS kerogen by definition is the same as Type-II kerogen, but with higher sulfur content, which leads to oil generation at lower thermal maturities compared with standard Type-II kerogen (Orr, 1986). Present-day Hydrogen Index (HI) values reported for J100 in deepwater GOM range between 550 - 700 mg/g TOC according to Cole et al. (1999), which is in agreement with values in the range of 500 - 700 mg/g TOC in the Campeche slope and shelf regions (Clegg et al., 1998; Santamarıa-Orozco et al., 1998). Shann et al. (2020) proposed an average HI value of 600 mg/g TOC for the Campeche slope. Average TOC values of around 5 % have been suggested in literature studies (Jarvie & Smyth, 2016; Cole et al., 1999, 2001). Shann et al. (2020) suggested that TOC higher than 5 % are likely in the Campeche slope, a suggestion agreed with by Jarvie & Smyth (2016), who reported average TOC values as high as 8 - 9 % for the middle sub-unit of the formation.

1.2   Available Data For Study

1.2.1   Offshore 3D Seismic Dataset

For this study, a 3D offshore *Wide Azimuth* (WAZ) seismic dataset was available. This post-stack dataset had been pre-stack depth migrated (PreSDM) with *Reverse Time Migration* (RTM). The dataset covered a total surveyed area of approximately 20800 km², with inline and crossline (x-line) lengths of 140.9 km and 147.6 km, respectively. Both the inline and x-line intervals for the survey design were planned at 25 m. The total recording time, equalling the *Two-way Traveltime* (TWT), of 10 s was set with a sampling interval of 4 ms, which translated to a surveyed depth of 20 km in the depth domain post-domain conversion using an interval velocity data cube. A summary of the key acquisition parameters and aforementioned processing steps is provided in table 1.1. Figure 1.7 shows a random x-line,

inline and a depth slice at 14008 m of the processed 3D seismic dataset in the *True Vertical Depth* (TVD) domain for visualization purposes. For spatial context, the limits of the Sureste Basin offshore as well as of the AOI within block X are also shown on the figure.

Parameter	Value
Surveyed area	20800 km^2
Crossline (x-line) interval	25 m
Inline interval	25 m
Crossline (x-line) length	147625 m
Inline length	140900 m
Sample interval	4 ms
Recording time (TWT)	10 s
Seismic TVD (post domain conversion)	20000 m
Migration Algorithm	PreSDM RTM

Table 1.1: **Key acquisition parameters and migration algorithm for the offshore 3D PreSDM RTM dataset used for seismic interpretation.**
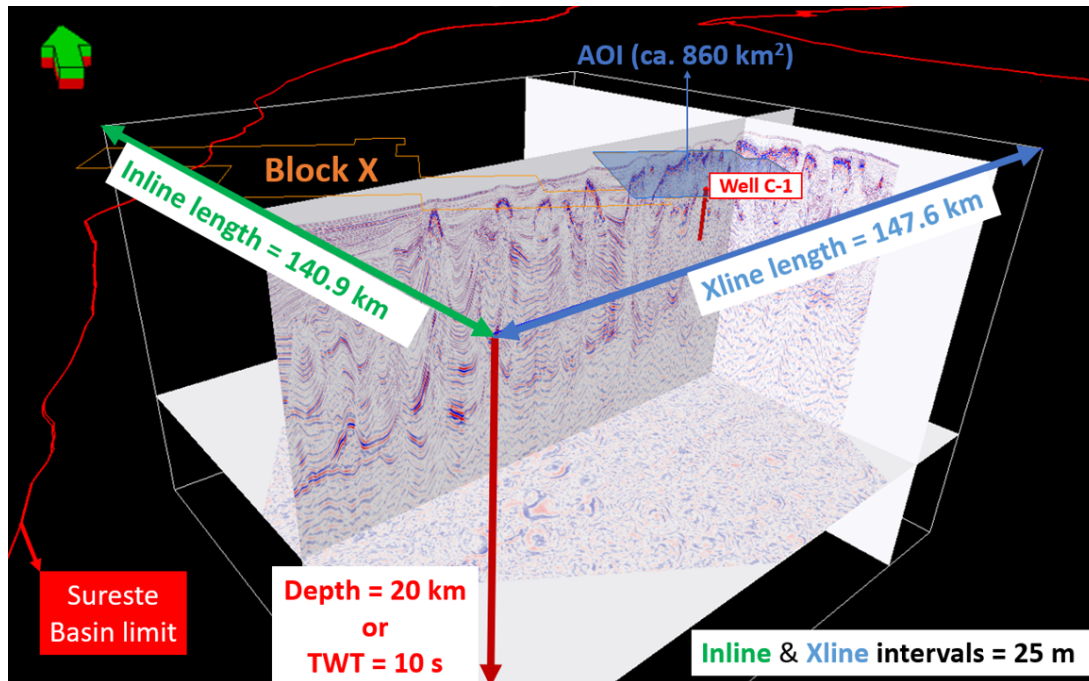
Figure 1.7: **The PreSDM RTM offshore 3D seismic dataset used for this study.**

1.2.2 Well Data Availability in AOI

Well data in the AOI was limited, with only one well (namely *C-1*) drilled towards the southwest in the AOI (see figures 1.2 and 1.7). This well had only been drilled to a *True Vertical Depth Sub-Sea* (TVDSS) of approximately 1787 m. Only formation temperature data obtained from *Horner*-corrected bottom-hole temperature data (Horner, 1951) from this well was available for this study; its usage as calibration data is discussed in detail in subsection 2.2.5.

1.2.3 Available Gridded Surfaces - Seismic Interpretation

From prior work in the region, regional interpretations using the 3D seismic dataset (subsection 1.2.1) for two horizons were available, which had been obtained using an autotracking algorithm in PaleoScan™. Interpretation via auto-tracking entails an automatic interpretation given initial seeding/interpretation points on horizons of interest (Chopra & Marfurt, 2014). The two horizons for which interpretations were available corresponded to the top horizons for

the T100 and T90 sequences. Autotracking was possible for these horizons due to their absolutely continuous nature, with minimal slope variations and no salt body protrusions (see figure 2.8). The initial interpretations that acted as seeding points for autotracking were facilitated by seismic-well ties in the region. The horizon interpretations were then converted to gridded surfaces in Petrel$^{©}$. Additionally, gridded surfaces for seismic interpretations conducted in Petrel$^{©}$ for the top of T50, J60 and J50 sequences were also available from prior work in the region. The surfaces representing the top of the Upper Miocene (T50) sequence and the Bajocian (Middle Jurassic) autochtonous salt sequence (J60) were initially interpreted discontinuously, with interpretation locally halted where protruding allochtonous salt bodies existed. The base of J60 surface was also interpreted discontinuously due to poor imaging quality hindering seismic horizon continuity. The interpretations were then gridded to generate surfaces, after which a *spline* interpolation algorithm was employed to fill gaps in the gridded surfaces in order to generate continuous surfaces. A similar procedure was adopted for interpretations conducted in this study, details for which can be found in section 2.1.5. The five gridded surfaces from seismic interpretation (clipped outside the AOI) can be visualized on figure 1.8.
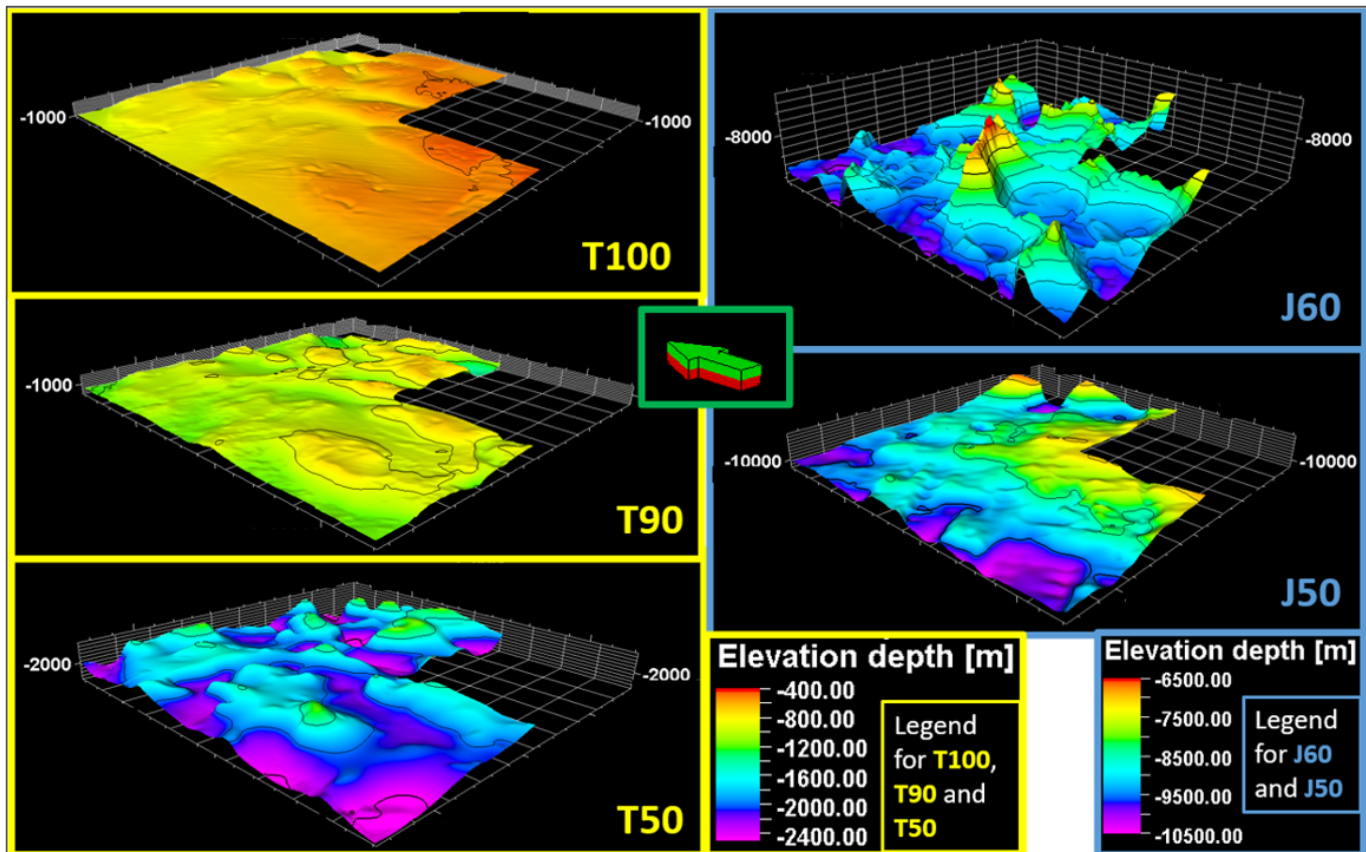
Figure 1.8: **5 available gridded surfaces for this study from prior seismic interpretation work.** The five gridded surfaces for the top horizons for the T100, T90, T50, J60 and J50 sequences are visualized in Petrel$^{©}$. All surfaces are shown with a vertical exaggeration of ×2, with depth contours representing depth increments of 500 m. See corresponding text for more details.

1.2.4   Available Gridded Surfaces - Gravity Data Inversion

From prior work in the region, gridded surfaces were also available in the study AOI for the crust-mantle (Moho) boundary and the base of the upper crust (top of lower crust). These surfaces were obtained from gravity data using an inverse modelling scheme in the software GM-SYS 3D$^{©}$. As a part of the results, a surface for the top of J50 (base of J60) was also available from the modelling results as an alternative to the available surface from seismic interpretation.

While the specific details regarding the gravity data modelling scheme cannot be revealed due to confidentiality requirements, a general and brief overview of the scheme is provided for interested readers. Firstly, an initial geological model was set up to introduce *a priori* constraints. This geological model utilized bathymetric data, the top of the autochtonous salt surface, and initial allochtonous salt canopy/diapir delineation surfaces in the region, obtained from

seismic interpretations on the dataset presented in subsection 1.2.1. In addition, the interval velocity data cube (used for the seismic dataset domain conversion), published data for regional depth-density relationships for all lithologies of interest (Gardner et al., 1974; Jackson & Talbot, 1986), and estimates of the Moho and top upper crust surfaces for the study region from prior company studies (confidential) were also used for the initial geological model construction. Moreover, measured free-air gravity anomaly data was available for the region. The modelling scheme calculated the free-air gravity anomaly responses from the initially set up geological model, and then compared the *calculated* anomalies with the *measured* anomalies. The misfit between the calculated and measured gravity anomalies was minimized by adjustment of the the (initial) geological model. The resulting Moho and base of upper crust surfaces from the final geological model are shown in figure 1.9.
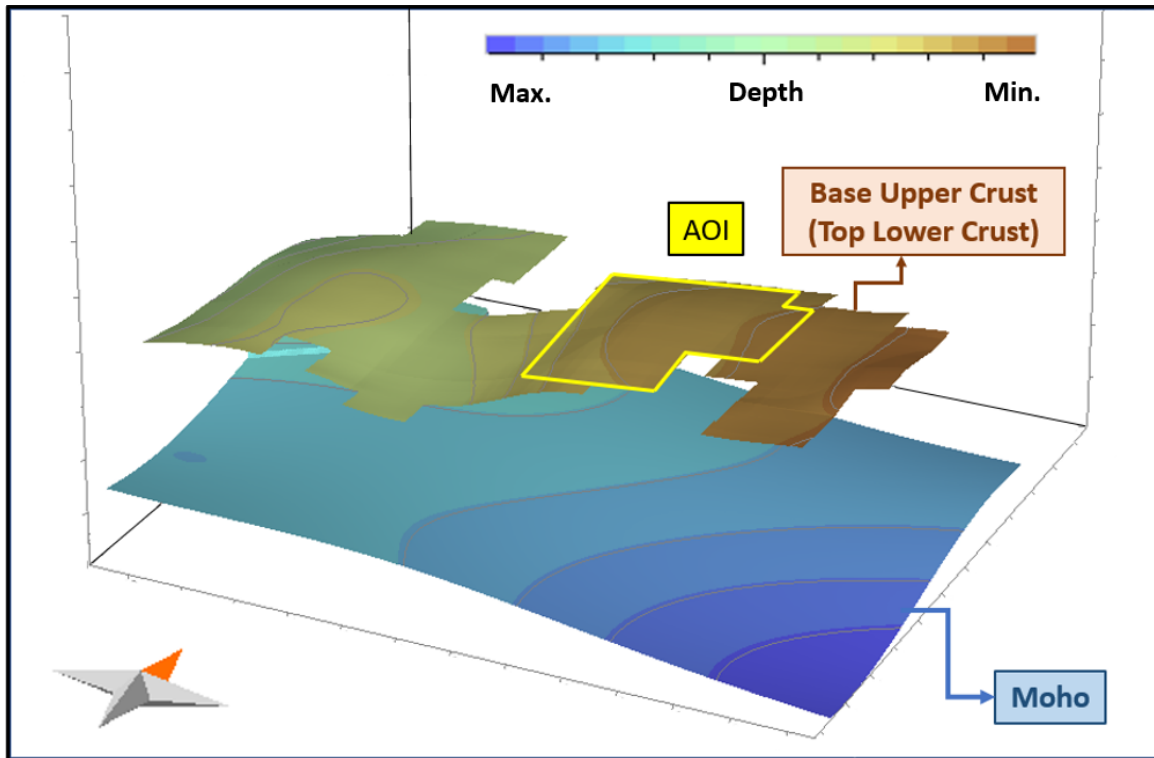
Figure 1.9: **The surfaces for the base of the upper crust (top of lower crust) and Moho from gravity data inversion results.** The surfaces shown have a vertical exaggeration of ×2. The surface for the base of the J60 autochtonous salt sequence from the gravity data inversion results is not shown to aid enable proper visualization of the other two surfaces; this surface is implicitly shown in figures 2.9 and 2.15.
Note: The depth values for the surfaces have been hidden due to confidentiality requirements of Wintershall Dea GmbH and partners.

1.3   Study Objectives and Structure

The overarching aim of this study was to acquire initial estimates of the Tithonian (J100) source rock maturity in terms of the maturity parameters *Vitrinite Reflectance* (%R_0) and Transformation Ratio (TR) (see Preface I). Specifically, the main objectives of this study were as follows:

- Acquire initial estimates of the source rock maturity through time and in the present-day at the C-1 well location.

- Acquire initial estimates of the source rock maturity through time and in the present-day across the wider AOI.

- Place constraints on the possibility of oil and/or gas accumulations in the vicinity of the C-1 well location based on the maturation timing of the J100 source rock at the location in relation to the timing of other petroleum system elements and processes.

To this end, a thermal modelling workflow was undertaken, based on which seismic interpretation was conducted as a first step. The interpreted surfaces from this step, in conjunction with the available gridded surfaces (see subsection

1.2), were utilized as the structural input for the thermal model. The thermal model was then set up, which involved assignment of layer properties and model paleo-geometry, as well as the assignment of the (thermal) boundary conditions. To determine the lower (thermal) boundary condition, namely the *basal heat flow*, a crustal modelling scheme was used to place geologically reasonable constraints on the values assigned to the boundary condition parameter. Once the model setup and boundary condition assignment was complete, the model was simulated to yield the maturity values of interest at time steps of interest through the source rock's depositional history.

A *one-at-a-time* (OAT) sensitivity analysis (e.g. see Wainwright et al. (2014)) approach was also undertaken to assess the variability in output maturity values by varying individual input parameter values in isolation. This was done to identify which of these key parameters yielded the greatest variability in the simulated source rock maturity values. The resulting ranges in source rock maturities from the sensitivity analyses were assumed to serve as reasonable *initial estimates* to enable further petroleum system elements and processes timing analysis (see text above regarding study objectives).

Figure 1.10 schematically describes the thermal modelling workflow for this study. Details regarding each step of this workflow are the focus of chapter 2.
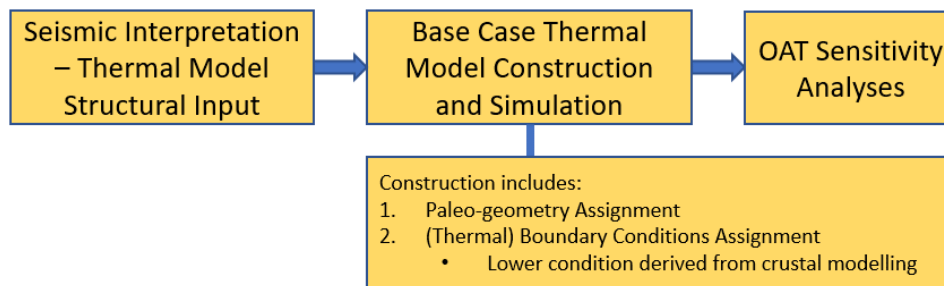

Figure 1.10: **General overview of the workflow for the thermal modelling scheme for this study.**

Chapter 2

Methods

The aim of this chapter is to provide a detailed description of the workflow followed for a thermal modelling scheme to determine source rock maturity estimates of the Tithonian source rock (Edzna Formation) in the AOI. Section 2.1 details the steps taken involving seismic interpretation to derive a structural input for the thermal model. Section 2.2 provides information regarding the base case thermal model construction, the key modelling parameters, assignment of the upper (thermal) boundary condition and paleo-geometry parameter values, and a crustal model developed to determine the lower (thermal) boundary condition values for the thermal model. Lastly, *one-at-a-time* (OAT) sensitivity analyses performed to assess the sensitivity of the thermal maturities of the source rock on various key parameters of interest are described in section 2.3.

2.1 Seismic Interpretation - Structural Input for Thermal Model

To construct the thermal model for this study, structural information of the subsurface in the AOI was necessary as the core input. This information was extracted from the 3D seismic dataset available in the region (see subsection 1.2.1) through seismic horizon interpretation. The aim was to interpret all horizons - following the tectono-stratigraphic sequences identified proposed in subsection 1.1.3 - for which there were no surfaces available from prior work (see subsections 1.2.3 and 1.2.4). The following subsections describe in detail the seismic interpretation process for this study. The interpretations and other associated steps were done using Petrel$^{©}$ (Version 2018.2). It is critical to note that from hereon, the top horizons for their respective tectono-stratigraphic sequences will be referred to following the nomenclature for the sequences themselves for simplicity purposes. For example, the label T100 will be used to refer to the top horizon of the T100 sequence.

2.1.1 Interpretation Workflow

The C-1 well being the only well drilled in the AOI did not penetrate the shallowest horizon that needed to be interpreted given the availability of the interpreted surfaces for the shallow T100, T90 and T50 horizons. Thus, the lack of well control led to a lack of seismic-well ties for the horizon interpretations for this study. To compensate, using the tectonic and stratigraphic contextual framework available for the sedimentary fill (see section 1.1), structural and stratigraphic constraints were introduced for interpretation through an analysis of the subsurface information available in the seismic dataset. A generalized workflow for the seismic interpretation process can be seen schematically represented in figure 2.1.
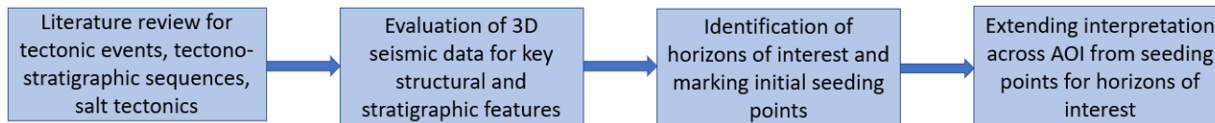
Figure 2.1: **Seismic interpretation workflow adopted for this study.**

2.1.2 Structural and Stratigraphic Evaluation

To facilitate interpretation, the 3D seismic dataset in the depth domain was evaluated within the AOI. As a first step, key structural features were identified to provide a structural framework within which the individual horizons could be later mapped. The first such feature extensively observed in the AOI were reverse/thrust faults, examples of which are

shown in figure 2.2. The faults were interpreted loosely with the sole aim of understanding the structural setting, and were not interpreted for later integration within the thermal model as key structural elements (see subsection 2.2.2). The justification for this simplification is provided in subsection 2.1.6.

On figure 2.2, floating blocks are also shown that are related to extensive thrust faulting due to the Chiapaneco Middle Miocene compressional event. Such floating blocks were identified in the east-northeast of the AOI. In addition, numerous allochtonous salt bodies were also identified within the AOI, with some salt bodies even indicating upwards density-contrast driven migration in the present-day, causing doming of the seabed T100 horizon (see figure 2.2). Other structural features such as salt-related turtle structures (leading to doming of the sequences overlying the autochtonous salt), fault-propagation folds (figure 2.3) etc. were also observed in the AOI.
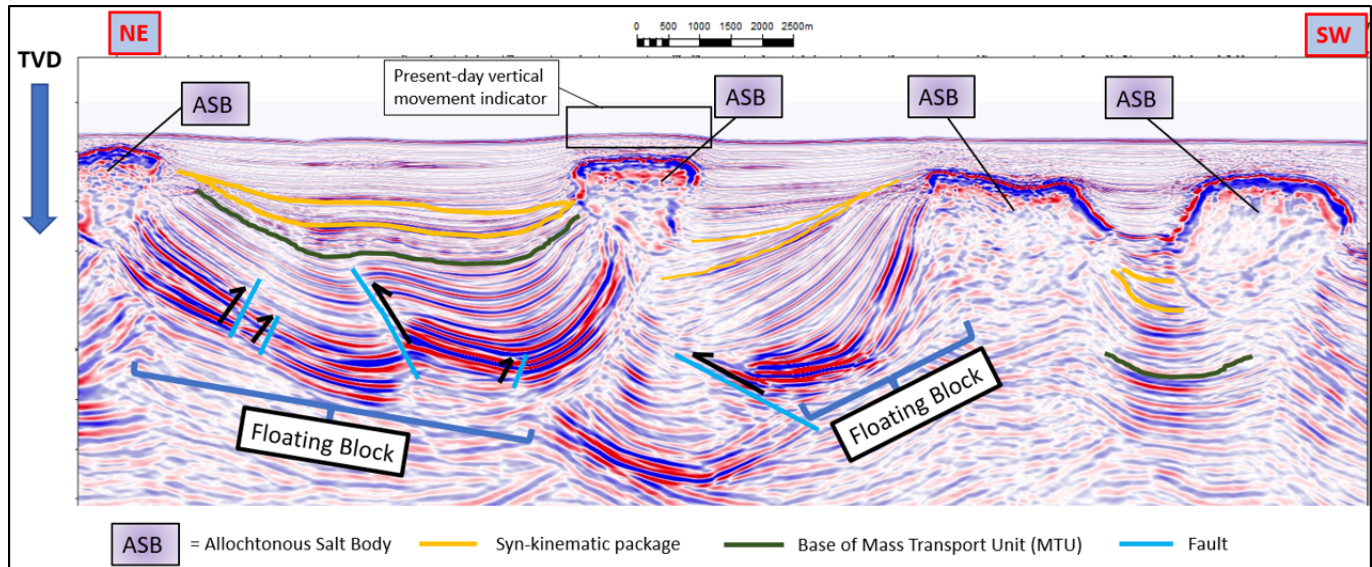
Figure 2.2: **Evaluation of structural and stratigraphic features to facilitate later horizon interpretation**. Note: The true vertical depth (TVD) values as well as the location of the cross-section in the AOI have been hidden due to confidentiality requirements of Wintershall Dea GmbH.

Having identified key structural features to understand their effect on the spatial evolution of the depositional sequences across the AOI, key stratigraphic markers were focused on to further constrain interpretations of the horizons of interest. Firstly, the most easily detectable syn-kinematic depositional unit was identified, known to be the Middle Miocene T55 sequence associated with the Chiapaneco compressional event. This syn-kinematic package has been indicated in figures 2.2 and 2.3. This unit emerged quite visibly as the "bridging" unit between the underlying extensively structurally altered sedimentary sequences and the overlying, more structurally uniform and passive sedimentary sequences.

Next, chaotic and severely discontinuous reflectors in the seismic dataset, in particular in the north-northeast segment of the AOI, were identified as *Mass Transport Units* (MTUs) related to turbiditic channels and fan lobes characteristic of the Lower Miocene (see subsection 1.1.3). Examples of these MTUs are shown in figures 2.2 and 2.3. Moreover, clear thickness variations across a deposited sequence indicating structural alteration in the form of tilting/folding during deposition were observed at greater depths relative to the MTUs across the AOI. This sequence was understood to have been deposited during the Laramide-related compressional event (see figure 2.4).

2.1.3   Horizon Identification and Interpretation

Having established a structural and stratigraphic framework, key horizons of interest were identified on the seismic dataset. According to Sanford et al. (2016), the K100 horizon is observable clearly in seismic and well data covering offshore Sureste Basin as a high amplitude/bright peak reflector across the entire GOM due to its stark impedance contrast compared to its overlying sequence. This is owing to the sequence's predominantly carbonaceous lithology. According to Shann et al. (2020), the T20 horizon is distinguishable in offshore 3D seismic data as a strong, continuous blanket reflector over the underlying Cretaceous sequences, which associated with the marine flooding-related regional shale. Both the K100 and T20 were identifiable in the AOI following the described characteristics. The T30 was identified as the top horizon for deposited sequences with varying thicknesses related to the Laramide-related compression, following the T30 sequence descriptions from Comisión Nacional de Hidrocarburos (2019). This horizon could also be marked as a blanketing, relatively flat horizon overlying thrusted packages in multiple parts of the AOI, also associated
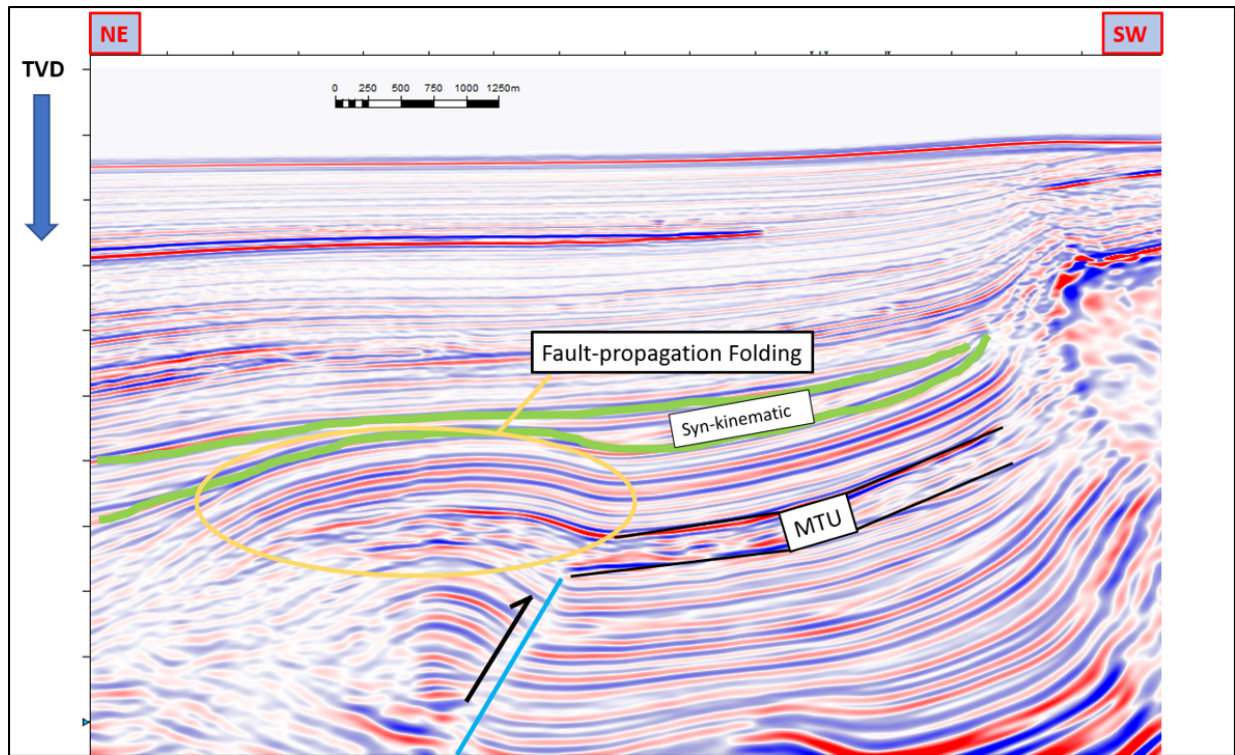
Figure 2.3: **Key structural and stratigraphic features identified on the 3D seismic data in the AOI**.
Note: The true vertical depth (TVD) values as well as the location of the cross-section in the AOI have been hidden due to confidentiality requirements of Wintershall Dea GmbH.

with the aforementioned compression. In conjunction to these stratigraphic and structural markers, the identification of the T30 horizon was also facilitated by relatively strong (peak) amplitudes, owing to notable carbonaceous content in the sequence (see subsection 1.1.3). The base of the Lower Miocene T52 sequence, marking the top T40 horizon, was identified at the base of the MTUs in the AOI following the description from Shann et al. (2020) (see section 1.1.3). The T52 horizon was easily identified as the base of the syn-kinematic packages observed widely in the AOI (figures 2.2 and 2.3), whereas the T55 horizon was marked as the top of this syn-kinematic sequence above which no considerable thickness variations existed.

All six horizons can be seen interpreted in the depth domain over a random composite line connecting various *mini-basins* in the AOI in figure 2.5. The term mini-basin from hereon refers to the regions in the AOI separated by allochtonous salt bodies. It is important to note that in the absence of seismic-well ties - a key step that provides information regarding the correspondence of a horizon with a peak, trough, z-crossing (peak to trough) or s-crossing (trough to peak) on the seismic data - all horizons were interpreted as peaks. While interpretations for the K100 and T30 as peak horizons are geophysically justifiable due to expected positive acoustic impedance contrasts with their overlying sequences, such assumptions for other horizons need not necessarily hold true.

Using the horizon interpretations from the random composite line as initial seeding points, interpretations were extended for each of the horizons across the AOI on the x-lines and inlines. For interpretations for each horizon in each mini-basin, separate horizon files were used to account for vertical stacking (see figure 2.5) observed extensively across the AOI. This was done since interpretations within a single horizon file do not allow multiple depth values ascribed at a single lateral (x,y) location. Interpretations were conducted on every 16th x-line and inlines (down to every 4th x-line and inline in structurally complex areas) for all interpreted horizons except the K100; the K100 was interpreted on every 4th inline and x-line across the AOI.

2.1.4   Interpretation Results

Once completed, the interpretations stored in all horizon files were gridded to ensure that an interpretation point existed on every x-line and inline over the interpreted region. As a result, continuous *surfaces* were generated. This step was necessary since only continuous surfaces could be used as inputs for the thermal model constructed. The gridding process in Petrel[©] is facilitated by an autotracking algorithm that follows the phase of the waveform picked for the interpretation - peaks for all interpretations in this case - till the next interpretation point is reached on the
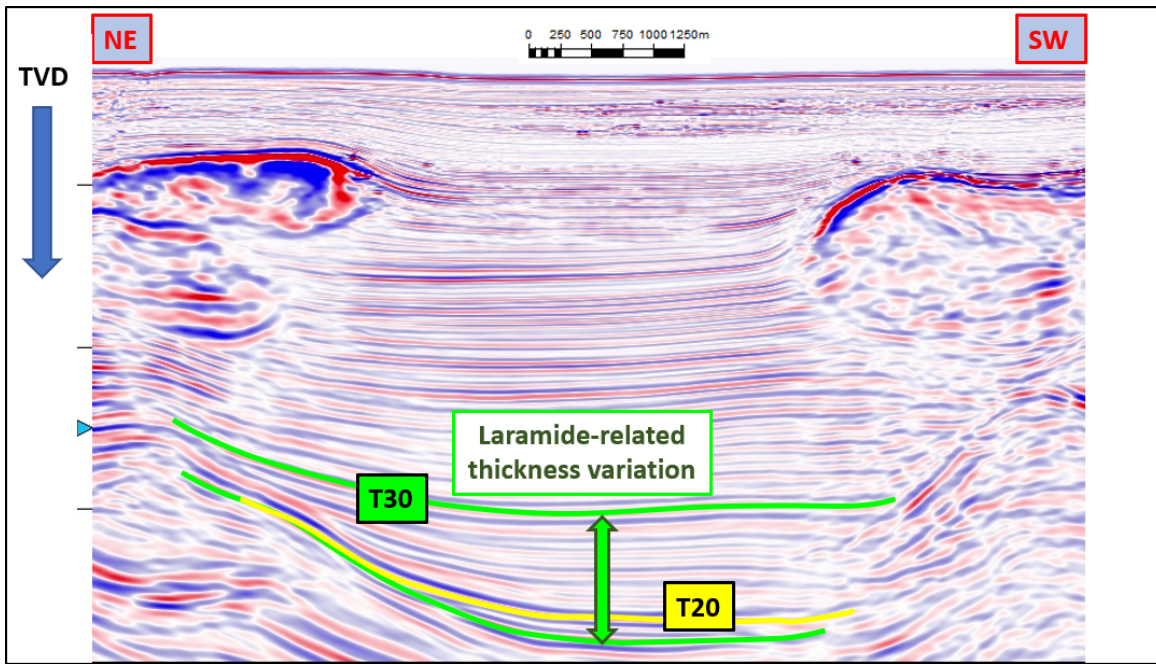
Figure 2.4: **Clearly observable thickness variations in the deposited sequence coinciding with the Laramide orogeny.**
Note: The true vertical depth (TVD) values as well as the location of the cross-section in the AOI have been hidden due to confidentiality requirements of Wintershall Dea GmbH.
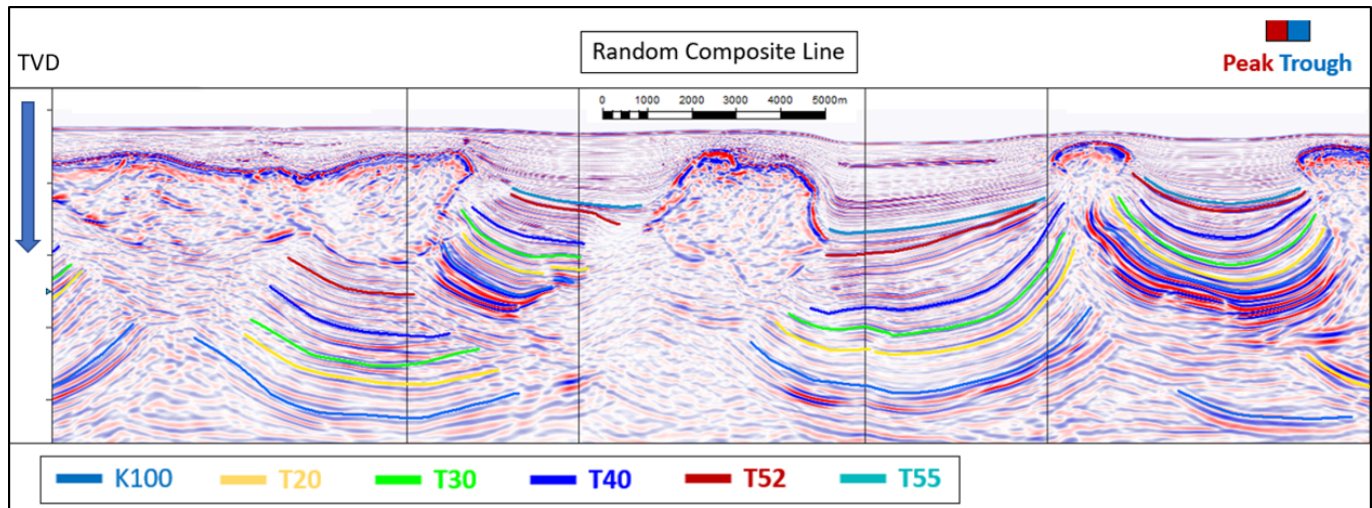
Figure 2.5: **K100, T20, T30, T40, T52, and T55 horizons identified and interpreted on a random composite line connecting various mini-basins in the AOI.** On the seismic, the peaks and troughs of the seismic waveforms are indicated by the colors red and blue, respectively. No faults have been shown interpreted since they were marked only to understand the structural framework.
Note: The true vertical depth (TVD) values as well as the location of the cross-section in the AOI have been hidden due to confidentiality requirements of Wintershall Dea GmbH.

dataset. In areas where the interpretation shows discontinuities or "jumps", a *spline* interpolation algorithm is utilized to ensure that the trend of the gridded surface is maintained. The extent of the tracking is limited by boundary polygons, which were drafted along the edges for each mini-basin-separated interpretation to ensure that the gridding process was constrained within the manually interpreted regions. The grid cell size for all surfaces generated theas determined by the inline and x-line interval i.e. the cell size was $25\,\mathrm{m} \times 25\,\mathrm{m} \times 25\,\mathrm{m}$ in 3D. For all horizons of interest, numerous surfaces were generated for the mini-basin-separated interpretations, and these are shown in figure 2.6. It is useful to note that the regions where no surfaces exist on the figure are predominantly due to the protruding

allochtonous salt, a feature that became increasingly prominent in shallower horizons and hence led to increasingly sparse interpretations. Reasons for why the allochtonous salt bodies were not interpreted during the interpretation process are discussed in subsection 2.1.6.

It is critical to note that surfaces for the J80, J90, J100, K50 and K80 horizons were not interpretable on the available seismic dataset based purely on structural and stratigraphic constraints. These surfaces needed to be accounted for as pseudo-surfaces in the thermal model; this will be discussed later in section 2.2.2.

2.1.5   Data Preparation for Thermal Model

Merged Surfaces   The numerous individual surfaces for each horizon needed to be merged into single surfaces representing each horizon for the thermal model; this was done as a part of the process to generate continuous (gap-free) surfaces for each horizon for the thermal model. This led to a simplification of the horizon geometries in localized regions towards northeast of the AOI where vertical stacking of the horizons was observed (i.e. multiple depths at a single x,y location), since a single gridded surface only allowed for single depth values at each lateral location. In such vertically stacked regions, deeper interpretations for the K100 were preferentially retained in the merged output surfaces while shallower interpretations were preferentially retained for the stacked horizons (T20 to T52). For the K100 horizon, the deeper lying interpretations were used since these interpretations were to be used to generate the J100 surfaces (see subsection 2.2.2), and it was decided that the source rock maturities at the deeper depth ranges were of more interest. As for the other overlying horizons (T20 to T52), the shallower lying interpretations of the vertical stack were used since structural and stratigraphic markers to enable interpretations were much clearer at shallower depths and hence the shallower interpretations were more reliable. Owing to these simplifications, a much thicker T20 layer package was observed in these localized areas in the northeast of the AOI (see figure 2.7). The impact of such a simplification on the study results is discussed in 4.2.1.
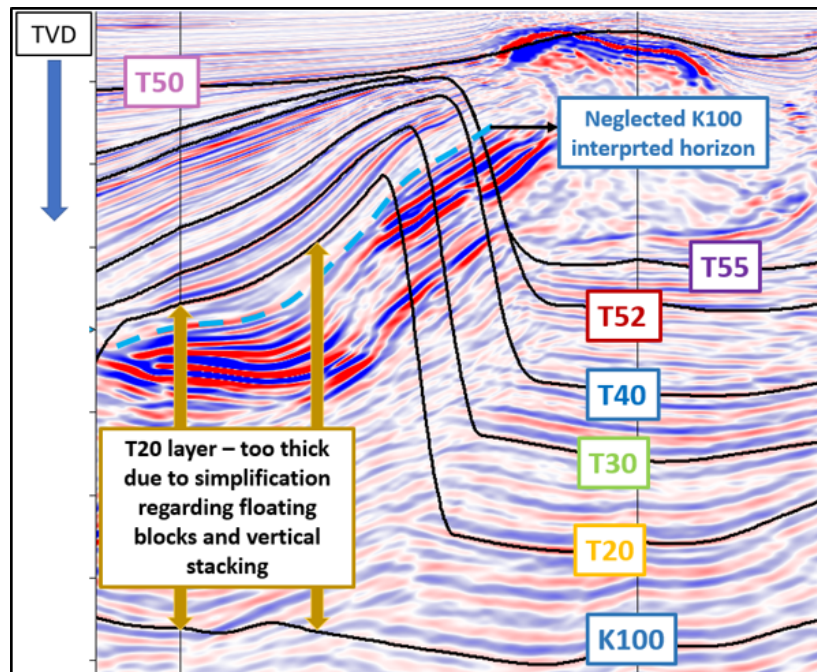
Figure 2.7: **Simplified merged surfaces due to neglection of vertical stacking leading to locally very thick T20 layer.** See corresponding text for more details.
Note: The true vertical depth (TVD) values as well as the location of the cross-section in the AOI have been hidden due to confidentiality requirements of Wintershall Dea GmbH.

Interpolation Algorithms and Manual Intersection Treatment   To fill the gaps in merged horizons where allochtonous salt bodies disabled continuous interpretation, a *spline* interpolation algorithm was implemented that utilizes low-degree polynomials to connect manual interpretation points. An example of such an interpolation is shown in region A of figure 2.8.

Since the trends of the interpretations guided the interpolation, intersections of surfaces in interpolated regions were observed that led to deeper surfaces (representing a geologically older horizon) cutting "through" shallower surfaces (representing geologically younger horizons). This created geologically erroneous scenarios, which would prevent model
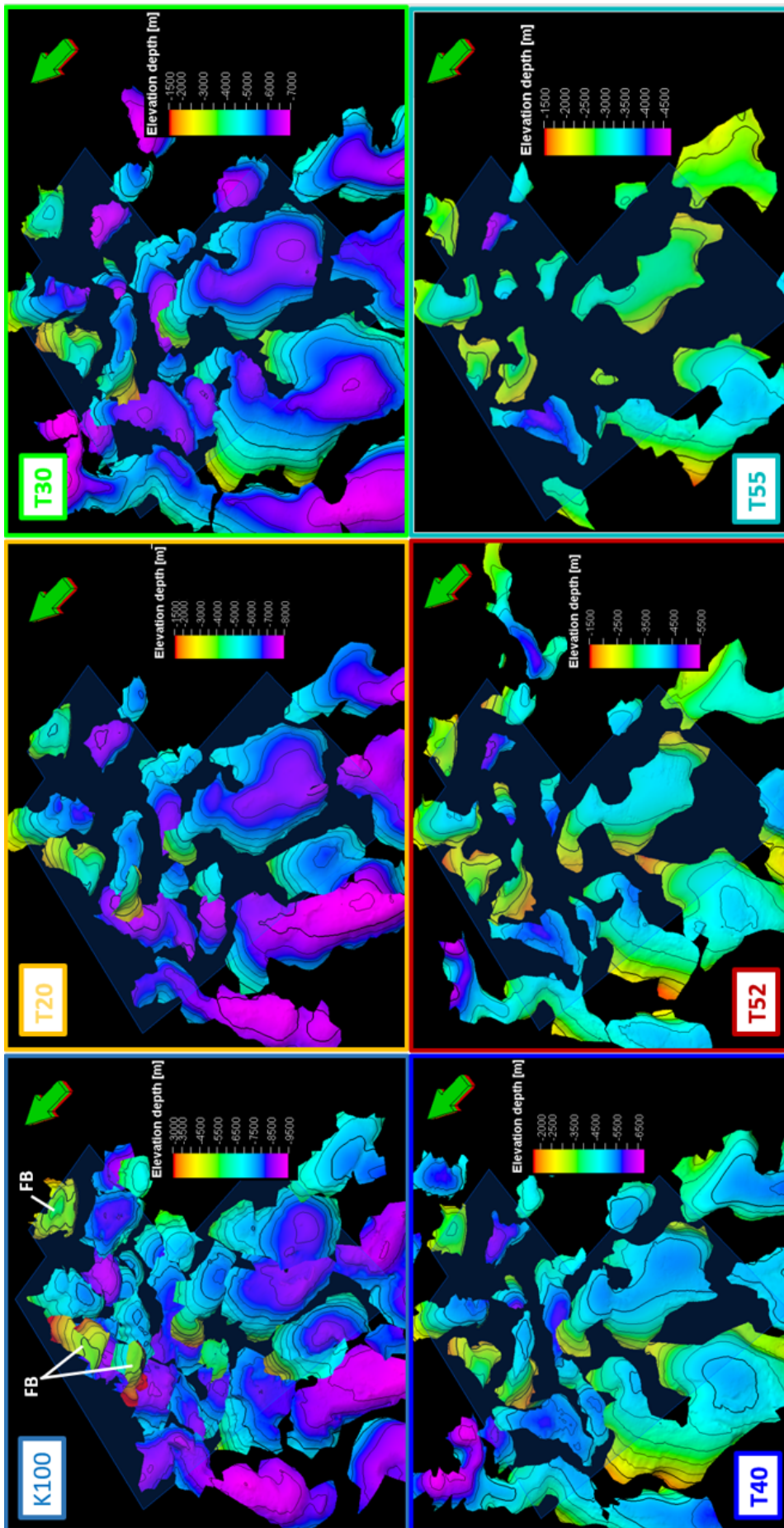
Figure 2.6: **Gridded surfaces for individual mini-basin-separated interpretations for the K100, T20, T30, T40, T52 and T55 horizons.** Increasingly sparse interpretations for shallower horizons were a result of protruding allochtonous salt bodies. The depth contours on the surfaces represent depth increments of 500 m.

Note: **FB** = Mini-basin surfaces associated with floating blocks.

simulation. As a countermeasure, such intersections were treated in Petrel[©] such that shallower surfaces, where they cut deeper than the underlying surfaces, were guided to follow the trend of the underlying surface; a 5 m vertical separation was introduced between the surfaces. As opposed to the deeper horizons being guided to follow the shallower surface trends, the aforementioned treatment approach was preferred because it supports a more geologically realistic scenario i.e. the depositional geometry of a sequence is dictated by the geometry of its underlying sequence. It is critical to note that such treatment was only necessary in interpolated regions.
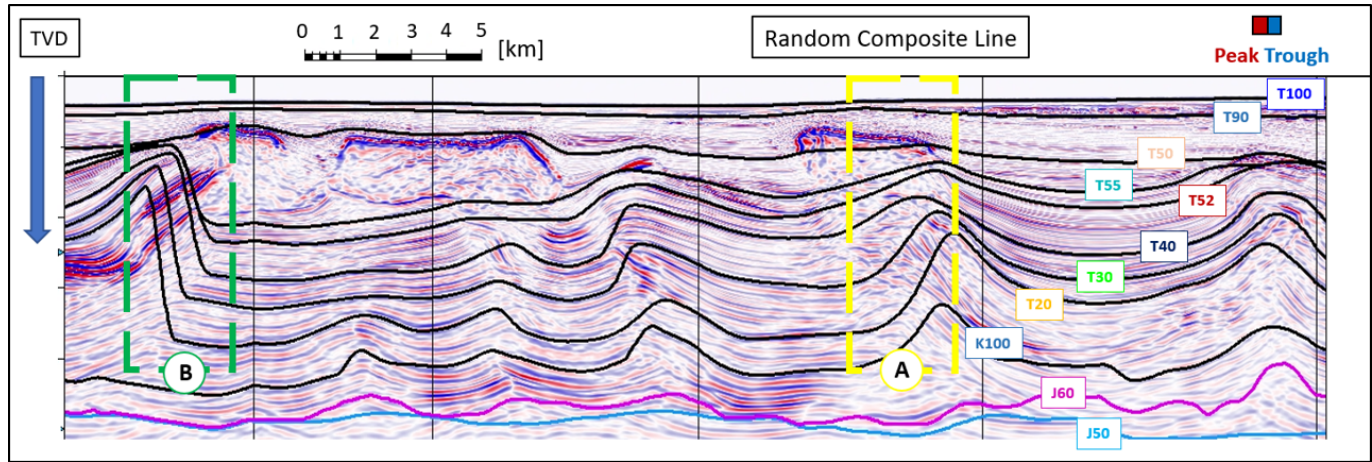
Figure 2.8: **A random composite line in the AOI showing all interpreted and priorly available surfaces post-treatment.** Region A (outlined in yellow) shows an example of the spline interpolation algorithm implemented. Region B (outlined in green) shows the effect mini-basin-separated surface merging; the deeper lying surfaces for all horizons were preferentially retained at the expense of the extensions of the shallower surfaces. Region B also highlights the effect of the smoothing filter that dampens of the slopes of otherwise near-vertical surfaces.
Note: The true vertical depth (TVD) values as well as the location of the cross-section in the AOI have been hidden due to confidentiality requirements of Wintershall Dea GmbH.

Surface Smoothing Grid nodes for the merged and interpolated surfaces in Petrel[©] were separated by 25 m. In PetroMod[©] (see section 2.2), while retaining the same grid node separation for modelling is possible, the input model is often re-gridded (sampled) during simulation where the grid cell size is limited to a minimum of 100 m for computational efficiency. This prompted the use of a smoothing filter for the surfaces. This was so because in areas where a shallower mini-basin-separated surface overlapped with a deeper surface and the two were merged, a very steep bridging surface that linked the two surfaces was generated. Such steep bridging surfaces had lateral displacements of 25 m, limited by the grid cell size in Petrel[©]. In a standard sampled grid in PetroMod[©], such a steep surface would be read as a vertical surface owing to grid size limitations, thereby introducing the need for computationally-intensive finer grid sampling. To circumvent this, a smoothing filter with an influence radius of 75 m was applied to all surfaces. Such a filter calculated an average (depth) value for each cell based on the surface depth values in three adjoining cells (3×25 m) in all orientations. As desired, such smoothing resulted in negligible geometrical alteration in all surfaces in regions that were gently dipping, while near-vertical regions were smoothed sufficiently to prevent gridding errors in PetroMod[©]. The result of such smoothing is shown in region B of figure 2.8.
The post-treatment final surfaces used as the structural input for the thermal model are shown in figure 2.9.

2.1.6 Key Assumptions - Seismic Interpretation

Neglection of Faults and Thrusted Packages (Vertical Stacking) As described in section 1.3, the aim of the thermal model was strictly to constrain thermal maturities of the J100 sequence, and not to evaluate petrophysical processes such as hydrocarbon migration, which would indeed be largely impacted by the presence of (open/non-sealed) faults. For a thermal maturity model, faults only play a role in the burial history of the sediments. While an accurate reconstruction of the burial history of deposited formations is critical for more accurate estimations of thermal maturities, this would require well-founded information regarding the extent and timing of all faults mapped. Extracting such information from the available seismic data was difficult for a number of reasons:

1. Limited vertical resolution (up to 250 m) was noticeable in the depth ranges within which major fault activity was visible in the seismic. This inhibited accurate fault extent estimation into different sedimentary packages, which can provide information regarding fault activation timing.
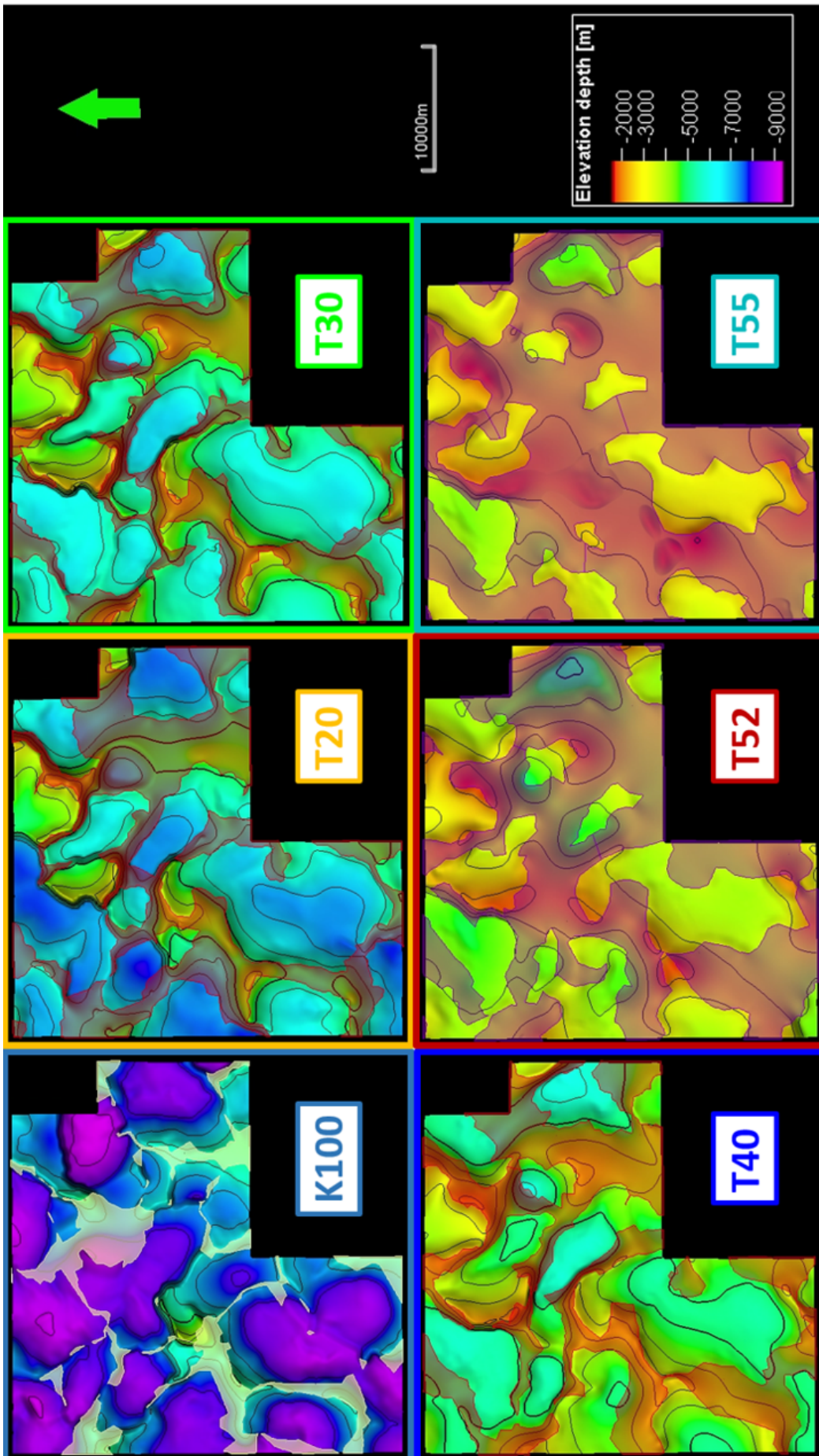
Figure 2.9: **The post-treatment surfaces used as the structural input for the thermal model (clipped outside the AOI).** These six surfaces were used in conjunction with the five available surfaces described in section 1.2. The regions highlighted using maroon polygon fill (yellow fill for K100) depict the interpolated regions.

2. A number of compressional events impacted the structural settings of the basin fill, and this could entail an activation and later re-activation of faults, a consideration that would require detailed analyses of thickness variations in the sedimentary sequences deposited syn-faulting in the vicinity of faults of interest. Again, vertical resolution limits inhibited such an evaluation.

Moreover, the faults identified within the sedimentary fill were reverse/thrust faults associated with compressional tectonics. Normal faulting associated with rifting led to the formation of syn-rift grabens in the crustal basement, propagating upwards even into the J50 sequence deposited syn-rift (Shann et al., 2020), but these could not be resolved below the autochtonous salt J50 sequence in the seismic data. Reverse/thrust faults lead to vertical stacking of horizons, as is visible on figure 2.2. Incorporating reverse/thrust faults into the modelling scheme would imply the need to consider a multi-z model, as opposed to a standard model that does not allow for the existence of a single horizon at multiple depth locations at a specified lateral location. Multi-z models require detailed information from palinspatic structural restoration studies that clearly provide information regarding geomechanical process e.g. fault extent and timing, sediment (de-)compaction etc. Due to a lack of such data, a standard model was focused on that could not account for such reverse/thrust faulting by definition.

Allochtonous Salt Neglection   The integration of allochtonous salt bodies in a thermal model would firstly require well-founded delineation of the allochtonous salt bodies, in particular to determine whether they were diapirs (attached to autochtonous sequence) or canopies (detached to autochtonous sequence). Though the sub-salt imaging quality achieved with WAZ seismic survey designs is known to be better compared to a Narrow-Azimuth (NAZ) designs, clear delineation for all salt bodies was still not possible. Secondly, detailed analyses of salt movement and spatial distribution through time with the aid of palinspatic structural restoration studies would be needed. Such analyses would also need to account for the geomechanical impacts of such movement on surrounding depositional sequences in terms of uplift and tilting, decompaction etc. This data was unavailable for this study and therefore prompted simplifying assumptions. A discussion on the impact of salt neglection on the study results can be found in 4.2.2.

Horizon Extent Estimation   Determining the extent of horizons in salt-flank and sub-salt regions was also related to difficulties with salt body delineations. This was in most cases related to the difficulty in distinguishing between the "tail end" of the allochtonous salt and the horizon of interest, thereby introducing uncertainties (in some cases, in the order of 500 m) with regards to how shallow the horizon truly existed (see figure 2.10). As a rule of thumb, it was assumed that the horizon of interest was geologically absent in sub-salt and salt-flank regions where the seismic signal became noticeably discontinuous, and this usually occurred as the horizon dipping angles exceeded $\approx 60°$. Beyond such dipping angles, the horizons were not interpreted.
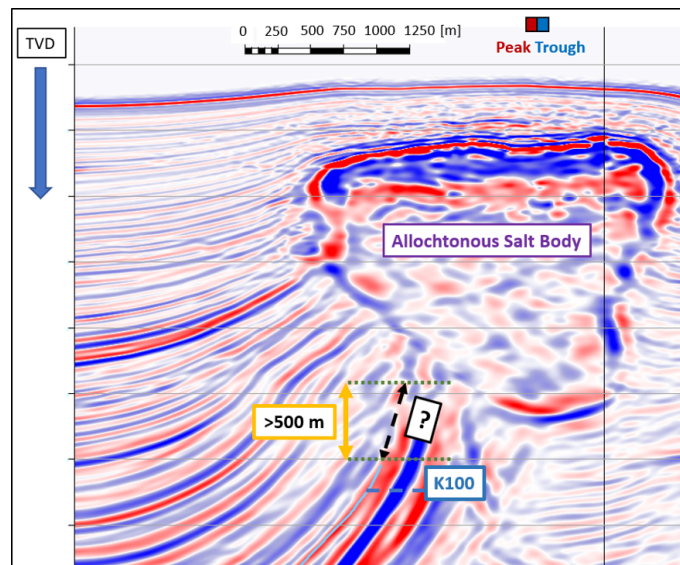
Figure 2.10: **Difficulty in estimating how shallow horizons of interest extend in salt-flank or sub-salt regions.** Horizon interpretations were stopped in such regions where the signal became noticeably discontinuous, usually at steep dipping angles exceeding $\approx 60°$. See corresponding text for more details.
Note: The true vertical depth (TVD) values as well as the location of the cross-section in the AOI have been hidden due to confidentiality requirements of Wintershall Dea GmbH.

2.2   Thermal Modelling

With the continuous gridded surfaces available from the interpretation work described in section 2.1 as well as from prior work done in the region (section 1.2), the thermal modelling process was initiated, which is the focus of this section.

2.2.1   Modelling Workflow

The modelling process can be divided into four principle steps, namely model construction (input), paleo-geometry and boundary conditions assignment, model simulation, and model results evaluation. The model construction step involves setting up the model such that the structural input (limited to horizon surfaces for this study) is utilized to generate multiple subsurface layers; these layers can then be ascribed various properties to digitally represent the subsurface in the AOI. The boundary conditions assignment step involves specifying the basal heat flow (lower boundary condition) and sediment-water interface temperature (upper boundary condition) trends to define the thermal conditions for the model through time. Similarly, the paleo-geometry assignment step involves setting up a paleo-water depth trend, a parameter that directly impacts the SWIT and the burial history of the deposited sedimentary sequences. The model simulation step allows users to define the outputs of interest, as well as to undertake any specific assumptions. Finally, the results evaluation step involves assessment of the output parameters of interest in terms of their reasonability; this is usually tested via comparison of simulated results with available well data (known as calibration data) in the AOI. Typically, the modelling process is iterative i.e. the model input parameters as well as the boundary conditions and paleo-geometry assigned need to be updated/calibrated in order to attain better agreement/fit of the output parameter values with the available calibration data. A schematic representation of the workflow followed for the modelling scheme for this study can be seen in figure 2.11. All associated steps with this modelling workflow were conducted in PetroMod$^©$ (Version 2019.1), a basin and petroleum systems modelling software developed by Schlumberger$^©$.
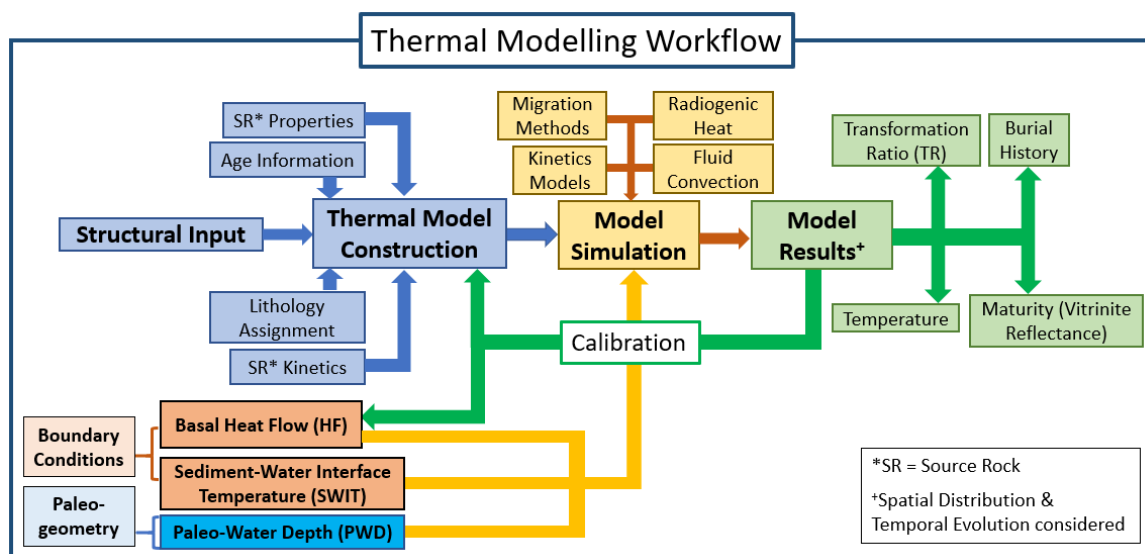
Figure 2.11: **A schematic representation of the general workflow for the thermal modelling process for this study.**

2.2.2   Model Construction - Base Case

All sub-steps associated with model construction described in this subsection were conducted in the PetroBuilder 3D$^©$ interface of PetroMod$^©$, unless explicitly stated otherwise.

Pseudo-Surface Generation   Based on the 11 total horizon surfaces, a preliminary model structure could be set up. In addition, five pseudo-surfaces for the J80, J90, J100 (top of Tithonian source rock sequence), K50, and K80 horizons needed to be generated in the absence of seismic interpretations for these surfaces.
The J100 surface, marking the base of the Cretaceous depositional package (K50, K80 and K100 sequences), was generated by manually shifting the K100 surface 500 m deeper. This implied that the entire Cretaceous package had a constant true vertical thickness (TVT) of 500 m across the AOI. However, the true stratigraphic thickness (TST) -

calculated normally to the dipping angle of the layer - was smaller than 500 m in all regions where the layer was not perfectly horizontal; smallest TST values would therefore be observed at the steepest dipping angles e.g. in salt-flank regions.

The generation of the J100 surface as such was based on literature suggestions. Grajales-Nishimura et al. (2003) provided a generalized stratigraphic column from the Campeche slope where the supergiant Cantarell field is located; an average depth of 500 m was denoted for the Cretaceous package. This value was corroborated by the interpreted 2D regional seismic sections in the Campeche shelfal and slope regions presented by Snyder & Ysaccis (2018), where the Cretaceous package could be seen varying in thicknesses from approximately 200 m to 700 m. Similar values could also be estimated from seismic sections presented by Comisión Nacional de Hidrocarburos (2019) from the Central Saline Basin (sub-basin within the Sureste Basin), which is located slightly to the north of the AOI. Lastly, Arzate et al. (2009) also suggested that the Cretaceous package thicknesses in the Campeche Bay Area vary from 100 m in shallower settings to 600 m in deeper water settings. Davison et al. (2021) pointed out that the Sureste Basin remained relatively starved of clastic sediment input during the Cretaceous, with approximately only 1 - 3 km of carbonate sediment deposited in the deep-water GOM during the time (Snedden & Galloway, 2019). This suggestion aligns with Cretaceous package thicknesses in the order of 500 m in the Campeche slope regions.

The assumption of constant TVT for the Cretaceous package undertaken for the model can be understood as reasonable, since the entire Mesozoic package in the offshore 3D seismic dataset in the AOI shows minimal thickness variations owing to the fact that any compressional events leading to the presence of syn-depositional packages did not occur during the Cretaceous period. The thickness variations visible in the seismic sections from literature studies also can only be identified on regional scales. While a constant thickness can be reasonably assumed to estimate the depositional trend well, the choice of assigning the value 500 m in particular to Cretaceous package is simply based on a calculated average. Thicker or thinner average thickness cannot be disregarded as possibilities, and this will be addressed in section 2.3.

With a constant 500 m Cretaceous layer constructed, the K50, K80 and K100 sequences were accounted for the in the model through splitting of the layer into three layers. The K100 and K80 layers were both assigned a constant TVT of 100 m, and the remaining 300 m were assigned to the K50 sequence. This was based on the depth-denoted stratigraphic column from Grajales-Nishimura et al. (2003).

The J90 surface (base of J100 Tithonian source rock) was generated by shifting the J100 surface 200 m deeper, thus assigning a 200 m TVT to the J100 sequence. This was based on thickness values reported in literature studies, and these were introduced in detail in subsection 1.1.4. Lastly, the remaining J80 and J90 sequences were incorporated into the model by splitting the layer between the J90 and J60 surfaces into two layers, weighted by a splitting factor of 1/3 and 2/3 for the J90 and J80 sequences, respectively. This was based on the depth-denoted stratigraphic column from Grajales-Nishimura et al. (2003). This yielded average true vertical thicknesses of 211 m and 423 m for the J90 and J80 across the AOI, respectively. Table 2.1 summarizes the details regarding the pseudo-surfaces and layers generated for the model, and figure 2.12 provides a visualization of the finalized structural input for the base case thermal model. It is critical to note that the structural input does not include the Triassic-Lower Jurassic Clastic J50 sequence. This is because the base horizon of this sequence could neither be identified on the offshore 3D seismic dataset, nor was it available as one of the surfaces available from gravity data inversion modelling scheme. Moreover, it is also important to mention that the surface used to determine the top of J50/base of J60 horizon in the base case thermal model was taken from the gravity inversion results (see subsection 1.2.4) as opposed to the top of J50 surface available from the seismic data interpretation.

Age Assignment A key input for the thermal model was the numerical inputs for age information to ascertain the timing of sedimentary sequence deposition. For any particular layer, the specific ages assigned to its base horizon (top horizon for the underlying sequence) as well as to its top horizon determine the geological time period over which the sequence of interest was deposited at a constant deposition (linear) rate. The deposition duration, in combination with sequence/layer thicknesses at each lateral location, serve as key input parameters (among others) for the reconstruction of the burial history of the sedimentary model through a process known as *back-stripping*. Details regarding the mathematical bases for the back-stripping process can be found in subsection 2.2.5.

The age information for all horizons of interest were modified from the tectono-stratigraphic ages presented by Shann et al. (2020), which were based originally on the International Chronostratigraphic (ICS) chart from Cohen et al. (2021). The assigned ages are presented in table 2.2 (left).

Source Rock Properties and Maturation Kinetics Assignment The source rock properties required as a fundamental input for the thermal model include Hydrogen Index (HI) and Total Organic Carbon (TOC). Uniform TOC and HI values were assigned to the entire source rock layer in the model based on literature suggestions (see subsection 1.1.4). The assigned values are listed in table 2.2 (right).

Further critical input parameters for the source rock, particularly for a thermal maturity model, are the source rock

Horizon	Surface Source	Layer	True Vertical Thickness [m]
Top Upper Cretaceous K100	Seismic Interpretation		
		K100	100
Top Middle Cretaceous K80	K100 + 100 m		
		K80	100
Top Lower Cretaceous K50	K100 + 200 m		
		K50	300
Top Tithonian J100	K100 + 500 m		
		J100	200
Top Kimmeridgian J90	J100 + 200 m		
		J90	211 (average)
Top Oxfordian J80	Layer splitting		
		J80	423 (average)
Top Bajocian J60	Seismic Interpretation		

Table 2.1: **Summary of the pseudo-surfaces and corresponding layers generated to set up the structural input in accordance with the tectono-stratigraphic sequences introduced in subsection 1.1.3.**
Note: The '+' indicates an increase in depth.
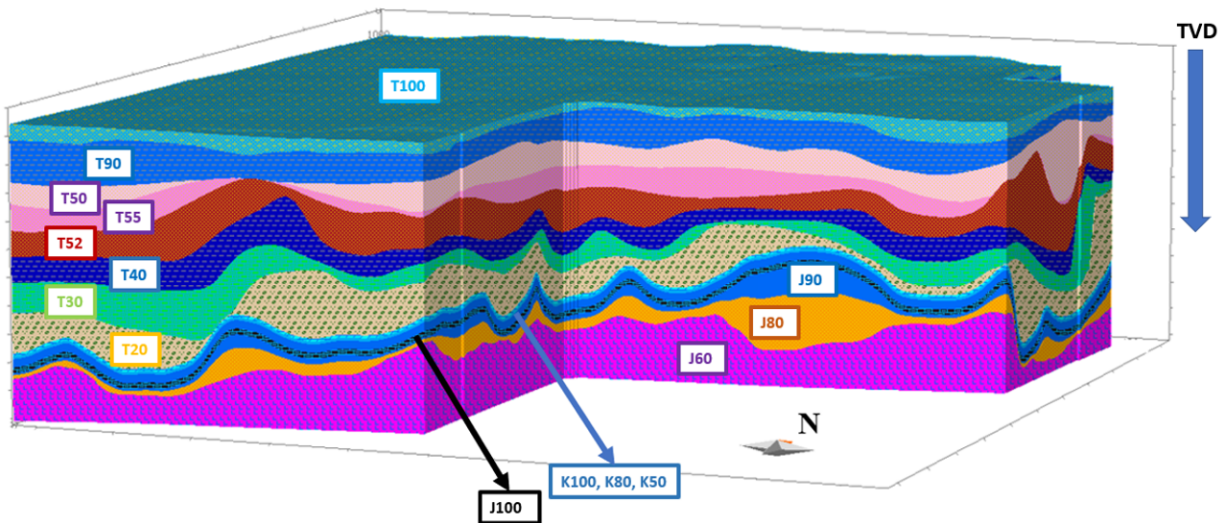
Figure 2.12: **Final structural input for the base case thermal model.** The layers have been overlain with patterns specific to the lithological mix ascribed to each layer.
Note: The true vertical depth (TVD) values have been hidden due to confidentiality requirements of Wintershall Dea GmbH.

maturation kinetics parameters. These parameters govern the molecular reactions that determine the conversion of kerogen into hydrocarbon upon heating to determine the key output parameter of interest for this study, namely the Transformation Ratio (TR). The aforementioned parameters include:

- The frequency factor (A), which represents the frequency of collisions between reactant molecules at a standard concentration.

- The activation energy (E_a), which represents the energy required by reactant molecules to initiate the chemical reaction.

- The absolute (reaction) temperature (T).

- The rate constant (k), which represents the frequency of collisions that actually result in a reaction taking place.

The relationship between the maturation kinetic parameters is described by the well-known Arrhenius equation (expressed via equations 2.1 and 2.2):

Top Horizon	Age [Ma]
T100	0.00
T90	1.80
T50	5.33
T55	11.63
T52	15.97
T40	23.03
T30	33.90
T20	47.80
K100	66.00
K80	93.90
K50	113.00
J100	145.00
J90	152.10
J80	157.30
J60	168.30
J50 (Model Base Horizon)	170.30

Source Rock	HI [mg/g TOC]	TOC [%]
Tithonian J100	600	5

Table 2.2: Left: **Age assignment to the top horizons for the various layers/sequences of the thermal model.**
Right: **Hydrogen Index (HI) and Total Organic Carbon (TOC) values assigned to the Tithonian J100 source rock.**

$$k = AF \qquad (2.1) \qquad\qquad F = e^{-E_a/RT} \qquad (2.2)$$

In equation 2.2, e is simply the Euler's number and R is the universal gas constant. The term F in the equations represents the fraction of collisions that have enough energy to overcome the activation barrier i.e. the collisions that have energy greater than or equal to E_a at T and therefore lead to the reactants chemically reacting. In petroleum geochemistry, F represents the fraction of kerogen converted to hydrocarbons as a function of T and E_a and therefore equals the transformation ratio (TR).

The kinetics parameter values used for this study were determined through laboratory geochemical analyses by Santamaria Orozco (2000) for the Type-IIS Kerogen Tithonian source rock in the Campeche area. The key parameter relationships from lab tests from the study are graphically represented in the the two sub-figures in figure 2.13. In the left sub-figure, the F or TR is shown as a function of activation energy. Based on a heating rate of 9.6 °C/Ma (extrapolated from laboratory timescales to geological timescales), the analysis revealed that most of the Tithonian source rock kerogen breaks down into hydrocarbons (oil) - a process known as *catagenesis* - when the activation energies reach the 51 - 55 kcal/mol range, with peak transformation occurring at 54 kcal/mol. The temperature range within which catagenesis results in near 100 % transformation is approximately 80 - 200 °C, given the aforementioned heating rate (see right sub-figure). The laboratory results also revealed a single frequency factor A of approximately 4.57×10^{14} s^{-1} (or 1440×10^{25} Ma^{-1}). For a more thorough review of the Tithonian source rock maturity kinetics, see Santamaria Orozco (2000).

The laboratory-derived relationships (extrapolated for geological timescales) serve as the bases for calculating the TR during simulations based on the simulated temperatures that the source rock is exposed to.

Lithology Assignment   Lithology assignment is a crucial model construction step, since further properties of interest for the layers - for example, porosities, thermal conductivities, heat capacities, radiogenic heat generation potential, mechanical compaction curves etc. - can be calculated for the model based on the lithology (or lithological mix) assigned to each layer (see subsection 2.2.3). In the absence of well and core data that would ideally provide accurate descriptions of the lithologies (and associated variations across the AOI) for all layers at sufficiently small depth intervals, uniform lithologies (spatially invariable) were assigned to an entire layer (no variations with depth) for all the layers for the base case model. Lithological mixes were created for most layers based on the descriptions provided in subsection 1.1.3. From the qualitative descriptions, percentages of contributing lithologies to a lithological mix were deduced. The mixes were created in the Lithology Editor interface for PetroMod©, and were then assigned to their
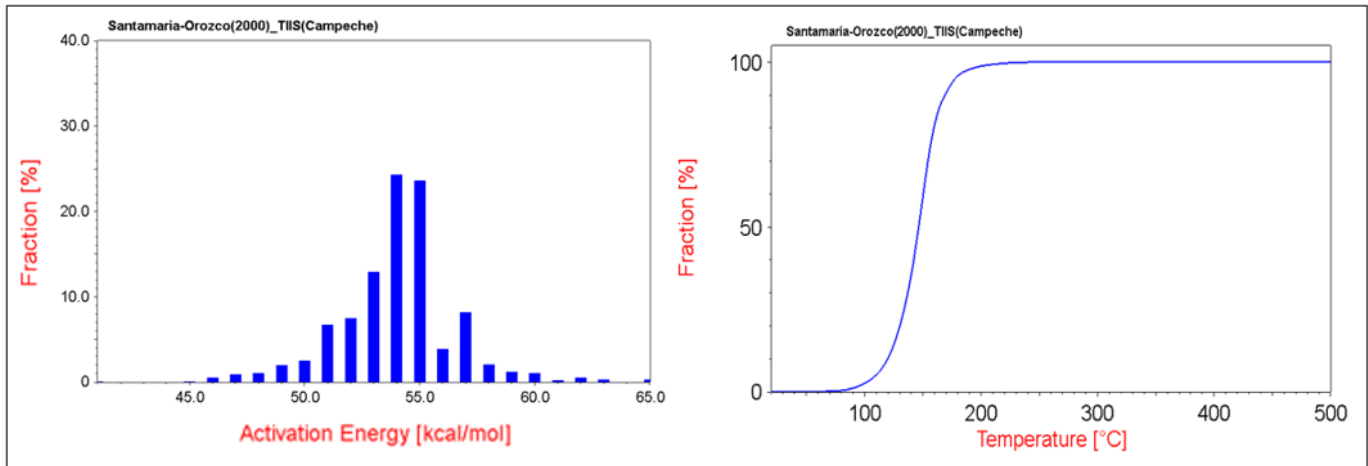
Figure 2.13: **Source rock maturity kinetics information sourced from Santamaria Orozco (2000).** The term *fraction* on the y-axes represents the parameter F or TR. For more details on the sub-figures, please read the corresponding text.

corresponding layer in the PetroBuilder 3D interface. It is important to note that all contributing lithologies to the final mixes were already available in the Lithology Editor as pre-defined lithologies. The final lithologies assigned to each layer are listed in table 2.3.

Layer	Lithology	Contribution [%]	Layer	Lithology	Contribution [%]
T100	Clay-rich sandstone	70	T20	Conglomerate	60
	Shale	15		Shale	20
	Organic-lean siltstone	15		Shaly limestone	20
T90	Shale	70	K100	Dolomite	70
	Sandstone	30		Conglomerate	30
T50	Sandstone	60	K80	Shaly Limestone	100
	Shale	30			
	Chalky limestone	10			
T55	Sandstone	80	K50	Dolomite	70
	Shale	15		Shaly limestone	30
	Chalky limestone	5	J100	Chalky limestone	25
T52	Sandstone	60		Shaly limestone	25
	Shale	30		Marl	25
	Chalky limestone	10		Shale	25
T40	Shale	35	J90	Dolomite	50
	Shaly limestone	35		Ooid Grainstone (Limestone)	30
	Sandstone	15		Shaly limestone	20
	Chalky limestone	15	J80	Sandstone	60
T30	Shale	40		Clay-rich sandstone	30
	Shaly limestone	40		Dolomite	5
	Sandstone	10		Ooid Grainstone (Limestone)	5
	Chalky limestone	10	J60	Halite	100

Table 2.3: **Lithological mixes for each layer in the base case thermal model.**

2.2.3   Model Parameters of Interest

Vitrinite Reflectance (%R₀) $\%R_0$ is a common maturity indicator used to determine whether the rock is immature, is in the oil or gas window, or is overmature. $\%R_0$ values are derived from geochemical analyses conducted in laboratories and are often used as calibration data for thermal modelling studies, during which simulated $\%R_0$ values are compared to the laboratory-derived values. For the base case thermal model, the Easy$\%R_0$ maturity model de-

veloped by Sweeney & Burnham (1990) was used to calculate the $\%R_0$. The mathematical basis for this model is given in equations 2.3 and 2.4. In equation 2.4, F describes the extent of the reaction, w_0 signifies the initial concentration of the total reactants, and w signifies the current concentration of total reactants at a certain reaction extent. It is important to note that principally, the parameter F (or TR) from equations 2.4 and 2.2 are the same, and therefore $\%R_0$ is theoretically dependent on TR; however, PetroMod$^©$ calculates $\%R_0$ independent of TR, using the kinetics parameters given in figure 12 in the appendix. This is to allow for maturation simulations of the source rock even when hydrocarbon generation via kerogen conversion is user-defined to not be simulated. Since F has a direct dependence on the reaction temperature corresponding to a certain activation energy, $\%R_0$ and TR can be understood to reflect the maximum temperature conditions to which the source rock was exposed to through its burial history.

$$\%R_0 = e^{-1.6+3.7F} \qquad (2.3) \qquad\qquad F = 1 - \frac{w}{w_0} \qquad (2.4)$$

Mechanical Compaction - Porosity Trend The porosities of the lithological mixes when uncompacted (depth = 0 m) were calculated using an arithmetic mean, as shown in equation 2.5. Here, $\phi_{ari,0}$ signifies the surface (uncompacted) porosity of the lithological mix of a respective layer, $\phi_{i,0}$ indicates the surface porosity of a constituent lithology contributing to the mix, and n signifies the total number of constituent lithologies in a mix. Depth dependence of porosities of the lithological mixes due to mechanical compaction was accounted for through the use of the compaction model presented by Athy (1930). This is given in equation 2.6. Here, $\phi_{ari}(z)$ is the porosity of the mix at depth z, and k is the Athy's compaction coefficient for the lithological mix. For any lithological mix, the compaction coefficient was deduced through an arithmetic mean (k_{ari}) of the individual pre-defined k_i values for each constituent lithology i of the total n constituent lithologies using equation 2.7. The factor f was introduced into the compaction model, which defines a minimum porosity condition during porosity calculations. Without this factor, porosity values would converge to zero with increasing z, which is a geologically unreasonable scenario. The factor c was assigned a value of unity for all porosity calculations for this study.

$$\phi_{ari,0} = \frac{1}{n} \sum_{i=1}^{n} \phi_{i,0} \qquad (2.5)$$

$$\phi_{ari}(z) = e^{-zk_{ari}} \phi_{ari,0} + f \qquad (2.6) \qquad\qquad k_{ari} = \frac{1}{n} \sum_{i=1}^{n} k_i \qquad (2.7)$$

The $\phi_{ari,0}$ and k_{ari} for each lithological mix corresponding to each layer in model is shown in table 2.4.

Thermal Conductivity The bulk thermal conductivity of each constituent lithology was calculated as a geometric average as shown in equation 2.8, which accounted for porosity variation due to compaction. Here, $\lambda_{b,z}$ denotes the bulk thermal conductivity of the lithology at depth z, λ_{mat} signifies the matrix thermal conductivity, and λ_{fl} signifies the thermal conductivity of the pore fluid. Note that this equation is independent of temperature (detailed below).

$$\lambda_{b,z} = \lambda_{mat}^{1-\phi(z)} \lambda_{fl}^{\phi(z)} \qquad (2.8)$$

The bulk thermal conductivities for each lithological mix were determined through a geometric mean, which was calculated as shown in equation 2.9. In equation 2.9, at any given porosity $\phi(z)$, $\lambda_{i,20}$ is the bulk thermal conductivity at 20 °C of each constituent lithology contributing to the lithological mix, N is the total number of constituent lithologies, and n is the volume fraction of constituent lithology i. Standard $\lambda_{i,20}$ values already calculated in the Lithology Editor were used to calculate the bulk $\lambda_{geo,20}$ (bulk thermal conductivity of the lithological mix at 20 °C) at the given $\phi(z)$.

$$\lambda_{geo,20} = \prod_{i=1}^{N} \lambda_{i,20}^{n_i} \qquad (2.9)$$

Temperature dependence of thermal conductivities was also accounted for based on the Sekiguchi (1984) model. This is shown in equation 2.10. Here, $\lambda_{geo}(T)$ denotes the bulk thermal conductivity of the lithological mix at temperature

T at any given z and $\phi(z)$.

$$\lambda_{geo}(T) = 1.84 + 358(1.0227\lambda_{geo,20} - 1.882)\left(\frac{1}{T} - 0.00068\right) \qquad \textbf{Note: } \text{T in } K \qquad (2.10)$$

The aforementioned functions were used to compute *vertical* thermal conductivities only. In order to account for anisotropy within the lithological mixes, an anisotropy factor (α) was used to calculate the horizontal (bulk) thermal conductivity at temperature T ($\lambda_h(T)$) at any given $\phi(z)$. The governing relationship between the vertical (bulk) thermal conductivity ($\lambda_v(T)$) at temperature T, $\lambda_h(T)$, and α is shown in equation 2.11. Values for α for lithological mixes were also calculated through a geometric mean (analagous to equation 2.9) of individual α values for constituent lithologies pre-defined in the Lithology Editor, and were independent of T. The $\lambda_{v,20}$, $\lambda_{h,20}$ and α for the lithological mixes assigned to each layer are shown in table 2.4.

$$\lambda_h(T) = \alpha\lambda_v(T) \qquad \text{where} \qquad \lambda_v(T) = \lambda_{geo}(T) \qquad (2.11)$$

It is useful to mention that a geometric mean was used for equations 2.8 and 2.9 as opposed to an arithmetic mean since the former most accurately approximates the bulk thermal conductivities in cases of homogeneous mixes compared to true values (Fuchs et al., 2013), and is therefore offered as a default calculation method for homogeneous mixes in PetroMod©. Moreover, according to Hartmann et al. (2005), the effective thermal conductivity of a lithological mix is best approximated by an arithmetic mean if the heat flow is parallel to the layering. For this study, the vertical heat flow (considered to be more perpendicular than parallel to the layering) can be considered predominant due to the highest temperature differences in the vertical orientation. Therefore, a geometric mean was considered more suitable. For all other parameters calculated via arithmetic means as described earlier or later in this subsection, this is the case since PetroMod© only allows arithmetic mean calculations for these parameters; in mathematical terms, this implies that the highest possible (mean) values for all of these parameters are used for further calculations (Benson, 2015). While this is merely one way to derive single values for any parameter for lithological mixes, in the broader context, the differences between parameter values attained via arithmetic versus geometric means can be reasonably assumed to have relatively much smaller impacts on the maturity indicator parameters of interest relative to other governing parameters such as the thermal boundary conditions (see subsections 2.2.4 and 2.2.5). Therefore, these arithmetic averages can be understood to offer reasonably representative values for the lithological mix parameters for the purposes of this study.

Layer	$\phi_{ari,0}$ [%]	k_{ari}	$\lambda_{v,20}$ [W/m/K]	$\lambda_{h,20}$ [W/m/K]	α
T100	46.8	0.42	2.80	3.62	1.30
T90	61.3	0.67	2.13	3.10	1.45
T50	52.6	0.53	2.94	3.71	1.26
T55	46.8	0.42	3.41	4.10	1.20
T52	52.6	0.53	2.94	3.71	1.26
T40	57.9	0.65	2.29	3.36	1.46
T30	58.3	0.65	2.17	3.31	1.52
T20	41.6	0.45	2.15	2.70	1.26
K100	33.5	0.36	3.51	3.71	1.06
K80	48.0	0.50	2.30	3.91	1.70
K50	38.9	0.42	3.51	4.28	1.22
J100	59.5	0.68	2.16	3.10	1.43
J90	37.6	0.30	3.37	4.06	1.21
J80	40.1	0.30	3.72	4.32	1.16
J60	1.0	NA	6.50	6.56	1.01

Table 2.4: **Values for the parameters of interest for the lithological mixes assigned to the 15 layers of the thermal model.** See corresponding text for more details.
Note: Halite has limited porosity and is incompressible; the minimum porosity condition (factor $f = 1\%$) was applied and the Athy's compaction coefficient was not available.

Temperature Distribution and Geothermal Gradient   The temperature distributions were calculated within the model with the assumptions of steady-state conditions as well as with the neglection of heat transport via advection;

as such, the temperature distribution was governed by the simplified 3D heat conduction equation, shown in equation 2.12, which can be numerically solved using finite element approximations within the model domain. Here, T is the temperature distribution as a function of time and space (i.e. $T = T(x, y, z, t)$), and λ_x, λ_y and λ_z are the thermal conductivities in the x, y, and z directions i.e. anisotropy is considered. The R_{gen} is source term within the equation that represents the radiogenic heat production rate per unit volume. Calculation of the latter parameter is discussed later in this subsection.

$$\frac{\partial}{\partial x}(\lambda_x \frac{\partial T}{\partial x}) + \frac{\partial}{\partial y}(\lambda_y \frac{\partial T}{\partial y}) + \frac{\partial}{\partial z}(\lambda_z \frac{\partial T}{\partial z}) + R_{gen} = 0 \qquad (2.12)$$

The *Fourier's Law of Thermal Conduction* provides the principle equation that relates the heat flow to the thermal gradients (Beardsmore et al., 2001) in the subsurface via the thermal conductivities. This equation is provided in equation 2.13. Here, T and q denote the temperature distribution and heat flow, respectively. As was the case for equation 2.12, λ_x, λ_y and λ_z are the thermal conductivities in the x, y, and z directions. It is important to mention that q in equation 2.13 theoretically denotes the *heat flux* (W/m^2) because it describes a heat transfer per unit time (J/s or W) normalized to the cross-sectional area (m^2) over which the heat is transferred (Elison, 2015). Still, since the term "heat flow" has been adopted as the standard in PetroMod$^©$ and has been extensively used in literature studies, it will be used henceforth in this study as well. Lastly, the negative sign in the equation mathematically represents the physical phenomenon of heat flow down the temperature gradient (Sobota, 2014).

$$q = -\left(\lambda_x \frac{\partial T}{\partial x} + \lambda_y \frac{\partial T}{\partial y} + \lambda_z \frac{\partial T}{\partial z}\right) \qquad (2.13)$$

Radiogenic Heat Production The thermal model accounts for radiogenic heat production within the sedimentary column due to the presence of radioactive elements Uranium (U), Thorium (Th), and Potassium (K) in varying concentrations in various lithologies. The generated radiogenic heat is considered in summation with the basal heat flow ascribed as the lower boundary condition to calculate temperature conditions in the model. For each pre-defined lithology in the Lithology Editor, pre-defined standard values for U, Th and K exist, which can then be used to calculate the matrix heat flow production values for the respective lithology following the Rybach (1973) equation (see equation 2.14). Here, $Q_{r,m}$ is the matrix heat flow production value and ρ_{mat} is the matrix density.

$$Q_{r,m} \ [\text{μW/m}^3] = \left(\rho_{mat} \ [\text{kg/m}^3](9.52U \ [ppm] + 2.56Th \ [ppm] + 3.48K \ [\%])\right) \times 10^{-5} \qquad (2.14)$$

The $Q_{r,m}$ for a particular lithology can then be converted to bulk heat flow production rates ($Q_{r,b}(\phi)$) by simply multiplying the matrix values with $(1 - \phi(z))$ for any given depth z. From there, at each given $\phi(z)$ value, the bulk heat flow production rate of any lithological mix ($Q_{r,b,ari}(\phi)$) can be calculated as an arithmetic mean of $Q_{r,b}(\phi)$ of all individual contributing lithologies. This is shown in equation 2.15, where n is the total number of contributing lithologies and $Q_{r,b,i}(\phi)$ denotes the bulk heat flow production rate of a contributing lithology i at a given $\phi(z)$ value. Note that $Q_{r,b,ari}(\phi)$ has the units mW/m^3 and equates the R_{gen} in equation 2.12.

$$Q_{r,b,ari}(\phi) = \frac{1}{n} \sum_{i=i}^{n} Q_{r,b,i}(\phi) \qquad (2.15)$$

2.2.4   Paleo-Water Depth and Sediment-Water Interface Temperature Trends

The paleo-water depth (PWD) trend is the main parameter that governs the paleo-geometry of the model (Hantschel & Kauerauf, 2009). This trend directly impacts:

- The sediment-water interface temperature (SWIT); this is because the model implicitly assumes a density-driven stratification of the water column, which is directly impacted by the temperature. Therefore, lower water temperatures are reasonably assumed at deeper depths.

- The lithospheric thinning through calculations of crustal and mantle stretching (β) factors (see subsection 2.2.5 for more details).

Numerical inputs for the paleo-water depths through time were deduced from the qualitative descriptions of the paleo-depositional environments (see subsection 1.1.3 and paleogeographic maps in the appendix). For the Cretaceous period in particular, biostratigraphic information through an analysis of benthic foraminiferal assemblages revealed

PWD values in the order of 1300 m in the present-day onshore Mexico regions (Alegret & Thomas, 2005). These values agree with the paleobathymetric profiles for the Middle Cretaceous presented by Winker & Buffler (1988) for the Campeche region as well as with the paleogeographic maps for the Cretaceous presented in the appendix. The final PWD trend assigned to the model is shown in table 2.5. It is useful to notice that the present-day PWD is simply the surface available for the top of the T100 sequence. For the PWD trend before present, constant values were assigned to the entire AOI. The trend is generated by linearly interpolating between the assigned PWD values at different times.

Time [Ma]	Geological Time	Paleo-water Depth [m]
0.00	Present Day	T100 surface
23.03	Late Oligocene	600
33.90	Late Eocene	600
56.00	Late Paleocene	800
66.00	Late Upper Cretaceous	1000
93.90	Middle Cretaceous	1300
145.00	Late Tithonian (Upper Jurassic)	1000
152.10	Late Kimmeridgian (Upper Jurassic)	500
157.30	Late Oxfordian (Upper Jurassic)	50
170.30	Bajocian (Middle Jurassic)	1250
240.00	Middle Triassic	50

Table 2.5: **PWD trend assigned to the base case thermal model.**

The SWIT serves as the upper thermal boundary condition for the model. This corresponds to the Dirichlet boundary condition in numerical modelling of a system's thermodynamics (Arendt & Warma, 2003). The assignment for SWIT for the model is facilitated by the global mean surface temperature model integrated into the PetroBuilder 3D interface, which is based on Wygrala (1989). The model requires present-day latitudinal information of the AOI as well as geographical information regarding the hemisphere and the continent within which the AOI is located. The model output is a trend for temperature at paleo sea levels at the AOI over geological time. This trend can then be corrected for the PWD to generate the SWIT trend. Assigning a latitude of 21 °N, the generated sea level temperature trend can be seen in figure 2.14 (left sub-figure). The PWD and SWIT trends at the C-1 well location are also shown in figure 2.14 (right sub-figure).
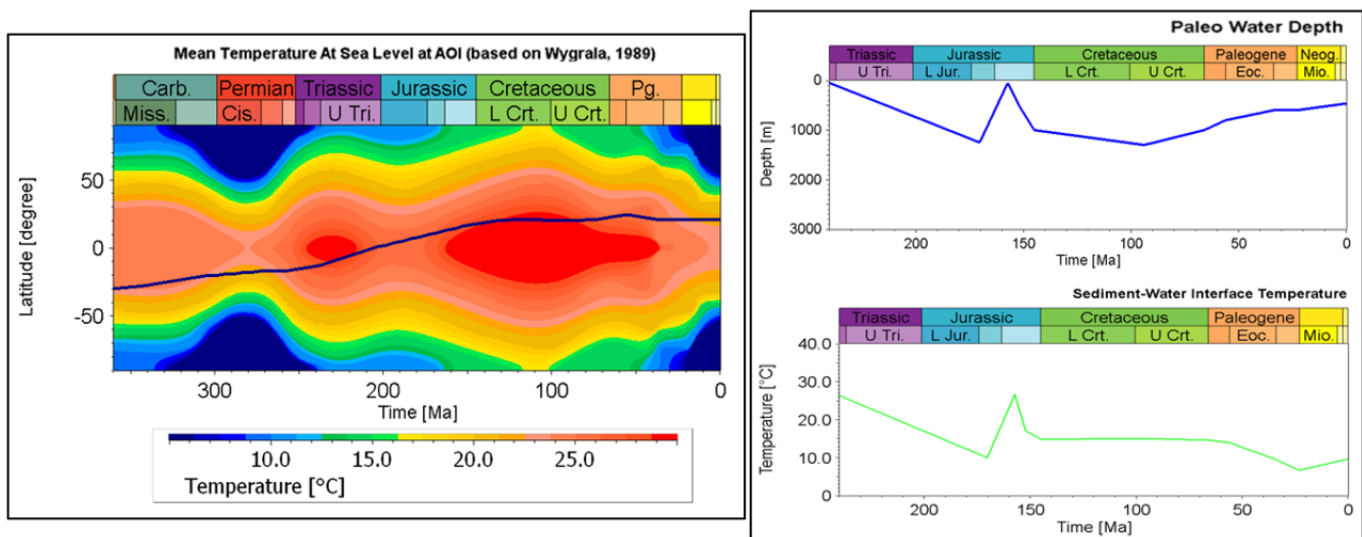

Figure 2.14: Left: **Temperature at paleo sea levels at the AOI through geological time.**
Right: **PWD and SWIT trends at the C-1 well location.**

2.2.5   Crustal Model - Lower Thermal Boundary Condition

A lower thermal boundary condition was also necessarily needed for the model base, which dictates the thermal conditions the model is subjected to over geological time (alongside SWIT). Typically, a basal heat flow is assigned at the model base over geological time, which corresponds to the assignment of a Neumann boundary condition (Arendt & Warma, 2003). However, such a boundary condition only works reasonably successfully in the presence of sufficient maturity (vitrinite reflectance) calibration data across the entire depth interval of interest, such that the maturity values can be interpreted to have mimicked the thermal history of the sedimentary sequences. This then allows adjustment of the exact values assigned to the basal heat flow trend, which is originally set up such that it generally showcases higher heat flow values during known rifting events and lower heat flow values during known compressional events (Allen & Allen, 2013). In the absence of such maturity data, as was the case for this study, only a quantitatively imprecise basal heat flow trend could have been assigned. As an alternative, a crustal model was set up using the available surfaces for the Moho and the base of the upper crust for the present day (see subsection 1.2.4). The top of the upper crust was assumed at the base of the autochtonous salt J60 layer. Additionally, a value of 175 km for the depth of the lithosphere-asthenosphere boundary (LAB) in the present was extracted from Hamza & Vieira (2012) based on the longitudinal and latitudinal information of the AOI; a depth map covering the entire AOI was assigned this value in PetroBuilder 3D. With all the aforementioned surfaces, three layers for the upper crust, lower crust, and the mantle lithosphere were implicitly generated within PetroBuilder 3D to finalize the present-day crustal model structural setup (figure 2.15). Next, lithologies were assigned to the upper crust, lower crust and mantle lithosphere.
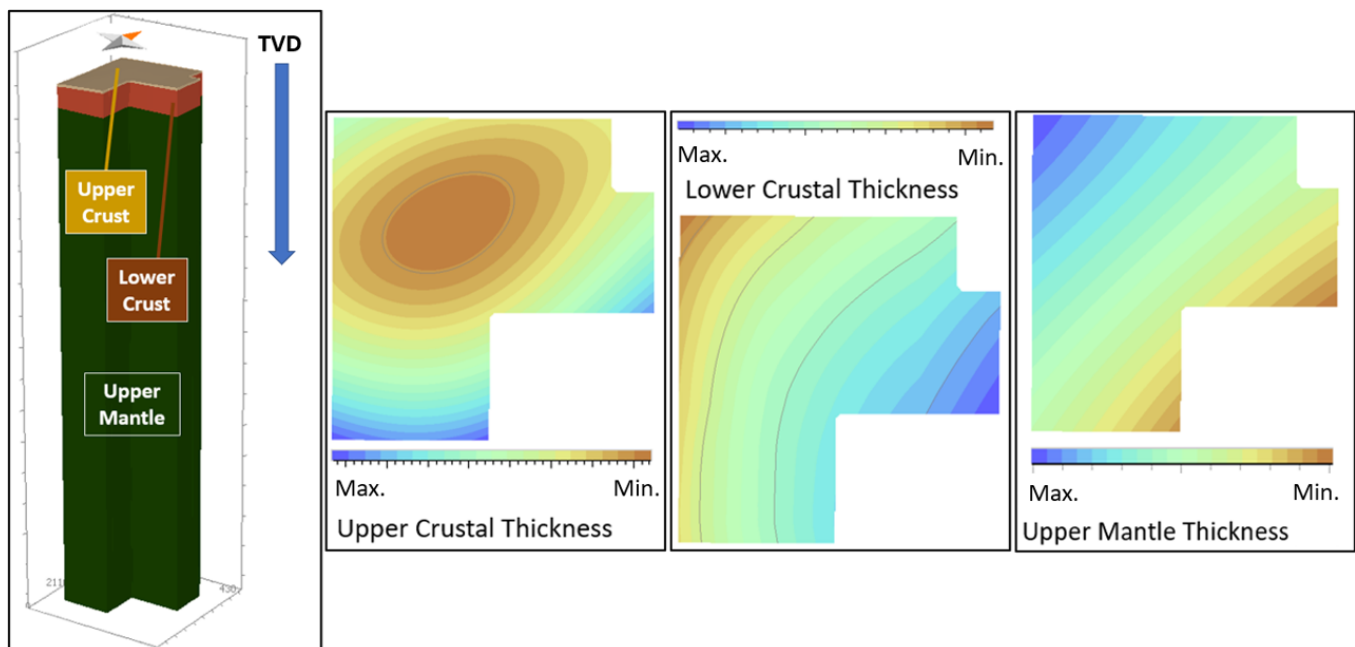

Figure 2.15: **The present-day crustal model structural setup and layer thicknesses**. The 3D setup on the left has no vertical exaggeration. All surfaces contributing to the layers have been clipped outside the AOI.
Note: The true vertical depth (TVD) values have been hidden due to confidentiality requirements of Wintershall Dea GmbH.

No mixes were created, and the standard lithologies available in PetroMod$^{\copyright}$ for these layers were used to assign to the layers of interest. Note that for the upper and lower crust, standard continental crust lithologies were assigned (for reference, see figure 1.3). The lithologies and their (standard) respective properties are shown in table 2.6. Following this, the crustal modelling workflow summarized in figure 2.16 was followed to ascertain the lower thermal boundary condition.

Present-Day Crustal Model and Heat Flow Calibration   Firstly, the present-day lithospheric structure was assumed to have existed throughout the geological time of relevance for the model (240 Ma to present). Using this structure, a temperature of 1333 °C (Allen & Allen, 2013) was assigned at the LAB. Using the SWIT and LAB fixed temperatures at the top of sedimentary sequence model (thermal model) and at the base of the crustal model respectively, a basal heat flow (at the base J60 sequence of the thermal model) was calculated as the lower thermal boundary condition (Neumann) for the thermal model by numerically solving 2.13 and the multi-1D heat flow equation

Layer	Lithology	$Q_{r,b}$ [µW/m³]	$\lambda_{v,20}$ [W/m/K]	α	$\lambda_{h,20}$ [W/m/K]
Upper Crust	Granite	2.50	2.60	1.15	2.99
Lower Crust	Diorite	2.50	2.70	1.00	2.70
Upper Mantle	Peridotite	0.00	4.00	1.00	4.00

Table 2.6: **Standard lithologies and respective properties for upper crust, lower crust and mantle lithosphere for the crustal model pre-defined in PetroMod©.**
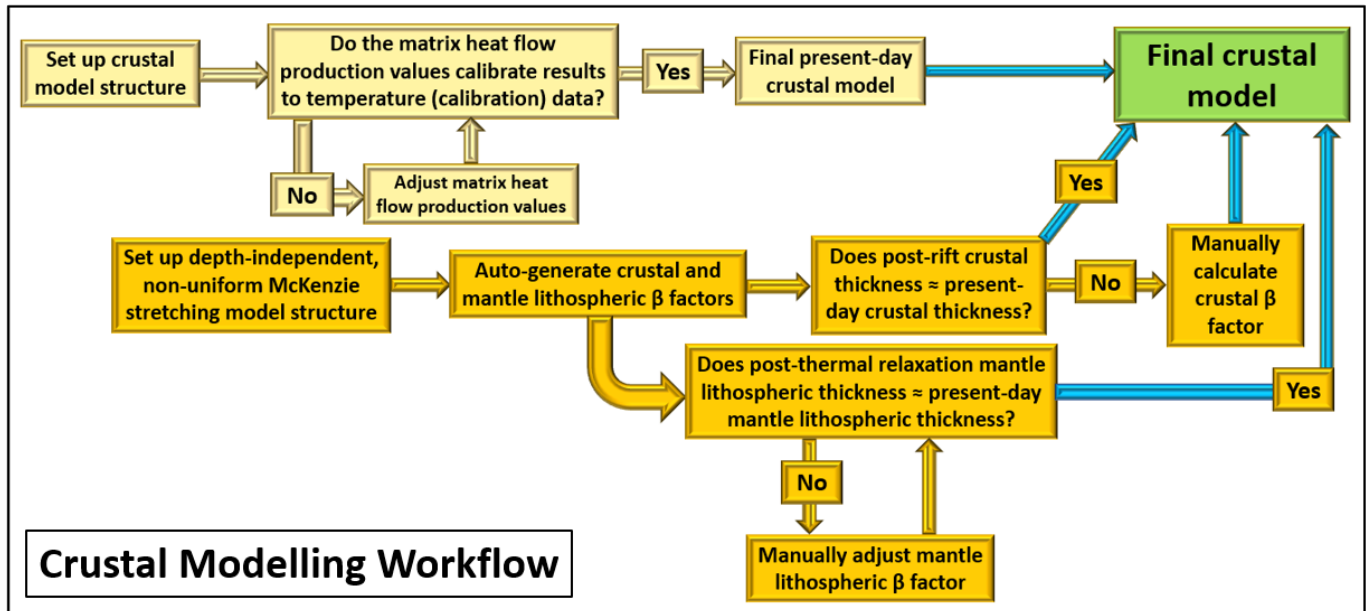

Figure 2.16: **Crustal modelling workflow to determine the lower thermal boundary condition through time.**

(equation 2.12 but with lateral heat flow via conduction assumed to have not occurred). Note that the $Q_{r,b}$ ($\approx Q_{r,m}$ at $\phi = 1\%$) for the upper and lower crust was also considered during the heat flow calculation. Radiogenic heat contribution from the mantle was reasonably assumed to be negligible. Next, again numerically solving equation 2.12 alongside equation 2.13, the temperature distribution and geothermal gradient was calculated for the sedimentary layer model through geological time. It was noted that the available present-day temperature calibration at the C-1 well location did not match the simulated present-day temperature trend at the location, and therefore the the crustal radiogenic heat flow production values were adjusted such that $Q_{r,b} \approx Q_{r,m} = 3.80\,\mu\text{W/m}^3$ for both the upper and lower crusts. It is important to note that while with these values the basal heat flow and corresponding sedimentary model temperature-depth trends calibrated well to the calibration data (see figure 2.17), assigning higher $Q_{r,b}$ values in the upper crust relative to the lower crust is more geologically reasonable (Jaupart et al., 2016). This was not done due to a few reasons. Firstly, there were no constraints available on what $Q_{r,b}$ values were in fact reasonable in absolute terms for the upper and lower crusts in the specific region; thus, increasing only the upper crust $Q_{r,b}$ for calibration introduced the risk of geological inconsistency as well. Secondly, since only the basal heat flow was the actual parameter of interest to calibrate the present-day simulated temperature trends, how the $Q_{r,b}$ values were setup to be distributed across the crust were only of secondary importance as long as the calibration could be achieved. In sub-figure C of figure 2.17, the basal heat flow is lower in the direction of crustal thinning due to rifting associated with the Pangaean continental breakup; the thinning leads to smaller volumes over which the radiogenic heat is produced.

Finite Duration, Depth-Independent Non-Uniform McKenzie Model To determine the spatial evolution of the lithosphere due to the Pangaean breakup rifting event, a finite duration (Jarvis & McKenzie, 1980), depth-independent and non-uniform (Royden & Keen, 1980) implementation of the McKenzie (1978) model was utilized. The term *non-uniform* entails differing stretching factors for the crust (β_c) and upper mantle (β_{ml}), and the term *depth-independent* entails constant values (i.e. not a function of depth) for β_c and β_{ml} within their respective media. Available as an integrated tool within the PetroBuilder 3D interface of PetroMod©, the *McKenzie Inversion* tool required inputs regarding pre-rift crustal and mantle lithospheric thicknesses, ages for the start and end ages of active rifting and post-rift thermal relaxation, and lithologies for the upper crust, lower crust and upper mantle. This input
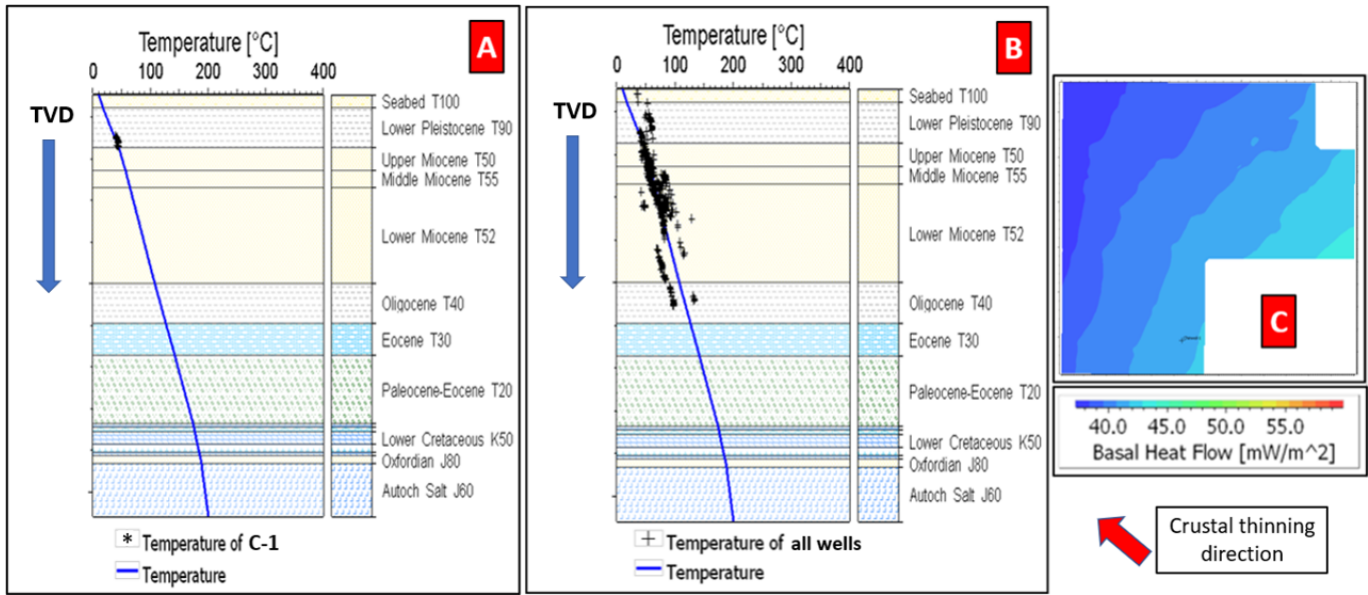
Figure 2.17: Sub-figure A: **Temperature gradient at C-1 well location shown to be calibrated against present-day temperature data obtained from the well.**
Sub-figure B: **Temperature gradient at C-1 well location shown to be compliance with the regional temperature trend from all available wells within the Campeche area.** Well names kept anonymous as per confidentiality requirements.
Sub-figure C: **Basal heat flow in the present calculated from the crustal model.**

information is summarized in table 2.7.

Pre-rift Crustal Thickness [km]	Pre-rift Mantle Lithosphere Thickness [km]	Start Rift Age [Ma]	End Rift Age [Ma]	End Thermal Relaxation Age [Ma]
30	145	240	163	93.9

Table 2.7: **Pre-rift lithospheric structural setup for the finite duration, depth-independent non-uniform McKenzie model implementation.**

The pre-rift crustal thickness value for the tool was obtained from literature studies that estimated the thicknesses in present-day onshore regions in southern, central and south-central Mexico, as well as in eastern GOM. This was done with the reasonable assumption that the present-day crustal thicknesses in inland continental regions surrounding the GOM are reflective of the pre-rift thicknesses prior to the Pangaean continental breakup. Christeson et al. (2014) reported crustal thicknesses in the range of 28 - 29 km landward at the Florida margin of eastern GOM. Hales (1969) interpreted average crustal thicknesses of around 32 km in central Mexico. Rodríguez-Domínguez et al. (2019) reported crustal thicknesses in the order of 30 km in south-central Mexico. Lastly, Iglesias et al. (2001) reported an average crustal thickness of approximately 33 km in central Mexico, and 28 km in southern Mexico. Noting the general agreement of these values, an average pre-rift crustal thickness value of 30 km was assigned to the pre-rift crustal scenario in the inversion tool. Next, following the description of of crustal thinning during rifting presented by McKenzie (1978), the pre-rift mantle lithospheric thickness was simply calculated as the difference between present-day depth of the LAB and the pre-rift crustal thickness. This yielded a pre-rift mantle lithospheric thickness value of 145 km. The assignment of the start and end ages for rifting and thermal relaxation was based on the information provided in 1.1.2. The lithological input needed for the inversion tool has already been provided in table 2.6.
The inversion scheme used can be subdivided into two main steps (Baur & Littke, 2010):

1. A *theoretical subsidence* curve was back-calculated based on the *back-stripping* equation from Steckler & Watts (1978), which is shown subdivided in equations 2.16 and 2.17 for a multi-layer model case. The process of backstripping essentially involves a sequential "stripping" or removal of the top most layer of the sedimentary column (from the present-day backwards) at the respective time steps based on assigned ages to estimate the depth of upper crust through time relative to the present-day sea level. The equations implicitly take into consideration sediment decompaction due to unloading as a result of layer removal (Athy's law, equation 2.6),

changes in paleo-water depth (which in turn also impact loading on underlying sedimentary column), and density-driven local isostatic compensation such that sediment- and water-loading in themselves are understood to contribute to subsidence in addition to rifting-related subsidence. In equation 2.16, Y is the tectonically driven subsidence i.e. the depth to the basement (relative to the present-day sea level) at the starting point in time of the deposition of the top-most layer in the backstripping process, S is the uncompacted ($\phi(z)$ at $z = 0$ m) thickness of the stripped layer, ρ_m and ρ_w are the densities of the mantle and water, respectively, W_d is the (paleo-)water depth at the time of deposition of the stripped layer, and Δ_{SL} is the difference in sea-level height between the present day and at the time at which the respective layer was deposited. In equation 2.17, L_j signifies the (de-compacted) thickness of each individual layer constituting the sedimentary column underneath the top most stripped layer such that the denominator in the equation represents the thickness (with de-compaction accounted) of the entire remaining sedimentary column after removal of the top layer. Moreover, ϕ_j is the porosity of layer j in the sedimentary column and ρ_g is the grain/matrix density of the layer j.

$$Y = S\left[\frac{(\rho_m - \rho_s)}{(\rho_m - \rho_w)}\right] + W_d - \Delta_{SL}\left[\frac{\rho_m}{(\rho_m - \rho_w)}\right] \tag{2.16}$$

$$\rho_s = \frac{\sum_{j=1}^{l} L_j[\phi_j\rho_w + (1 - \phi_j)\rho_g]}{\sum_{j=1}^{l} L_j} \tag{2.17}$$

2. With the theoretical subsidence curve at all lateral locations in the AOI (back-)calculated, a *calculated subsidence* curve at all locations was forward-computed using the pre-rift information (described earlier) based on a finite duration, non-uniform and depth-independent implementation of the mathematical formulation of the McKenzie (1978) model. For details on these formulations, please refer to the cited literature studies. The calculated subsidence is computed such that a best possible fit with the theoretical subsidence is iteratively achieved. As a result of the calculated subsidence curves for all locations, which account for tectonic and thermal (post-rift thermal relaxation related) subsidence, β_c and β_{ml} are calculated for all locations. These stretching factors then determine the thickness of the crust and mantle at each time step, thereby determining the volume over which the radiogenic heat flow production rate ($Q_{r,b}$) is calculated at each time step (relevant for the crust), while also determining the position of the LAB to establish the location of the 1333 °C isotherm for the basal heat flow (lower thermal boundary condition) calculation at each time step.

From the first run, β_c and β_{ml} calculated did not yield crustal and mantle lithospheric thickness in the order of the known thicknesses in the present day (figure 2.15). Based on the crustal modelling workflow (figure 2.16), a manually calculated $\beta_{c,man}$ distribution in the AOI was calculated based on equation 2.18, following the McKenzie (1978) formulation.

$$\beta_{c,man} = \frac{\text{Pre-rift Crustal Thickness}}{\text{Present-day Crustal Thickness Distribution}} \tag{2.18}$$

The resulting $\beta_{c,man}$ is shown in figure 2.18. The β_{ml} was also manually adjusted with each successive run to yield post-thermal relaxation mantle lithospheric thicknesses (93.9 Ma to present) as close to the thickness distribution shown in figure 2.15 as possible. A manual calculation for this factor was not possible since this would require a known relationship between the amount of thinning and the amount of thermal-relaxation induced thickening post-rifting for the AOI; such information was not available. The modelling results with a manually adjusted constant $\beta_{ml,man} = 1.1$ across the AOI yielded mantle lithospheric thicknesses in the order of 115 km across the AOI at the end of the thermal relaxation period (93.9 Ma). These values had a discrepancies in the order of 40 km relative to the known present-day mantle lithospheric thicknesses (figure 2.15). A lower value of $\beta_{ml,man} = 1.0$ would indicate no mantle lithospheric stretching syn-rift which is a geologically unrealistic scenario (particularly given the $\beta_{c,man}$ distribution in figure 2.18). Hence, a final value of $\beta_{ml,man} = 1.1$ was used.

Final Crustal Model and Basal Heat Flow Crustal thickness maps for different time steps computed were used for the final model for the basal heat flow calculation. For the mantle lithosphere, the thicknesses from the inversion tool were used till the time steps before 93.9 Ma. From 93.9 Ma till the present, the present-day mantle lithospheric thickness maps were used to override the inversion tool results to add reliability to the basal heat flow calculations. This was done since LAB based on present-day thickness maps is known to be located deeper compared to its estimated location based on the inversion tool thickness maps. A discussion on the uncertainty in the modelling results due to the mantle lithospheric inversion tool-derived thickness maps assigned till 93.9 Ma can be found in section 4.2.3. Final
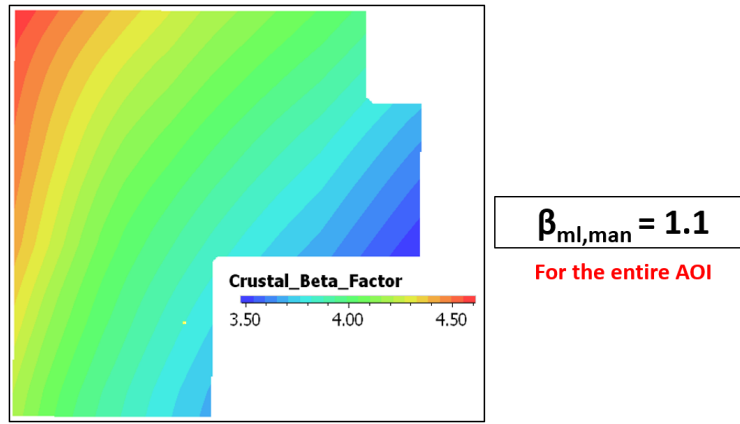
Figure 2.18: **The $\beta_{c,man}$ calculated using equation 2.18 and $\beta_{ml,man} = 1.1$.** The crustal thickness maps through time associated with this $\beta_{c,man}$ distribution were considered as the crustal thickness input for the final crustal model.
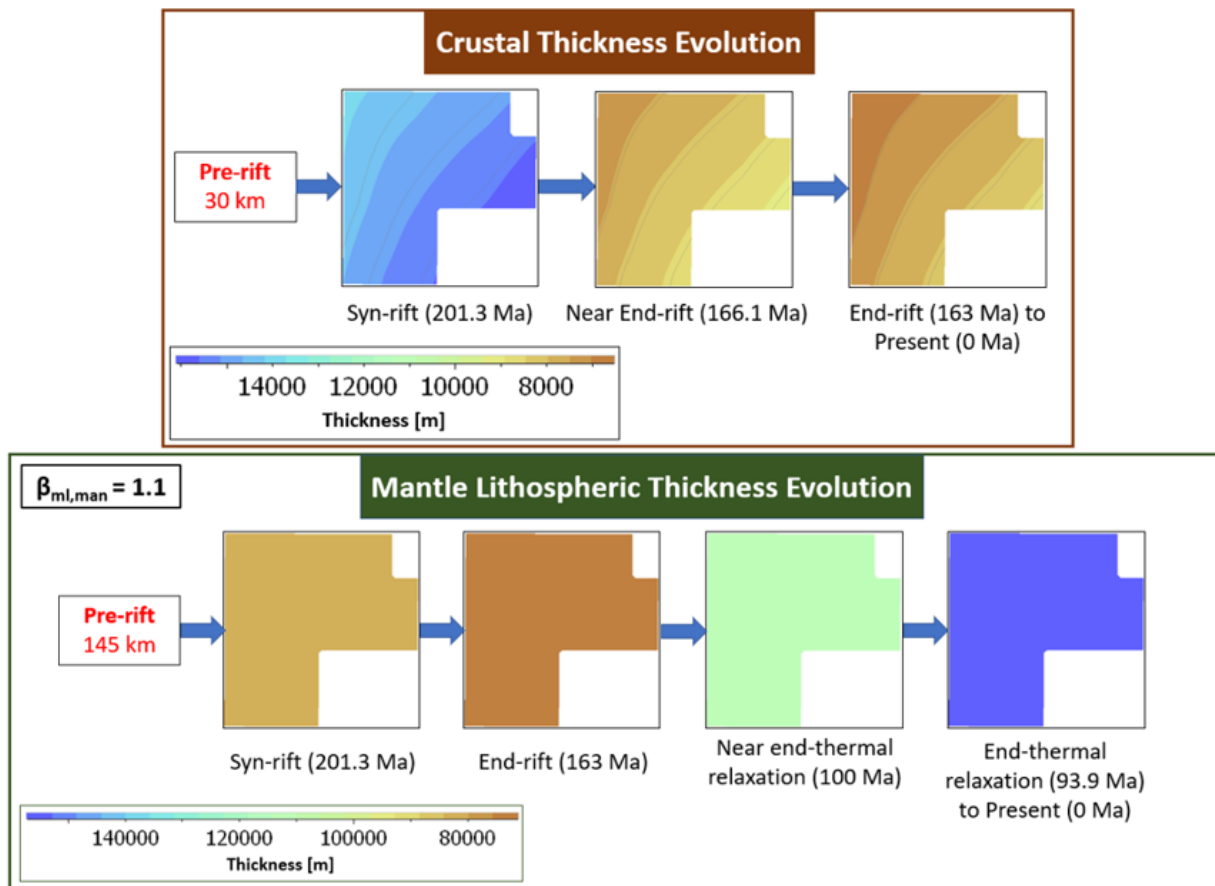

Figure 2.19: **Crustal and mantle lithospheric thickness maps (at key time steps) used for basal heat flow calculations for the base case thermal model.** Note that finer thickness variations within each mantle lithospheric thickness map are not visible due to the wide thickness range for the legend.

crustal and mantle lithospheric thickness maps used at a select few time steps for the basal heat flow calculation for the base case thermal model are shown in figure 2.19. Note that the crustal thickness distributions across the AOI at each time step include a summation of the lower and upper crust thicknesses.

As described earlier, the basal heat flow was again calculated for each time step using the multi-1D heat equation and equation 2.13, now with rift-related lithospheric temporal and spatial variation accounted for. The basal heat flow distribution distribution at six different time steps is shown in figure 2.20. As expected, the basal heat flow is the highest at 168.3 Ma in the range of $56\,\mathrm{mW/m^2}$ to $60\,\mathrm{mW/m^2}$, with values lower where the crust has been thinned more

(see figure 2.18). The generally higher basal heat flow at this time relative to other time steps is due to the uplift of the 1333 °C isotherm alongside large temperature gradients due to limited vertical separation (see equation 2.13) between the base (basal heat flow deduced temperatures) and top (SWIT) of the sedimentary column at all lateral locations. From 163 Ma to 93.9 Ma, the post-rift thermal relaxation period occurs which leads to the thermal equilibration of the 1333 °C. This, coupled with more sediment deposition leading to decrease in vertical temperature gradients leads to a strong reduction in the basal heat flow. From 93.9 Ma to 66 Ma, limited changes in the basal heat flow values and spatial distribution are observed. This can be attributed to post-thermal thermal relaxation stage during which no changes in lithospheric parameters now govern the basal heat flow changes. Also, with only 200 m of sediment deposited during this time, limited decrease in the vertical temperature gradients results in limited decrease in basal heat flow. From 66 Ma to present-day, considerable sediment deposition reduces vertical temperature gradients, thereby incrementally reducing basal heat flow through time. It is critical to note that changes in thermal conductivities of the sedimentary column at each lateral location due to deposition of new layer(s) in addition to compaction-related changes in conductivities at each time step indeed contribute to changes in basal heat flow according to equation 2.13; this however only has a second-order contribution. Moreover, the variations in the SWIT across the AOI through time also dictate changes in subsurface temperature gradients and hence heat flow.
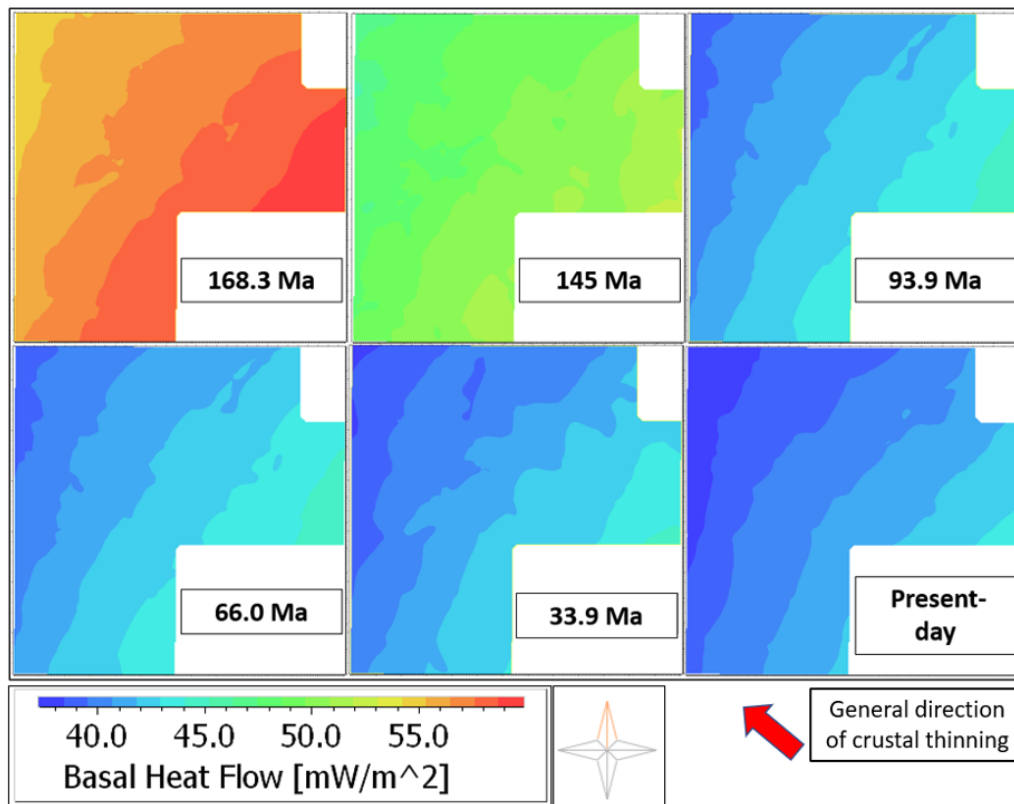

Figure 2.20: **The basal heat flow calculated at six different time steps using the crustal modelling workflow.** See corresponding text for more details.

2.2.6   Model Simulation and Key Assumptions

Lateral Boundary Condition   A lateral boundary condition in addition to upper and lower (thermal) boundary conditions needs to be ascertained for model simulation. In PetroMod$^{©}$, a no-flow boundary condition is automatically adopted i.e. $q = 0 \, \text{mW/m}^2$, which corresponds to the Neumann condition. With this condition, a mirrored version of the model with the same thermal properties at each time step is implicitly assumed on all lateral boundaries (Elison, 2015), thereby explaining the lack of heat flow. Such a condition is merely an assumption necessitated by the modelling method, and can lead to over-estimations of simulated temperatures at the boundaries due to the lack of horizontal heat flow in the boundary orientation. Table 2.8 summarizes the boundary conditions used in the modelling scheme.

Pore Fluid, Fluid Movement, and Hydrocarbon Migration   For all layers in the thermal and crustal models, PetroMod$^{©}$ assumes pore spaces to be filled with water, unless otherwise specified. The thermal conductivity of water

Position	Condition	Governing Model Parameter
Lateral	no-flow (Neumann)	NA (implicitly assumed)
Upper	fixed temperature (Dirichlet)	SWIT
Lower	heat flow (Neumann)	Basal Heat Flow

Table 2.8: **Summary of the boundary conditions used for the modelling scheme.**

$\lambda_{w,20}$ at $20\,°C$ is taken to be $0.6\,W/m/K$, which is then utilized for bulk thermal conductivity calculations for layers using equation 2.8. Though λ_w indeed itself has a temperature dependence, with numerical relationships presented in many literature studies to account for this (for example, see Touloukian et al. (1970) and figure 6 in Sharqawy et al. (2010)), this temperature dependence was not explicitly accounted for. Rather, it is implicitly considered using equation 2.10. Moreover, pore fluid movement within the pore spaces was not accounted for (as is implicitly already considered in equation 2.12 through the consideration of heat conduction only). Pore fluid movement is a phenomenon driven by a number of factors such as buoyancy, thermal expansion, migration due to compaction, topographically driven flow etc. Fluid transport in turn affects heat transport associated with fluid movement. A lack of such a consideration could in theory lead to greater temperature stratification in the model, thereby leading to potential overestimations in maturity calculations. The reason for fluid transport not being accounted for involves uncertainties in the multitude of factors impacting it. For example, fluid movement pathways may often include (open) faults, structural features not included in the thermal model. Fluid movement is also dependent on porosities defined for all layers; without proper porosity calibrations, fluid transport-driven heat transport adds another dimension of uncertainty within the modelling results. Lastly, fluid transport-driven heat transport also depends on the structural trends of the model; the thermal model 1) excludes key features such as allochtonous salt diapirs/canopies and 2) adopts a simplified depositional history that disregards the structural evolution affected by compressional events in the AOI. These factors too contribute to uncertainties in temperature field alterations via fluid transport. Coupling these examples with suggestions in literature studies regarding thermal conductivity being the main heat transport mechanism in similar subsurface depth levels of interest (Elison, 2015; Allen & Allen, 2013), heat transport via fluid movement was neglected.

Hydrocarbon expulsion and migration was also not accounted for in the model. Factors described above for advection not being accounted for also supported this assumption. In particular, since the faults (typical migration pathways) and allochtonous salt bodies (typical structures for trap formation) were ignored, simulations of hydrocarbon migration and accumulation would not have realistically represented actual scenarios through time.

Steady-State Thermal Conditions   As already implied in equation 2.12, the model assumes steady-state thermal conditions through time. The validity of such an assumption, according to Smith et al. (1978), needs to be *"judged a posteriori"* according to the *"supposed duration of the geological processes responsible for the thermal condition[s]"*. For this study, such an assumption was considered to offer a fair approximation of the heat flow evolution through time given the amount of sediment deposition for the sedimentary sequences in relation to the duration over which they were deposited as well as to their respective thermal conductivities. Contrarily, such an assumption would offer relatively poorer approximations if there known features associated with the sedimentary section that slow down thermal equilibration in geological timescales e.g. the "continued" presence of thick such sheets in geological timescales (for example, see (Elison, 2015)); such sheets effectively act as very good insulators (Elison, 2015), thus inhibiting relatively fast thermal equilibration.

Age Correction for Radioactive Decay   In the case of radiogenic heat flow production values being calculated using equation 2.14 on the basis of known/pre-defined present-day concentrations of radioactive elements U, Th, and K in a particular lithology, PetroMod$^{©}$ allows radioactive decay to be accounted for using equations 2.19, 2.20 and 2.21 to calculate paleo-concentrations $U_p(t)$, $Th_p(t)$, and $K_p(t)$ at each time step. In these equations, t is given in Ma. The paleo-values calculated can be used as inputs for equation 2.14 to calculate time-dependent matrix heat flow production values ($Q_{r,m}$).

Such age correction was not accounted for within the sedimentary layers of the thermal model due to the uncertainty in the present-day element concentrations, since standard PetroMod$^{©}$ present-day values were used that were not constrained by, for example, (spectral) gamma ray logs from wells within the AOI. Incorporating time-dependence was therefore understood to add further uncertainty, and was therefore neglected. For the crustal model radiogenic heat contribution, production rates were manually adjusted (see subsection 2.2.5) and not calculated based on element concentrations; therefore age correction could not be applied to the crustal model by default.

$$U_p(t) = U[1 + (2.77 \times 10^{-4}t) - (7.82 \times 10^{-8}t^2) + (4.53 \times 10^{-12}t^3)] \qquad (2.19)$$

$$Th_p(t) = Th(e^{0.00005t}) \tag{2.20}$$

$$K_p(t) = K(e^{0.000555t}) \tag{2.21}$$

Diagenesis and Other Processes   Diagenetic processes are key subsurface processes at given temperature-pressure conditions that can lead to further compaction of the layers (in additional to mechanical compaction) such that re-arrangement of matrix grains can lead to loss in porosities, or in cases of chemical dissolution, even gain in porosities. Such processes were not accounted for due to the lack of mineralogical, petrophysical and geochemical data availability for pre-integrated diagenesis models within PetroMod$^{\copyright}$, such as the ones based on Schneider et al. (1996) and Walderhaug (2000). For similar data availability related reasons, other higher-order processes such as secondary organic porosity generation due to the a reduction in volume during kerogen cracking in the source rock (A. Brown, 2019) (thereby altering bulk thermal conductivities) were also disregarded during simulation.

Local Erosional Unconformities   The local erosional unconformities formed as a result of the uplifting caused by the Middle Miocene Chiapaneco event (see subsection 1.1.2) were identifiable for the T52 and T55 sequences in some areas within the AOI). Such local unconformities were not accounted for in thermal model, firstly, due to it being a purely depositional model with no thrusting events accounted for. Without this consideration, an erosional event in the thermal model would entail greater deposited thicknesses in a paleo-setting that were aerially exposed and hence eroded, which is not representative of the thrusting-related uplift of the sequences that led to the local erosional unconformities. Secondly, a lack of available information regarding the actual amount of eroded sediments in these localized areas also inhibited incorporation of local unconformities in the model.

2.3   OAT Sensitivity Analyses

The *one-at-a-time* (OAT) sensitivity analysis approach involves assessing the impact of the variations in input values of a single parameter on the model results at a time (Wainwright et al., 2014). Sequentially, more parameters can be tested this way in isolation. While the OAT approach is useful to quantitatively understand changes in the (base case) model results as a function of a single parameter, it does not allow testing of all possible permutations of the input parameters value ranges and their interdependence. The latter can be achieved through *global sensitivity analyses* (GSA), though this approach can be computationally very intensive (Degen et al., 2021). For the purpose of this study, the OAT approach was adopted for reasons provided in section 1.3.

2.3.1   A1 and A2 - Cretaceous Package Thickness

While the assignment of 500 m to the entire Cretaceous package was rooted in literature suggestions, different thickness values for this package could not be definitively disregarded given the unavailability of seismic-well tie information as well as structural and stratigraphic markers to identify the top of J100 sequence on the seismic dataset across the AOI. This is of importance for maturity evaluations since this directly impacts the present-day depth at which the Tithonian J100 source rock is set up in the model. Therefore, minimum and maximum Cretaceous thickness scenarios were tested by limiting the package thickness to 200 m in the first case (A1), and extending it to 700 m in the second case (A2), based on literature suggestions (see subsection 2.2.2). For both cases, the layer splitting conducted to account for the K100, K80 and K50 sequence thicknesses followed the same splitting ratios as for the base case model i.e. 20 %, 20 % and 60 % of the total package thickness for the K100, K80, and K50 sequences, respectively. Moreover, in both the cases, the changes in Cretaceous thicknesses were compensated for by changes in the thicknesses of the J90 and J80 sequences formed through layer splitting. The thickness of the J100 sequence was kept at 200 m throughout, and the top of J60 autochtonous salt sequence available from seismic interpretation was not moved. The layer splitting for the J90 and J80 followed a thickness split of 1/3 and 2/3, respectively, as was also the case for the base case model. The summary of the layer setups for both cases is shown in table 2.9.

2.3.2   B - J60 Autochtonous Salt Thickness

Once the surface for the base of the upper crust surface had been obtained using the gravity inverse modelling scheme (see subsection 1.2.4), a base of J60 surface was introduced into "final" geological model geometry. This was done in order to refine the free-air gravity anomaly response of the model such that an even better fit with the measured anomalies could be attained. To this end, the initial base of J60 surface was set up in the model such that it mimicked

Horizon	Layer	Surface Source (Cretaceous = 200 m)	TVT [m] (Cretaceous = 200 m)	Surface Source (Cretaceous = 700 m)	TVT [m] (Cretaceous = 700 m)
Top K100		Seismic Interpretation		Seismic Interpretation	
	K100		40		140
Top K80		K100 + 40 m		K100 + 140 m	
	K80		40		140
Top K50		K100 + 80 m		K100 + 280 m	
	K50		120		420
Top J100		K100 + 200 m		K100 + 700 m	
	J100		200		200
Top J90		J100 + 200 m		J100 + 200 m	
	J90		312 (avg.)		145 (avg.)
Top J80		Layer splitting		Layer splitting	
	J80		623 (avg.)		290 (avg.)
Top J60		Seismic Interpretation		Seismic Interpretation	

Table 2.9: **Layer thicknesses with 200 m and 700 m Cretaceous package thicknesses assumed.** Layer splitting ratios were kept consistent with the base case model in subsection 2.2.2.
Note: The '+' indicates an increase in depth.

the final base of upper crust surface geometry, but with a uniform upwards shift of 1000 m. This initial geometry was then refined iteratively. This information is critical since it highlights the lack of true geological constraints on the initial geometry of this surface, which warrants the consideration in the thermal model of the base of J60 surface available from seismic interpretation. It is critical to note this base of J60 surface itself was not seismically constrained in many regions due to poor imaging quality at associated depths, hence requiring interpolations (see subsection 1.2.3). A comparison of the thickness distribution of the J60 sequence using both alternative surfaces is shown in figure 2.21. The figure clearly highlights differences in layer thickness distributions in the range of 300 - 900 m across the AOI. Such differences are expected to lead to variations in the thermal conditions of the sedimentary layer model through time due to salt thickness-related variations in geothermal gradients at each lateral location, and also due to variations in the basal heat flow calculations based on the crustal thicknesses through time, which is in turn based on the $\beta_{c,man}$ calculated for the rifting event. As shown in equation 2.18, $\beta_{c,man}$ is a function of the present-day crustal thickness, which itself is a function of the base of J60 surface geometry. Owing to these considerations, the crustal modelling workflow described in subsection 2.2.5 was once again followed, with the exception of adjustments to the matrix heat flow production values ($Q_{r,m} = Q_{r,b}$ at $\phi = 1\%$); such adjustments would incorrectly entail a different crustal lithology for this case. The manually calculated $\beta_{c,man}$ distribution for the AOI is shown in figure 2.22. Based on the $\beta_{c,man}$, the crustal thickness evolution was calculated using the McKenzie non-uniform depth independent model, and this is shown in figure 2.23, where the crustal thickness distribution at 163 Ma is the same as the present-day crustal thickness distribution. The mantle lithospheric evolution using $\beta_{ml,man} = 1.1$ was the same as shown in figure 2.19, since mantle lithospheric thicknesses are only dependent on the Moho and LAB geometry, both of which kept unaltered for this analysis.

Using the crustal and mantle lithospheric thickness evolutions, the basal heat flow was calculated through time; this is shown for six different time steps in figure 2.24. The basal heat flow is the highest at 168.3 Ma relative to the other time steps, with a range of 50 - 53 mW/m^2; this corresponds to the near end-rift time, where the 1333 °C isotherm is the shallowest in its evolution. The basal heat flow progressively decreases towards 93.9 Ma as the end of thermal relaxation is reached corresponding to the re-equilibration of the LAB, and as increasingly more sediments are deposited. Post-thermal relaxation, during which the heat generation accounted for by the crustal radiogenic heat production and the 1333°C LAB isotherm stays constant, the basal heat flow decreases through time owing primarily to thicker sedimentary columns which lead to a reduction in vertical temperature gradients. It is critical to note the differences in basal heat flow in figures 2.20 and 2.24. Higher syn-rift values and lower post-thermal relaxation values can be seen in figure 2.24. Since all factors such as sediment deposition trends (ages and thicknesses across AOI), SWIT trends, and thermal conductivities were kept constant for the two cases, the differences in the basal heat flow values can be attributed to the interplay between the lithospheric radiogenic heat production (crustal volume-dependent) and the spatial position of the LAB 1333 °C isotherm through time.
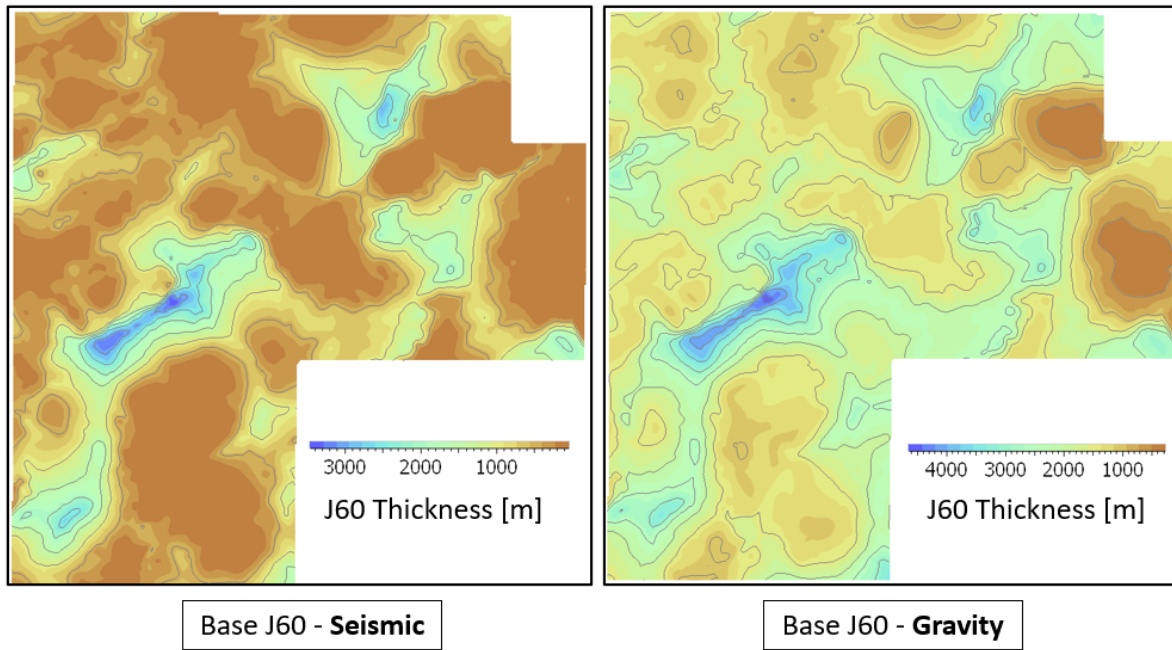
Figure 2.21: **Comparison of the J60 sequence thickness using the base J60 surface from seismic inter-pretation and gravity inversion results.** Generally, the latter surface yielded larger thicknesses across the AOI. See corresponding text for more details.
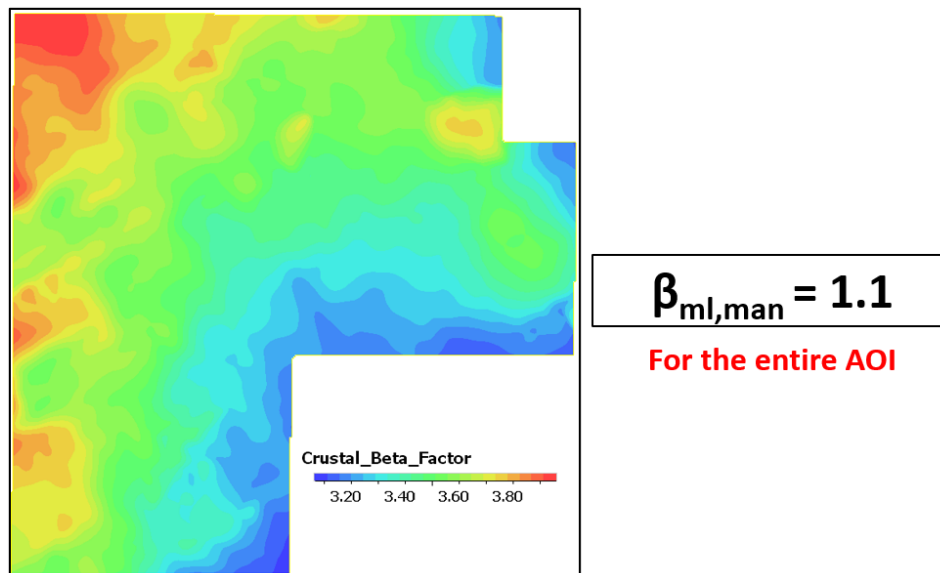

Figure 2.22: **The $\beta_{c,man}$ manually calculated for a relatively thicker present-day crustal thickness owing to the relatively thinner J60 sequence thickness compared to the base case.**

2.3.3   C - Layer-Splitting and Lithology Assignment

In the base case model, separation of sedimentary sequences was done following the tectono-stratigraphic sequence descriptions from Shann et al. (2020). While such a division allows the representation of lithological differences between various stratigraphic packages reasonably well, finer divisions in theory are always possible if adequate data for such subdivisions is available. For the base case model, various lithology contributions from finer sub-units of the sequences were accounted for by *homogeneous* lithological mixes assigned. For this analysis, sub-divisions into finer layers with varying lithologies was done to assess the differences in impact of such divisions on the thermal maturity distribution of the J100 source rock compared to the base case. Based on the qualitative descriptions of contributing lithologies in subsection 1.1.3, the layers in the thermal model representing T20, J100, J90 and J80 sequences were split into finer

layers, and new lithological mixes were created for each of these layers. This is shown in table 2.10. It is critical to note that the split percentage in the table determines the ratio of the original thickness ascribed to the respective split layer. This percentage also determines the splitting of the total deposition duration; for example, a split layer with 40 % the original thicker layer would also take 40 % of the deposition duration of the original layer to deposit. For completeness, the values for the parameters of interest (see subsection 2.2.3) for the split layers are also provided. Figure 2.25 shows the split layers overlain with their respective lithological patterns.
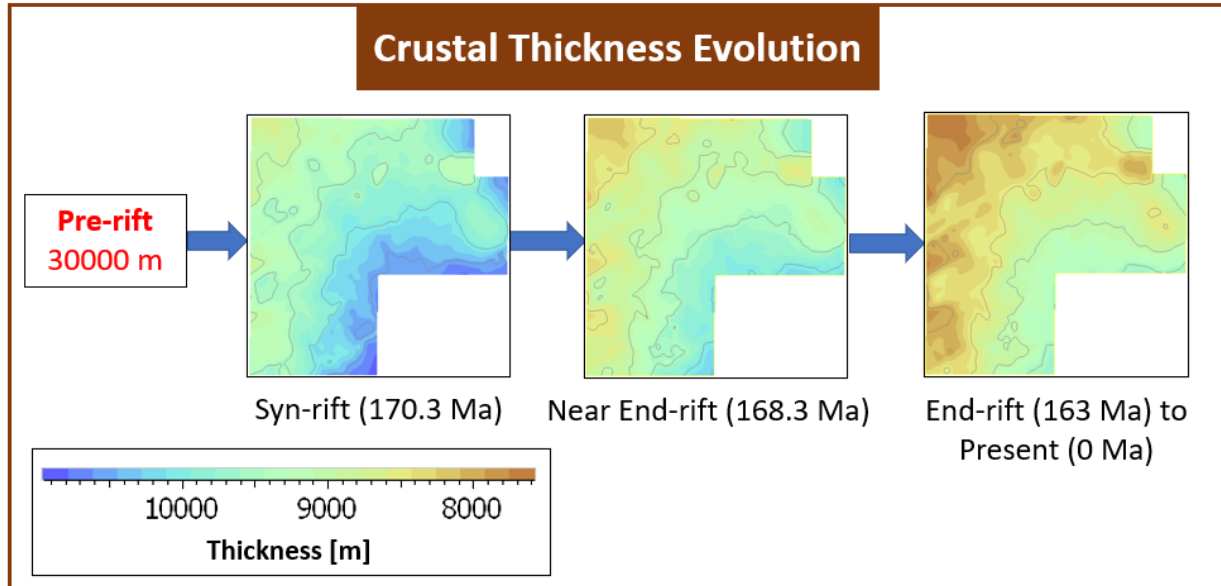

Figure 2.23: **Crustal thickness evolution (at key time steps) using the $\beta_{c,man}$ from figure 2.22.**
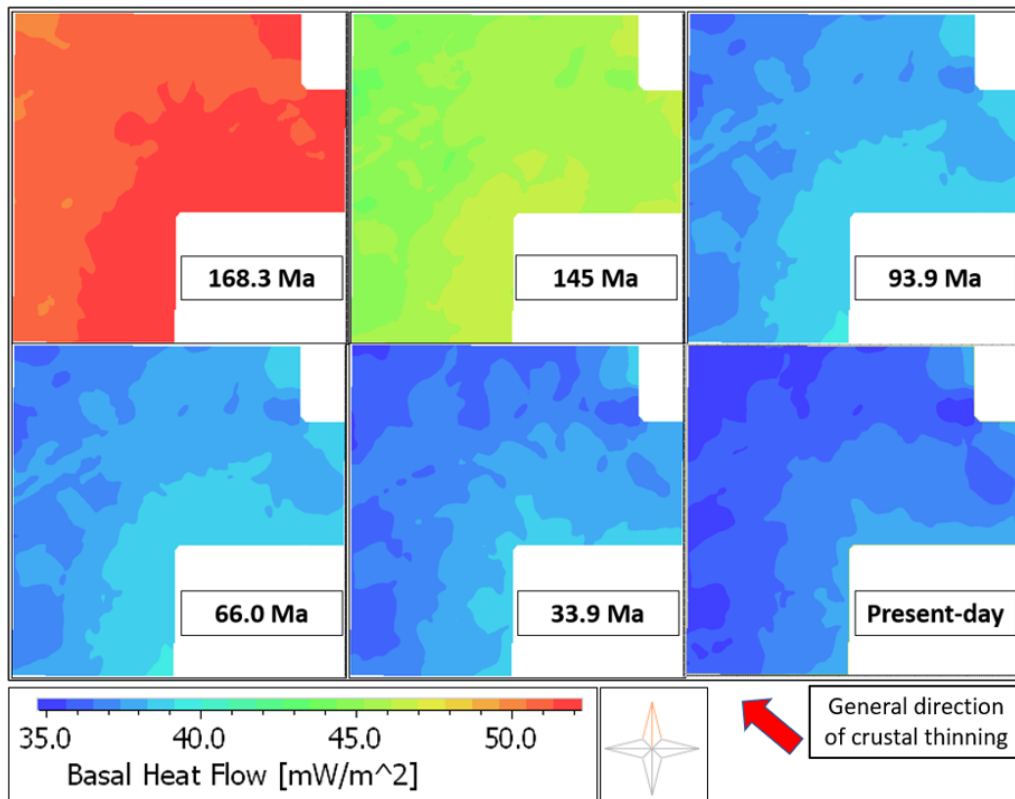
Figure 2.24: **The basal heat flow calculated at six different time steps using the crustal modelling workflow for the $\beta_{c,man}$ in figure 2.22**. See corresponding text for details.

Layer	Split [%]	Lithology	Contri- bution [%]	$\lambda_{v,20}$ [W/m/K]	$\lambda_{h,20}$ [W/m/K]	α	$\phi_{ari,0}$ [%]	k_{ari}
U. T20	40	Shale	50	1.94	3.20	1.65	59.0	0.67
		Shaly Limestone	50					
L. T20	60	Conglomerate	100	2.30	2.42	1.05	30.0	0.30
U. J100	20	Shaly Limestone	50	2.63	3.74	1.42	49.5	0.51
		Micritic Limestone	50					
M. J100	60	Organic lean, sandy Shale	80	1.92	3.72	1.94	61.6	0.76
		Shaly Limestone	20					
L. J100	20	Shaly Limestone	80	1.91	3.69	1.94	52.4	0.57
		Black Shale	20					
U. J90	25	Dolomite	100	4.20	4.45	1.06	35.0	0.39
U.M. J90	25	Shale	45	2.40	3.28	1.36	53.0	0.52
		Clay-rich Sandstone	45					
		Ooid Grainstone (Limestone)	10					
L.M. J90	25	Dolomite	45	3.29	3.83	1.16	38.5	0.26
		Ooid Grainstone (Limestone)	45					
		Shale	10					
L. J90	25	Shale	85	1.92	2.90	1.51	63.4	0.74
		Sandstone	5					
		Dolomite	5					
		Anhydrite	5					
U. J80	10	Ooid Grainstone (Limestone)	100	3.00	3.57	1.19	35.0	0.01
M. J80	80	Shale	60	2.27	3.19	1.41	57.8	0.59
		Sandstone	30					
		Ooid Grainstone (Limestone)	10					
L. J80	10	Clay-rich Sandstone	100	3.35	4.02	1.20	40.0	0.32

Table 2.10: **Information corresponding to the split T20, J100, J90 and J80 layers for the sensitivity analysis.**
Note: L = Lower, M = Middle, U = Upper.
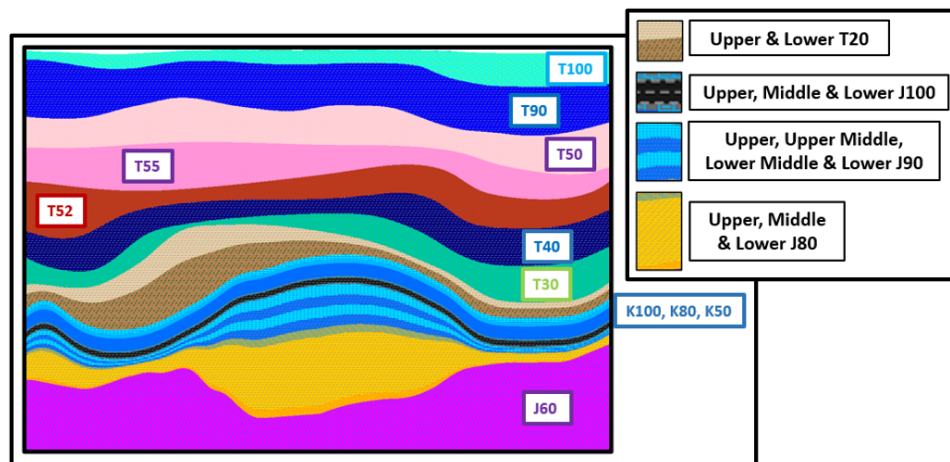
Figure 2.25: **Split layers based on the splitting percentages shown in table 2.10.**

2.3.4   D1 and D2 - Source Rock Maturity Kinetics

While the source rock maturity kinetics from Santamaria Orozco (2000) used for the base case model to calculate TR likely do approximate the kinetics of the Tithonian J100 source rock in the AOI, potential variations in the kerogen type and corresponding kinetic parameters cannot be ruled out definitively even within a single basin (Peters et al., 2018) without ample source rock samples from within the AOI being geochemically analyzed. To account for this, the most commonly used source rock maturity kinetics in basin and petroleum systems studies for Type-II and Type-IIS

kerogens from Pepper & Corvi (1995) were used (cases D1 and D2, respectively). The maturity kinetics from Pepper & Corvi (1995) serve as the average for the respective kerogen types, since geochemical analyses on 11 different source rocks for Type-IIS kerogen, and 16 different source rocks for Type-II kerogen from assorted basins were conducted to derive the averages. The key parameter relationships from lab tests from the study are graphically represented in the the four sub-figures for Type-II and Type-IIS kerogens in figure 2.26. Based on a (timescale-extrapolated) heat rating of 9.6 °C/Ma, the analysis for the Type-II kerogen revealed the onset of kerogen breakdown into oil as the activation energies reach 45 kcal/mol, with peak transformation into oil occurring at 52 kcal/mol. As can be understood from the figure, peak gas generation for Type-II kerogen approximately in the activation energy range of 65 - 67 kcal/mol. In terms of the temperature dependence of the transformation ratio, kerogen transformation into hydrocarbons occurs primarily in the temperature window of 100 - 200 °C.

For Type-IIS kerogen at a heating rate of 9.6 °C/Ma, onset of oil and gas generation from kerogen both coincide at 45 kcal/mol activation energies, with peak generation for both occurring at 49 kcal/mol; this emerges in stark contrast to the laterally displaced activation energy distribution for the Type-II kerogen in figure 2.26. The temperature dependence of kerogen transformation reveals that most of the kerogen gets converted into hydrocarbons within a temperature window of 90 - 170 °C.
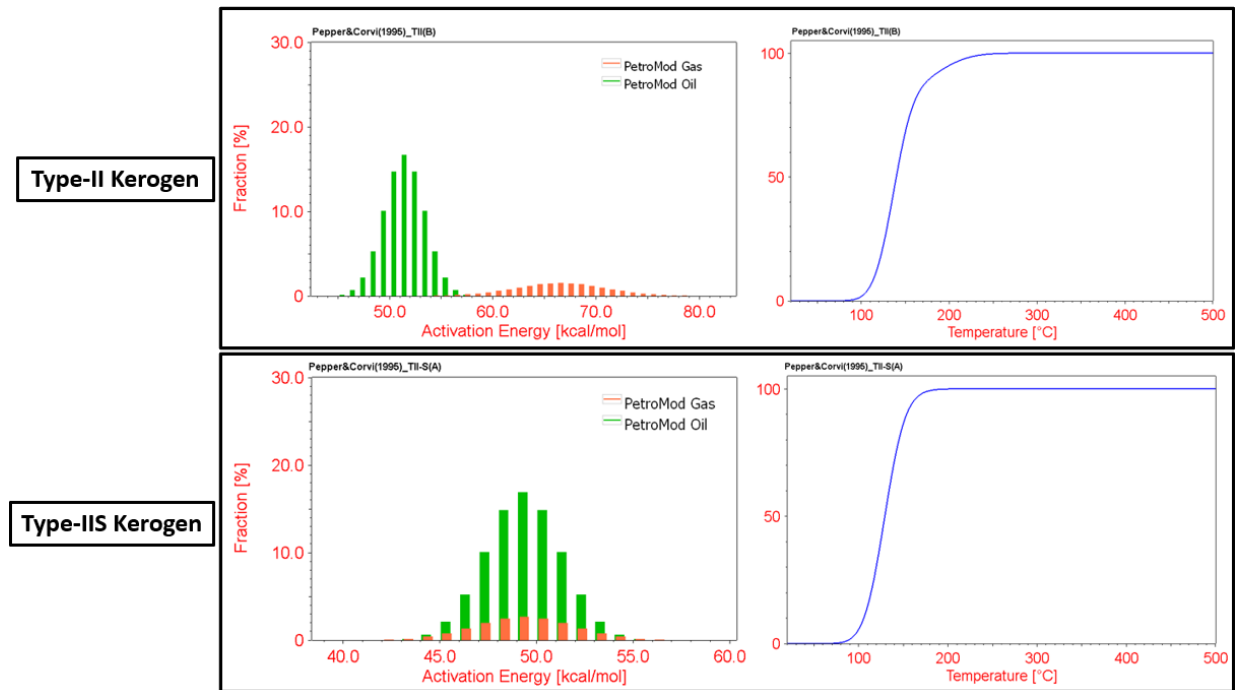

Figure 2.26: **Source rock maturity kinetics information sourced from Pepper & Corvi (1995).**

2.3.5   E1 and E2 - Maturity Model for Maturity

While the Easy%R_0 model is the most commonly used maturity model for %R_0 estimations (A. K. Burnham, 2017), the model has been identified to potentially overestimate maturities in the range of 0.5 - 1.7 %R_0 by up to 0.35 %R_0 compared to measured %R_0 (Schenk, Bird et al., 2017; Nielsen et al., 2017), a feature that is widely referred to as a *dogleg* trend in literature studies. At depths corresponding to higher %R_0 values than the aforementioned range, the Easy%R_0 model often underestimates %R_0 compared to measured values. In the absence of any %R_0 calibration data in the AOI for this study to test whether such errors in the simulated %R_0 values exist, two more maturity models were used to constrain maturity model-related variations in simulated %R_0 values; this was done following the recommendations regarding multiple model usage for thermal calibration by Schenk, Peters & Burnham (2017).

The first model (case E1) proposed by Nielsen et al. (2017), known as the Basin%R_0 maturity model, calculates %R_0 as shown in equation 2.22. Here, %R_{00} refers to the reflectance of immature vitrinite and adopts a constant value of 0.2104 %. The variable F follows the parameterization of the Easy%R_0 model by Sweeney & Burnham (1990) (see subsection 2.4).

$$\%R_0 = \%R_{00}e^{3.7F} \tag{2.22}$$

The second model (case E2) by A. Burnham (2016), known as the Easy%R_0DL (dogleg) model, calculates %R_0 using the same equation as for the Easy%R_0 (equation 2.3), but with different kinetics parameter values. These are shown in figure 13 in the appendix. Figure 2.27 shows the (maximum) temperature dependence of the calculated %R_0 using the Easy%R_0, Basin%R_0, and Easy%R_0DL models. As can be understood from the figure, in the temperature range of $100\text{-}200\,°C$, the Basin%R_0 and Easy%R_0DL models show lower maturities compared to the Easy%R_0, compensating for the aforementioned dogleg feature. The significantly different end %R_0 values for the three models are not very relevant for consideration, since they occur at temperatures higher than $330\,°C$, which are not commonly reached in sedimentary basins with geothermal gradients under normal depositional conditions (Schenk, Peters & Burnham, 2017).
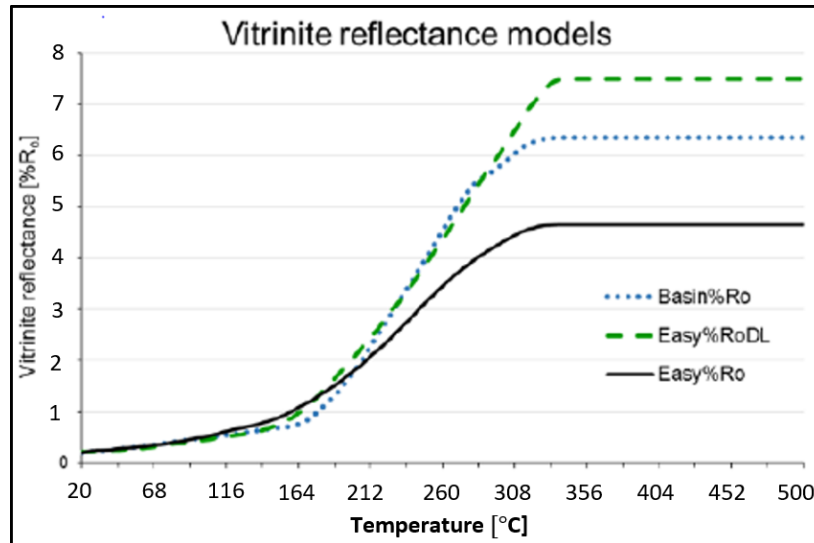

Figure 2.27: **Vitrinite Reflectance (%R_0) as a function of temperature for the Easy%R_0, Basin%R_0, and Easy%R_0DL maturity models.**
Modified from: Schenk, Peters & Burnham (2017).

Chapter 3

Results

The aim of this chapter is to discuss key modelling results regarding the maturity indicators for the J100 source rock. The results for the base case thermal model is the focus of section 3.1, and a comparison of the base case results with the sensitivity analyses modelling results is presented in section 3.2. For both sections, the temporal evolution as well as the present-day values at the C-1 well location as well as the wider AOI are the focus of the associated subsections.

3.1 Base Case Modelling Results

3.1.1 C-1 Well Location

Temporal Evolution - Temperature, $\%R_0$ and TR Figure 3.1 (top and middle sub-figures) shows the burial history of the sedimentary column at the C-1 well location, which has been calculated using the back-stripping approach (subsection 2.2.5) by accounting for the PWD as well as ages and depositional thicknesses of the layers. The temperature distribution and transformation ratio (relevant only for J100 source rock) for all layers through time can be seen overlain with the burial history plots on the top and middle sub-figures, respectively. The bottom sub-figure shows the temperature and transformation ratio evolution through time for the (middle of the) J100 layer.

During the Cretaceous period, a relatively small rate of temperature increase for the J100 can be explained primarily by limited sediment deposition (500 m) on top of the J100, in conjunction with the comparatively higher thermal conductivities of the deposited carbonaceous layers during the Cretaceous (see table 2.4); the latter implies greater heat "extraction" from the J100 sequence, thereby limiting the temperature increase over this period. With the deposition of the primarily siliciclastic Paleocene-Eocene (T20) layer, the rate of temperature rise markedly changes, which can again be attributed to the comparatively lower thermal conductivities of the deposited layers, as well as to deeper burial of the J100 layer due to more sediment deposition compared to the Cretaceous period. During the early Eocene, at approximately 62 °C, the process of catagenesis can be seen to have begun, with the transformation ratio (TR) becoming non-zero; this process is driven by the source rock maturity kinetics assigned (figure 2.13). At around 20 Ma with temperatures reaching approximately 130 °C, a 50 % TR was seen to have been achieved during the deposition of the Lower Miocene (T52) layer. The TR reached its maximum value of approximately 97 % in the present, with temperature values in the J100 reaching a maximum of ca. 183 °C.

The vitrinite reflectance ($\%R_0$) evolution through time of all the sedimentary layers at the C-1 well location can be seen on figure 3.2 (top sub-figure). The $\%R_0$ evolution through time of the J100 source rock layer in particular is shown on the bottom sub-figure in figure 3.2. According to the results, the J100 layer at the well location entered into the early oil window as recently as 39 Ma, as the $\%R_0$ reached a value of 0.55 $\%R_0$; this corresponds to the later deposition stages of the T30 (Eocene) layer. At ca. 25 Ma, coinciding with the late Oligocene and hence the later stages of the T40 layer deposition, a value of 0.70 $\%R_0$ was reached, which corresponds to entry into the main oil window. At ca. 14 Ma, corresponding to the the start of the Middle Miocene, the J100 reached a value of 1.0 $\%R_0$, indicating the start of the late oil generation window. A value of 1.3 $\%R_0$ was reached at ca. 5 Ma, coinciding with the deposition of the T90 sequence; this $\%R_0$ value signalled the start of the wet gas generation stage. Presently, the (middle of) J100 layer has been simulated to have a value of 1.57 $\%R_0$, indicating that the source rock is still within the wet gas generation stage. It is important to note that the correspondence of a generation window to a certain $\%R_0$ value is not fixed; rather it is dependent on the source rock maturity kinetics (see subsection 2.2.2). In PetroMod$^{©}$, the broad relationship between $\%R_0$ and hydrocarbon generation windows for each kerogen type introduced by Pepper & Corvi (1995) is utilized. These windows serve as useful approximations of the type of hydrocarbon generation likely to occur, thereby aiding proceeding analyses.
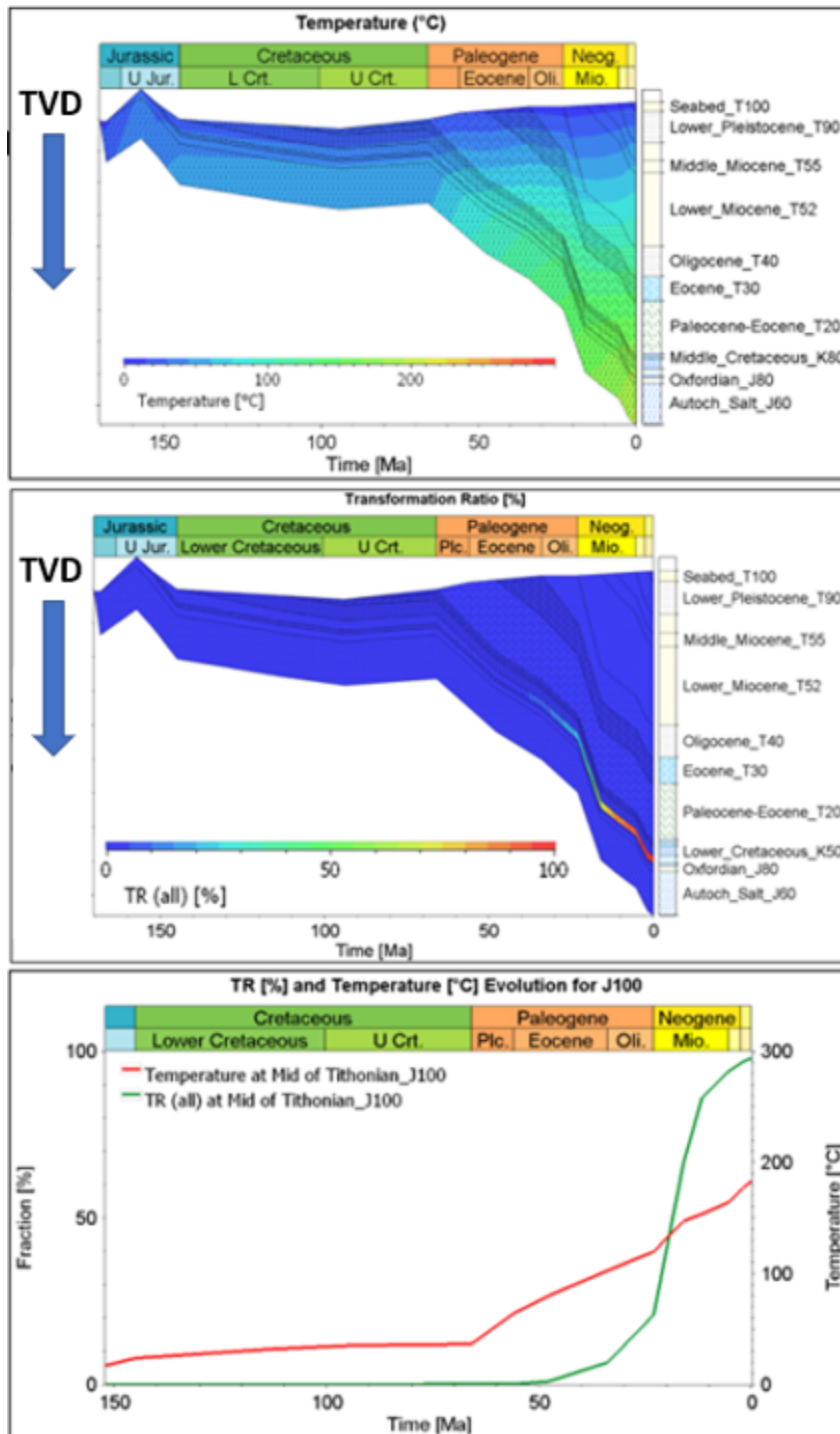
Figure 3.1: Top: **Temperature evolution through time for all layers at the C-1 well location; overlain on the backstripping-deduced burial history plot at the location.** Middle: **Transformation ratios through time for all layers at the C-1 location; overlain on the backstripping-deduced burial history plot at the location.** Bottom: **Temperature and transformation ratio evolution through time for the (middle of) J100 layer at the C-1 well location.**
Note: The true vertical depth (TVD) values have been hidden due to confidentiality requirements of Wintershall Dea GmbH.
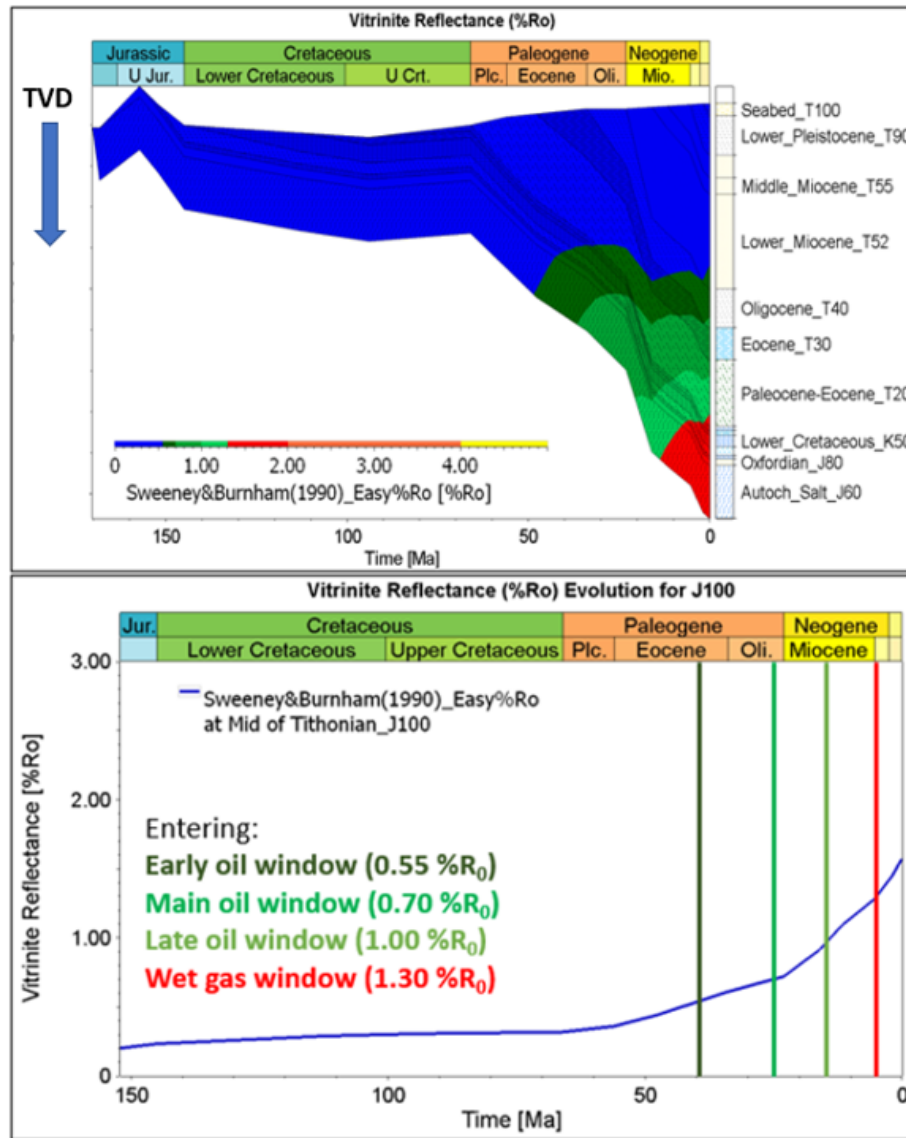
Figure 3.2: Top: **Vitrinite reflectance evolution through time for all layers at the C-1 well location; overlain on the backstripping-deduced burial history plot at the location.** Bottom: **Vitrinite reflectance through time for the (middle of) J100 layer at the C-1 well location.**
Note: The true vertical depth (TVD) values have been hidden due to confidentiality requirements of Wintershall Dea GmbH.

Present Day - Temperature and %R_0   Present-day temperatures as a function of depth at the C-1 well location are shown in the left sub-figure in figure 3.3. A present-day SWIT of 9.7 °C and a basal temperature of approximately 201 °C was simulated at the well location, with a present-day basal heat flow (q) of ca. 41 mW/m^2. A variation of 4 °C was also observed between the top and base of the J100 source rock layer, with temperatures of 181 °C and 185 °C noted for the two horizons, respectively. For all tertiary (T) layers, an average geothermal (vertical) gradient at the well location was calculated to be approximately 21 °C/km (from seabed down to base of T20); a significantly lower average gradient of approximately 12 °C/km was calculated for the Jurassic (J) and Cretaceous (K) layers. This can be explained by the markedly higher thermal conductivities in the Jurassic and Cretaceous layers owing to their predominant carbonaceous lithologies, leading to lower temperature gradient values (Fourier's law, equation 2.13). Conversely, lower thermal conductivities of siliciclastics lithologies in the tertiary layers lead to larger temperature gradient values to fulfill the steady-state precondition of constant heat flow through the sedimentary column at each time step.

The present-day %R_0 as a function of depth at the C-1 well location is shown in the right sub-figure of figure 3.3. The top and base of the J100 source rock layer has been simulated to have maturities of 1.53 %R_0 and 1.62 %R_0, respectively, with the highest simulated maturities at the base of the model (base of J60 layer) showing a maturity of

$2.0\,\%R_0$. It is important to note that while the present-day $\%R_0$ values reveal which generation window the source rock is in, it need not necessarily entail that hydrocarbon generation is actually taking place in the present. This is so because these values are only reflective of the maximum burial/temperature conditions the source rock has been exposed to, and such conditions may have prevailed in the past, causing the current extent of maturation. Such scenarios may emerge if there are structural evolution trends involved in the region of interest such as basin inversion, which may cause widespread and extensive erosion of deposited sediments. Understanding timing of maturation is therefore important, especially within the context of the emergence and occurrence of the various petroleum system elements and processes in the basin in a favorable order such that accumulations within traps actually occur. A discussion regarding this latter point is made in subsection 3.4.2. In the model constructed, since only deposition was accounted for and local erosional events were disregarded (see subsection 2.2.6 for explanation), it can be reasonably understood that the source rock maturities are increasing in the present with generation taking place.
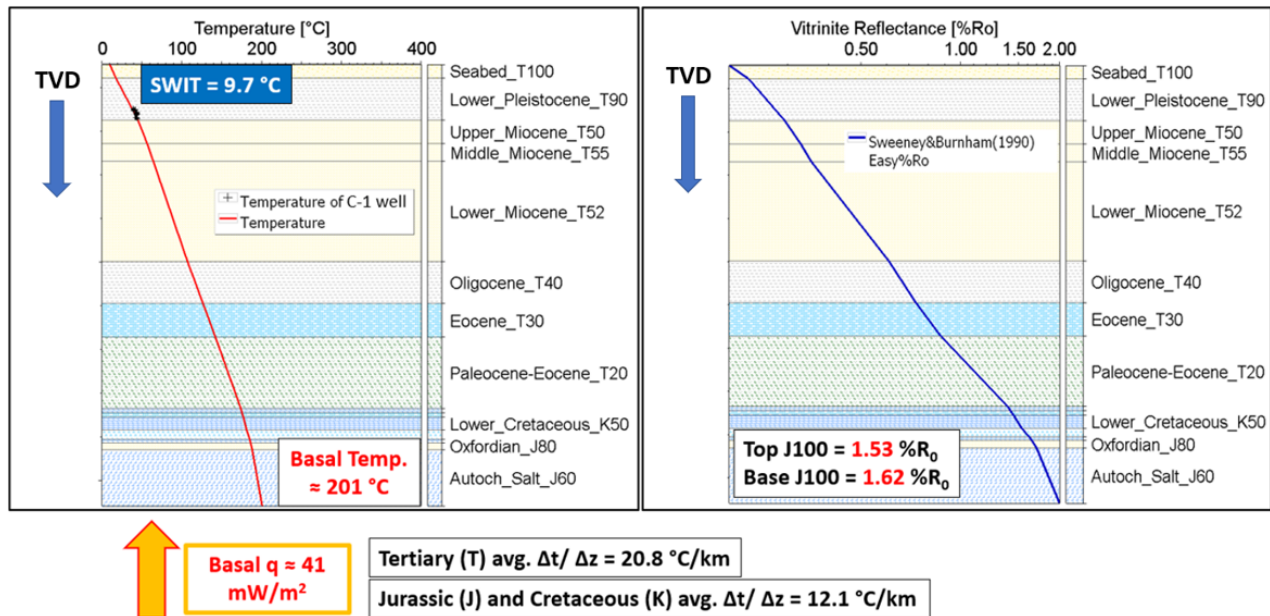

Figure 3.3: **Present-day temperature and vitrinite reflectance as a function of depth at the C-1 well location**.
Note: The true vertical depth (TVD) values have been hidden due to confidentiality requirements of Wintershall Dea GmbH and partners.

3.1.2   Source Rock Maturity Variations − AOI

Temporal Evolution - $\%R_0$ and TR   The temporal evolution of the $\%R_0$ of the top of the J100 source rock across the AOI is shown in figure 3.4, which can be understood to closely approximate the $\%R_0$ at all depths of the layer (see figure 3.3). The source rock remained immature, with $\%R_0$ values remaining under $0.55\,\%R_0$ till 56 Ma (end of Paleocene) during the deposition of the T20 layer. By 47.8 Ma (early Eocene; end of T20 deposition), regions within the AOI had entered the early and main oil windows, though the source rock still predominantly remained immature. This changed by 23.0 Ma (end of Oligocene and T40 deposition), where the source rock resided mainly in the early and main oil windows; some regions within the AOI depicted maturities corresponding to the late oil window, with very small sub-regions even entering the wet gas window. By 11.6 Ma, corresponding with the end of T55 Middle Miocene deposition as well as the conclusion of the Chiapaneco compressional event, some areas of the J100 source rock had notably entered the west gas window, though the major part of the source rock still resided in the main oil window. It is useful to note that some of the portions of the source rock still depicting maturities under $0.55\,\%R_0$ at this time correspond to the interpolated regions during the K100 surface generation, which showcased notably shallower depths. Hence consideration of the maturities in these regions is not of relevance. Further maturation continued towards 5.33 Ma, with source rock regions towards the northeast and southwest of the AOI also entering the wet gas generation window.

The temporal evolution of the TR distribution at the top surface of the J100 across the AOI is also shown in figure 3.4. As expected, the TR is well correlated with the $\%R_0$ evolution, as catagenesis already started in the north of the AOI by 47.8 Ma. With maturation continuing, a majority of the source rock area had passed 80 % kerogen conversion by 5.33 Ma.
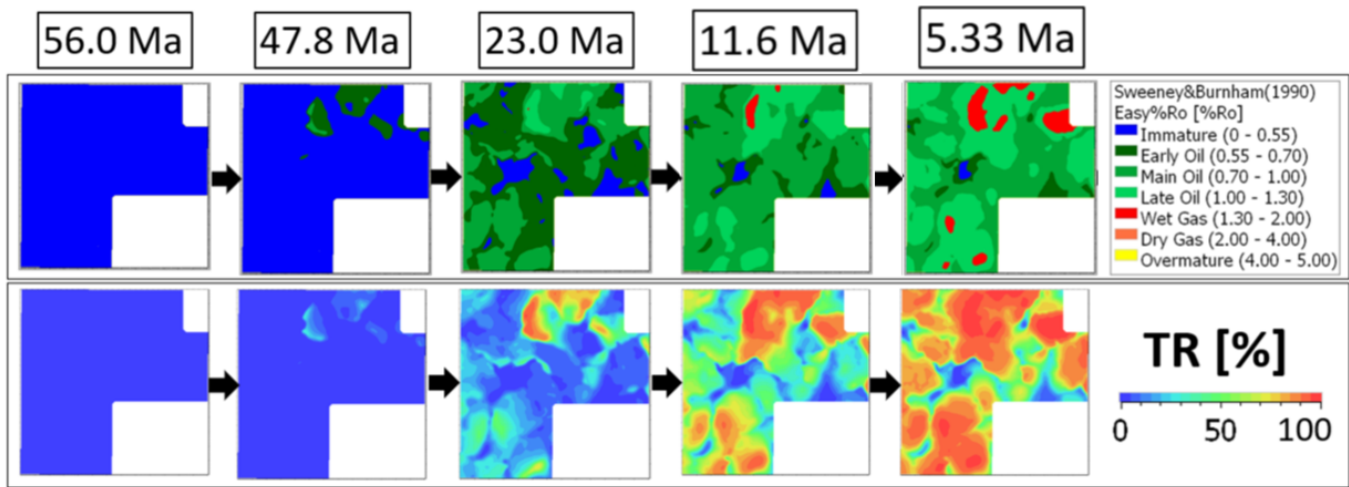
Figure 3.4: **The temporal evolution of the J100 source rock %R_0 and TR across the AOI.**

Present Day - %R_0 and TR   The present-day %R_0 and TR distributions across the AOI for the top of J100 source rock layer are shown in figure 3.5. Since a shifted version of the top of K100 surface was used as a proxy for the top and base of the J100 layer, the interpolated regions from the top of K100 surface (figure 2.9) were eliminated from the J100 surface, since the source rock is likely to not be present in these regions with the protrusions of the allochtonous salt bodies. In the present, the %R_0 distribution indicates a major part of the source rock layer to be within the (early) wet gas window, with an average %R_0 value of 1.31 %R_0 in the AOI (see table 3.1) and with 57.6 % of the %R_0 values in the distribution lying in the wet gas range of 1.3 - 2.0 %R_0 (see histogram in the left sub-figure in figure 3.6). Significant regions were also simulated to be present in the late oil window, with 31.4 % of %R_0 values in the distribution lying within the late oil window of 1.0 - 1.3 %R_0. A maximum and minimum value of 1.81 %R_0 and 0.47 %R_0 was simulated within the AOI.

For the TR, 60 % of the J100 source rock in the AOI was found to have a TR value within the 95 - 100 % range (see right sub-figure in figure 3.6), though the maximum value reached across the AOI was 99 %. A minimum TR value of 2 % was observed for the shallowest buried sub-region in the AOI. Nonetheless, the J100 source rock on average depicted high transformation ratios with a distribution mean value of 91 %.
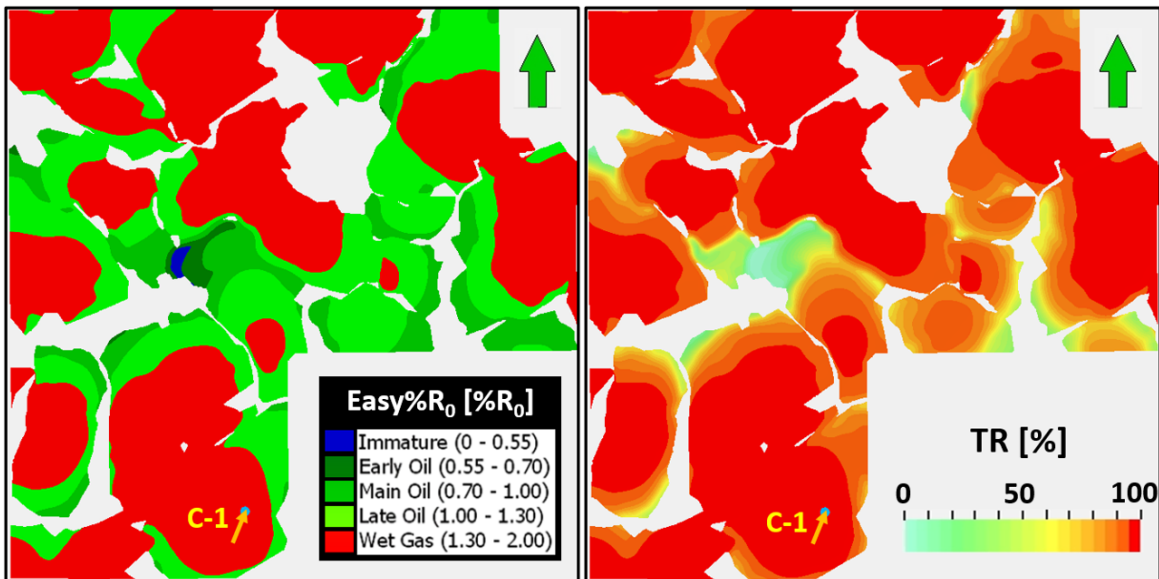

Figure 3.5: **The present-day %R_0 (left) and TR (right) distributions of the J100 source rock across the AOI.**

Note: The interpolated regions for the K100 surface (used for J100 top and base surfaces) were removed for the %R_0 and TR distributions shown.

	Vitrinite Reflectance [%R_0]	Transformation Ratio [%]
Maximum Value	1.84	99.0
Minimum Value	0.47	2.0
Average Value	1.31	91.0

Table 3.1: **Min., max. and average values for %R_0 and TR of (top of) the J100 source rock across the AOI.**
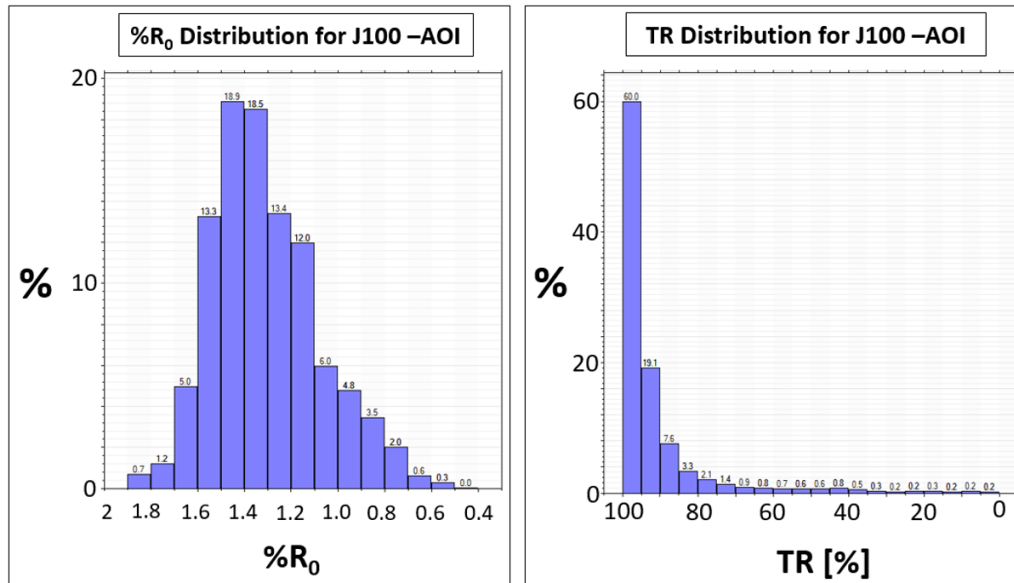

Figure 3.6: **Distribution of %R_0 and TR values of the J100 source rock across the AOI.** See corresponding text for details.

3.2 Sensitivity Analyses Comparisons

3.2.1 C-1 Well Location

Temporal Evolution - Temperature, %R_0 and TR Comparisons regarding the temporal evolution of the temperature at the (middle of) the J100 source rock for the different sensitivity cases with respect to the base case results at the C-1 well location are shown in figure 3.7. Cases D1, D2, E1 and E2 involve testing the impact of source rock maturity kinetics as well as the maturity model assignment on the modelling results, factors that govern (changes in) the simulated maturity values but do not have any direct relationship with temperature or on other parameters feeding into temperature calculations e.g. basal heat flow, thermal conductivities, SWIT etc. Therefore, as expected, the temperature temporal evolution curve for each of the aforementioned cases mimics the base case curve. For case A1, the temperature values at each time step after the source rock deposition (at 145 Ma) are lower relative to the base case values, which follows expectations regarding lower temperatures across the AOI at shallower burial depths (at each time step). It is important to note that at each time step, the differences in geothermal gradients at each location across the AOI as a function of the differences in thermal conductivities of the sedimentary column (due to thicker J80 and J90 sequences relative to the base case) are accounted for in temperature calculations; evidently, such variations do not have a very significant impact on the temperature evolution of the source rock. The temperature evolution for the source rock in case A2 can be explained similarly, as the higher temperature values at each time step after source rock deposition can be attributed to a deeper burial of the source rock. The temperature evolution curve for case B overlaps perfectly with the base case curve till approximately 110 Ma, before deviating negatively and depicting relatively lower temperature values till the present. This can be explained by the interplay between the higher amount of bulk radiogenic heat produced from the relatively thicker crust (larger volume) post-rifting in relation to the decrease in average thermal conductivity of the lithosphere due to a decrease in upper mantle thickness and increase in upper and lower crustal thicknesses in case B (compared to the situation in the base case). Since the upper mantle has significantly higher vertical and horizontal thermal conductivities (see λ_v and λ_h in table 2.6)

CHAPTER 3. RESULTS   51

compared to the upper and lower crust, thinner mantle lithospheric thicknesses and thicker crustal thicknesses lead to lower heat transferred to the sedimentary layers towards the end of the thermal relaxation phase from the LAB; this effect evidently overrides the increase in bulk radiogenic heat produced in the crust, thereby leading to smaller basal heat flow values during this period till the present for case B compared to the base case. It is important to note that it is this very interplay that also leads to higher basal heat flow values in case B compared to the base case syn-rift (compare figures 2.20 and 2.24), during which the LAB is uplifted. However, since the J100 source rock was deposited post-rift, the impact of this higher basal heat flow does not emerge explicitly on the temperature evolution curves in figure 3.7. The temperature evolution curve for case C approximately overlaps with the base case curve till the end of the Cretaceous (66.6 Ma), indicating that the thermal conductivities of the sedimentary column at the time due to layer splitting of the J80, J90, and J100 layers relative to thermal conductivity values with homogeneous mixes (base case) do not show significant enough differences to drive major temperature differences between the cases. However, with the deposition of the T20 layers in case C, an initial negative and then positive deviation relative to the base case curve is observed. This can be physically interpreted as the mean thermal conductivity of the T20 layer with split layers being lower relative to the conductivity value of the T20 layer with homogeneous mixing (base case); this leads to lower heat transfer from the underlying layers, leading to higher temperature values in the source rock layer.
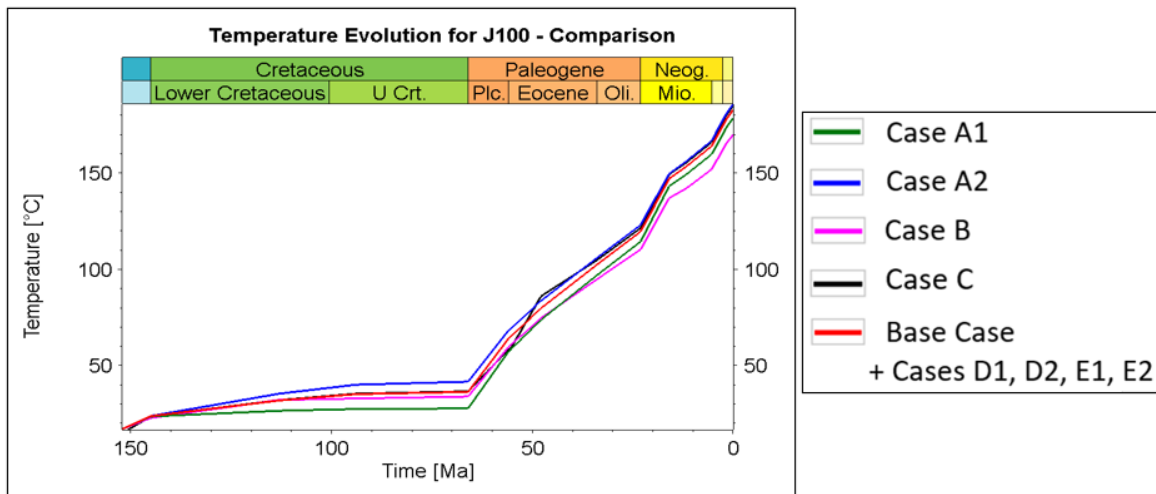

Figure 3.7: **Temperature evolution through time for the middle of J100 source rock for all cases at the C-1 well location.**

The $\%R_0$ evolution of the (middle of) the J100 source rock for the different sensitivity cases with respect to the base case results at the C-1 well location are shown in figure 3.8. Since $\%R_0$ is reflective of the maximum burial temperature for the source rock, the differences in $\%R_0$ values for cases A1, A2, B and C at each time step relative to the base case are simply due to their respective differences in temperature (figure 3.7) relative to the base case at each time step. Cases D1 and D2 mimic the base case curve due to all parameters governing $\%R_0$ calculations in these cases being the same as in the base case. The curve for case E1 is of particular interest, since it shows an approximate overlap with the base case curve till approximately 47 Ma, with the (middle of) J100 reaching approximately 81 °C. Beyond this, the case E1 $\%R_0$ trend shows smaller values relative to the base case, with maximum $\%R_0$ differences relative to the base case occurring at approximately 11 Ma at a temperature of approximately 155 °C. These differences begin to decrease towards the present, with present-day $\%R_0$ values of 1.43 $\%R_0$ and 1.57 $\%R_0$ reached for case E1 and base case, respectively, at a temperature of approximately 183 °C. It is useful to reiterate that the $\%R_0$ for case E1 and the base case are driven by the $\%R_0$ temperature-dependence curves for the Basin$\%R_0$ and Easy$\%R_0$ maturity models (see figure 2.27). Similarly, based on the Easy$\%R_0$DL maturity model for case E2, smaller values for the $\%R_0$ trend relative to the base case occurred already at approximately 145 Ma at a temperature of approximately 25 °C. Maximum differences between the case E2 and base case $\%R_0$ values occurred at approximately 23 Ma at a temperature of 120 °C. At 5 Ma, with a temperature of approximately 130 °C, a crossover of the case E2 and the base case curves was observed. In the present-day, the (middle of) J100 source rock was simulated to have a vitrinite reflectance value of 1.74 $\%R_0$. For each sensitivity case, table 3.2 provides the time at which the source rock at the C-1 well location entered into the various hydrocarbon generation windows. The values have been rounded off to the nearest Ma for all oil windows, and to the nearest 0.5 Ma for the wet gas window; the latter was done to allow for distinction between the cases.

The TR evolution of the (middle of) the J100 source rock for the different sensitivity cases with respect to the base
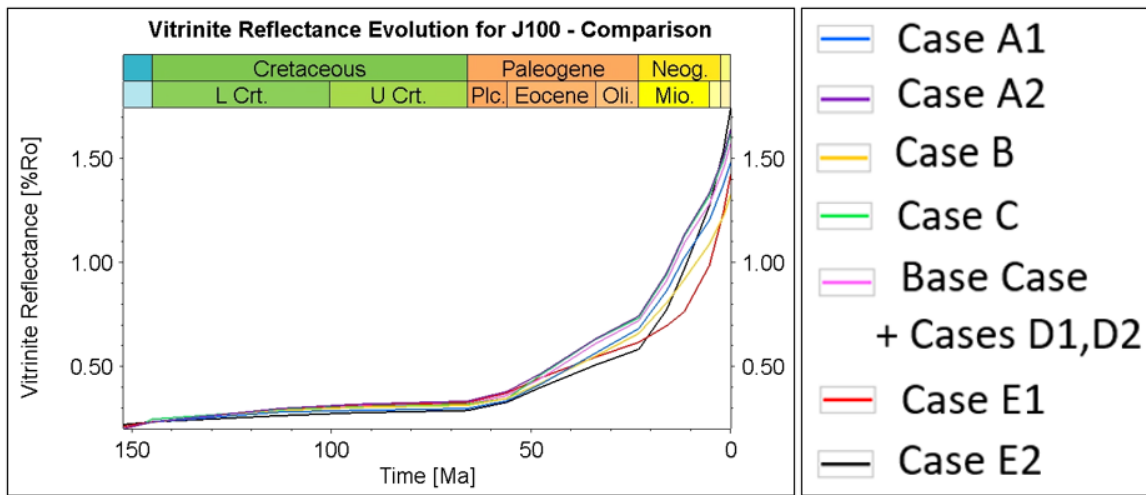
Figure 3.8: **%R$_0$ evolution through time for the middle of J100 source rock for all cases at the C-1 well location.**

	Sensitivity Cases - Hydrocarbon Generation Timing [Ma]						
Window	**A1**	**A2**	**B**	**C**	**E1**	**E2**	**Base Case, D1, D2**
Early Oil	35	41	34	40	33	27	39
Main Oil	22	27	21	25	16	19	25
Late Oil	12	15	9	14	5	11	14
Wet Gas	3	6	0.5	5	1	5	5

Table 3.2: **Comparison - Entrance of the J100 source rock into the various hydrocarbon generation windows for the different cases at the C-1 location.** The windows correspond to %R$_0$ value ranges as shown in figure 3.5, for example. The windows correspond to specific %R$_0$ ranges, shown in figure 3.5. Values in this table have been rounded to the nearest Ma for the oil windows, and to the nearest 0.5 Ma for the wet gas window close to the present.

case results at the C-1 well location are shown in figure 3.9. The cases A1, A2, B, and C all involve the same source rock maturity kinetics from Santamaria Orozco (2000) (figure 2.13) to calculate the TR, with only the differences in temperature governing positive (cases A2 and C) or negative (cases A1 and B) deviations from the base case curve through time. Cases E1 and E2 utilized all the same input values for parameters dictating TR calculations, and therefore their respective curves mimic the base case curve. Of particular interest, firstly, is the case D1 TR evolution curve. Due to peak (oil) generation occurring at relatively lower activation energies and TR being higher for the same temperature values for the Pepper & Corvi (1995) Type-II kerogen kinetics compared to the Type-IIS kinetics from Santamaria Orozco (2000) (compare top sub-figure in figure 2.26 with figure 2.13), higher TR values at earlier times are observed at the C-1 well location for case D1 relative to the base case. However, present-day TR values are higher for the base case curve since the activation energies required for kerogen breakdown for gas generation for case D1 are not fully reached, leading to the maximum TR (present-day) of approximately 93 %. Secondly, the Pepper & Corvi (1995) Type-IIS kinetics dictate kerogen transformation at even lower activation energies and temperatures, with gas and oil generation overlapping in their activation energy dependencies (compare bottom sub-figure in figure 2.26 with figure 2.13). This explains the standout behavior of the case D2 curve with its highest TR values at each time step and its present-day TR values being the highest compared to all other cases (near 100 %).

Present Day - %R$_0$ and TR   The present day %R$_0$ values as a function of depth for the base case as well as the sensitivity cases are shown in figure 3.10. The trends for cases A1 and A2 are shown separately in the figure due to the source rock not set up to be at the same depth intervals as for the other cases. The highest present-day maturities at the top and base of the J100 source rock layer can be seen for case E2, with values of 1.69 %R$_0$ and 1.81 %R$_0$, respectively. The lowest maturities were observed with case B, with top and base values of 1.29 %R$_0$ and 1.36 %R$_0$. The deviations of these values from the base case results are summarized in table 3.3. Note that the minimum Δ%R$_0$ is to be understood as the maximum negative deviation. The present-day TR for the middle of J100 source rock for all cases at C-1 well location is are also provided in table 3.4.
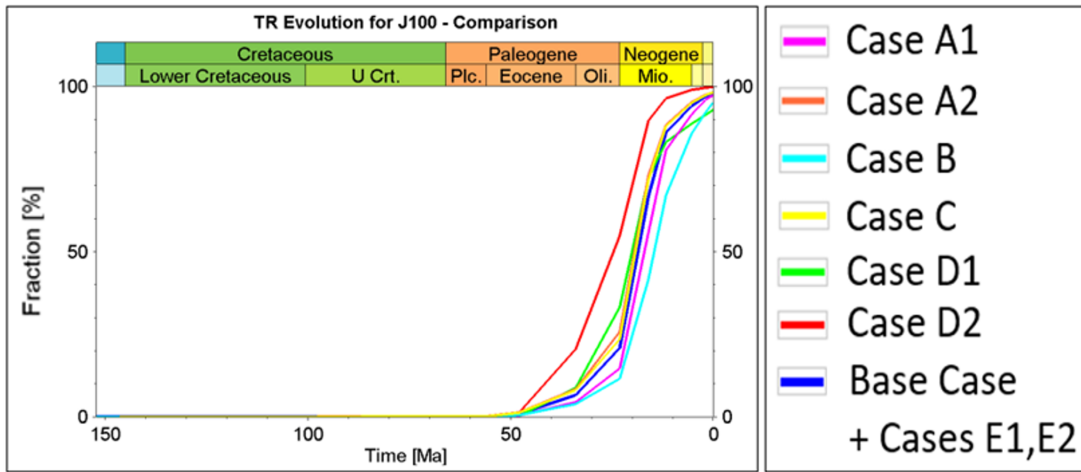
Figure 3.9: **TR evolution through time for the middle of J100 source rock for all cases at the C-1 well location.**
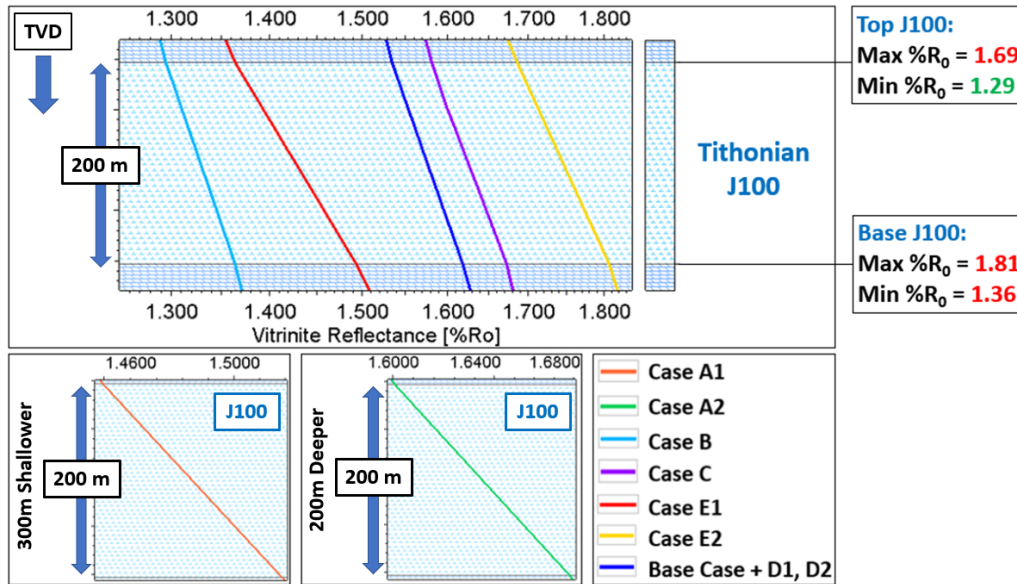

Figure 3.10: **Present-day $\%R_0$ as a function of depth over the J100 source rock at the C-1 well location.** The trends for cases A1 and A2 are shown separately due to the source rock not being located at the same depth intervals as for the other cases.

Note: The true vertical depth (TVD) values have been hidden due to confidentiality requirements of Wintershall Dea GmbH and partners.

	Base Case $\%R_0$	Max. $\Delta\%R_0$	Min. $\Delta\%R_0$
Top J100	1.53	0.16	-0.24
Base J100	1.62	0.19	-0.26

Table 3.3: **Maximum positive and negative $\%R_0$ deviations from the base case $\%R_0$ values at the top and base of the J100 source rock at the C-1 well location in the present day.**

Sensitivity Analyses Cases							
	A1	A2	B	C	D1	D2	Base Case, E1, E2
Present-day TR [%]	97.3	98.2	95.2	98.1	92.9	99.8	97.9

Table 3.4: **Present-day TR for the middle of J100 source rock for all cases at C-1 well location.**

3.2.2   Source Rock Maturity Variations − AOI

It is important to mention at the outset of this subsection that the explanations regarding differences in temporal evolution trends as well as present-day values for the sensitivity cases relative to the base case that have been provided in subsection 3.2.1 hold true for this subsection as well. For this reason, descriptions will mostly be focused on in this subsection, and readers are encouraged to refer to subsection 3.2.1 for explanations to avoid redundancy.

Temporal Evolution - $\%R_0$ and TR   For all sensitivity cases except cases D1 and D2, the temporal evolutions across the AOI of the $\%R_0$ distribution of the (top of) the J100 source rock are shown in figure 3.11 for five time steps. The evolutions for cases D1 and D2 mimic that of the base case and hence are not shown. At 56 Ma, all cases depict immaturity ($\%R_0 < 0.55$) across the AOI. By 47.8 Ma, the northern areas of all cases have entered the oil window; case C involves the largest AOI area to have entered the main oil window compared to the other cases, with case E2 showing the least amount of maturation. By 23 Ma, cases A2, B and C show signs of entrance into the wet gas window in the northern part of the AOI. By this time for case A1, a majority of the source rock across the AOI can be seen to have entered the early and main oil window. For cases E1 and E2, significant areas of the AOI are still simulated to be immature by this time. By 11.6 Ma, all cases prominently depict the existence of wet gas phases, with the exception of case E1, which still showcased a majority of the AOI to be within the early oil window by this time step. By 5.33 Ma, cases A2 and C show the highest maturities on average across the AOI, with significant regions in the north and south of the AOI having been in the wet gas generation phase. Following closely are the case E2 maturities that also show prominent wet gas generation potential towards the south by this time. Case E1 begins to show signs of emergence into the wet gas phase towards the north by this time.

For all sensitivity cases except cases E1 and E2, the temporal evolutions across the AOI of the TR distribution of the (top of) the J100 source rock are shown in figure 3.11 for five time steps. The evolutions for cases E1 and E2 mimic that of the base case and hence are not shown. The TR for all cases become non-zero by 47.8 Ma in the northern portion of the AOI, with case D2 showing the highest transformation across the AOI. TR for case D2 consistently remains higher on average compared to other cases for all time steps, with a majority of the source rock having undergone near 100 % kerogen conversion by 5.33 Ma already. As explained for its TR evolution at the C-1 well location, though case D1 showcases higher TR values on average across the AOI by 23 Ma compared to all other cases except for case D2, by 5.33 Ma it shows lower values across the AOI compared to all other cases except case B; this again can be attributed to the Pepper & Corvi (1995) kinetics for Type-II kerogen dictating kerogen conversion for gas generation at higher activation energies, thereby limiting the TR values. Case B emerges as the standout case with the lowest TR distribution at all time steps, with a significant area of the source rock for this case having remained untransformed (no kerogen conversion) by 23 Ma. A majority of the source rock for this case showcased TR values in the range of 45 - 65 % by 5.33 Ma. This can be attributed to the comparatively lower basal heat flow values post-thermal relaxation (rifting related) for this case, thus yielding lower values in the temperature distributions at the source rock through this time. Cases A2 and C showcase similar evolution trends to one another, which correlates with the similar $\%R_0$ evolution trends for the two cases as well; both of these cases reveal a majority of the source rock in the AOI to have TR values above 85 % by 5.33 Ma.

Present Day - $\%R_0$ and TR   The present-day $\%R_0$ distribution for all sensitivity cases is shown in figure 3.12 (top sub-figure); the maturation trends from figure 3.11 for all cases can be seen to have continued into the present. Generally, while the largest areas of the source rock in the AOI observed to have entered into the wet gas generation phase were for cases A2 and C due to a deeper burial of the source rock (case A2) and lower thermal conductivities of the T20 sequence (case C), the highest maturities at any given localized area over the AOI can be observed for case E2 towards the northeast of the AOI; here, the source rock can be seen to have entered into the dry gas window. This is due to the Easy$\%R_0$DL maturity model used that utilizes a $\%R_0$ temperature-dependence based on which $\%R_0$ values exceed 2.0 $\%R_0$ for temperatures exceeding ca. 190 °C (figure 2.27). For all other cases across the AOI, the dry gas generation window was not simulated to have occurred. The $\%R_0$ distribution for cases E1 and B can be seen to reside within the main and late oil windows for a majority of the AOI area; as explained earlier, this can be attributed to the lower basal heat flow calculated (case B) as well as the different $\%R_0$ temperature dependence based on the Basin$\%R_0$ maturity model used (case E1), respectively.

The bottom sub-figure in figure 3.12 shows the difference between the present-day $\%R_0$ values for the sensitivity cases and the base case $\%R_0$ values at each location across the AOI; from hereon, this difference is referred to as $\Delta\%R_0$. Negative $\Delta\%R_0$ and positive $\Delta\%R_0$ values can be understood as relatively lower or relatively higher maturities, respectively, for the sensitivity cases with reference to the base case values at each location. The $\Delta\%R_0$ distribution for case A1, as expected, reveals negative values in the order of -0.03 to -0.11 $\%R_0$, highlighting the average relative immaturity of the source rock for case A1 compared to the base case. The opposite scenario was observed for case A2, again as expected, with source rock maturities across the AOI on average exceeding the base case maturities by 0.02
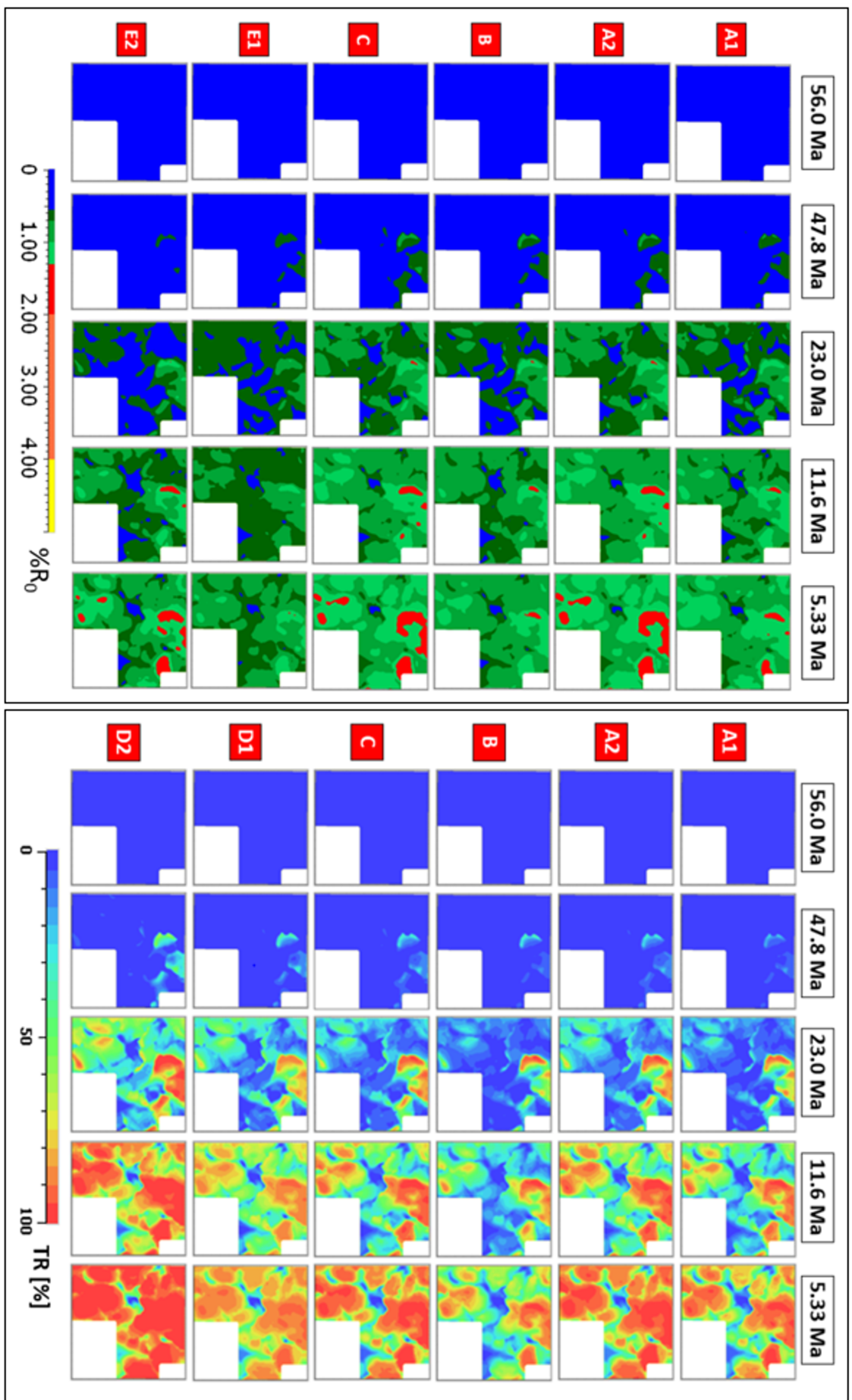
Figure 3.11: Left: **%R₀ evolution through time of the (top of the) J100 source rock across the AOI for all cases except cases D1 and D2.** The evolutions for cases D1 and D2 mimic that of the base case.
Right: **TR evolution through time of the (top of the) J100 source rock across the AOI for all cases except cases E1 and E2.** The evolutions for cases E1 and E2 mimic that of the base case.
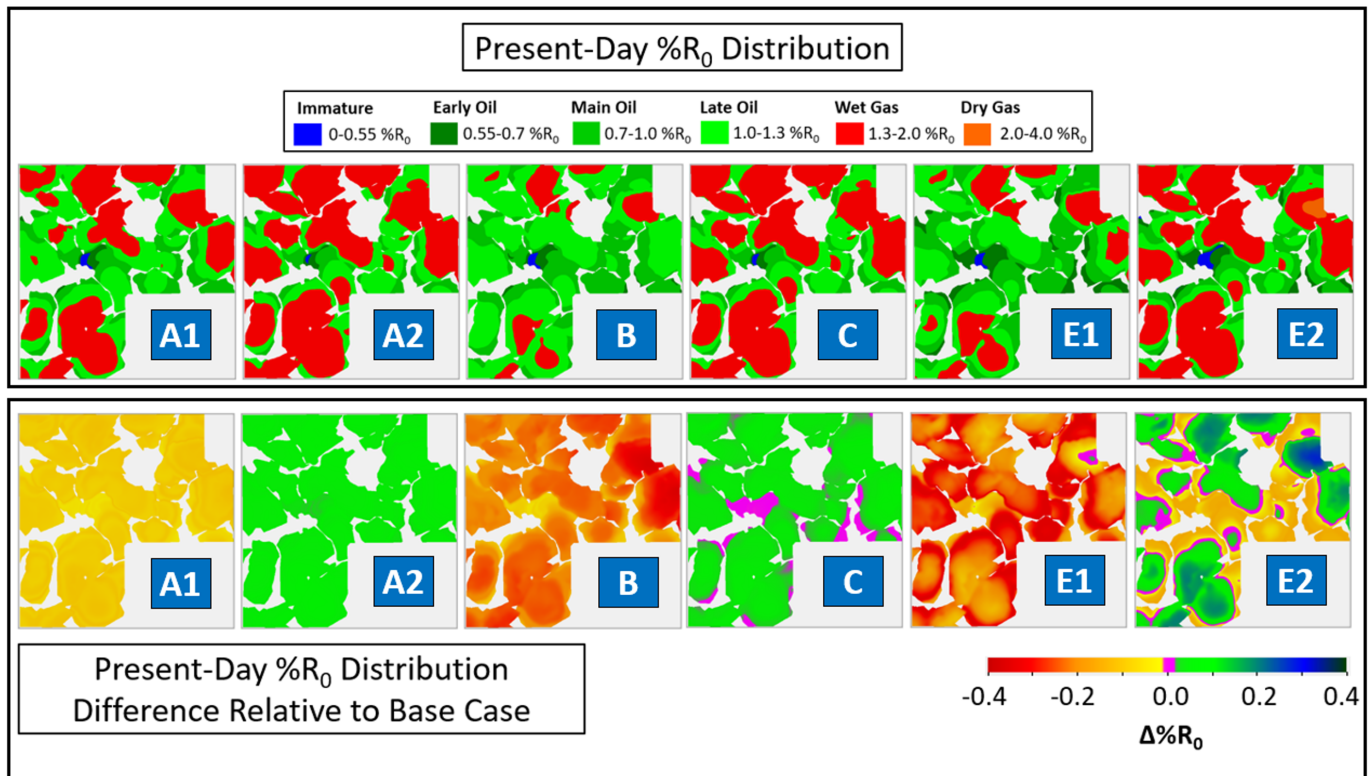
Figure 3.12: Top: **Present-day $\%R_0$ distribution across the (top of) the J100 source rock for all sensitivity cases except cases D1 and D2.** The $\%R_0$ distributions for cases D1 and D2 mimic that of the base case (see figure 3.5).
Bottom: **The difference between the present-day $\%R_0$ distribution for the sensitivity cases (except cases D1 and D2) and the base case $\%R_0$ distribution at each location across the AOI (referred to as $\Delta\%R_0$).**
Note: The interpolated regions for the K100 surface (used for J100 top and base surfaces) were removed for all $\%R_0$ and $\Delta\%R_0$ distributions shown.

Sensitivity Analyses Cases							
	A1	**A2**	**B**	**C**	**E1**	**E2**	**Base Case, D1, D2**
Max. $\%R_0$	1.75	1.95	1.49	1.92	1.86	2.12	1.84
Min. $\%R_0$	0.43	0.50	0.43	0.48	0.46	0.42	0.47
Avg. $\%R_0$	1.23	1.36	1.09	1.36	1.07	1.33	1.31
Max. $\Delta\%R_0$	-0.03	0.08	-0.04	0.11	0.02	0.28	NA
Min. $\Delta\%R_0$	-0.11	0.02	-0.35	-0.01	-0.34	-0.15	NA
Avg. $\Delta\%R_0$	-0.08	0.06	-0.22	0.04	-0.24	0.02	NA

Table 3.5: **Minimum, maximum, and average values for the present-day $\%R_0$ and $\Delta\%R_0$ distributions shown for the (top of the) J100 source rock for all cases in figure 3.12.** NA = Not Applicable.

to $0.08\,\%R_0$. The $\Delta\%R_0$ distribution for case B showed significantly higher (negative) maturity differences, with values reaching $-0.35\,\%R_0$. The comparatively higher thermal conductivities for the T20 layers for case C relative to the thermal conductivity of the homogeneous T20 layer for the base case resulted in $\Delta\%R_0$ values around $1\,\%R_0$. For case E1, while the $\Delta\%R_0$ for the majority of the source rock area is less than zero, a localized area towards the northeast showcased positive values. For case E2, this phenomenon is more widespread, with approximately half of the source rock area showcasing positive $\Delta\%R_0$ while the remaining area showcases negative values. For both these cases, as explained earlier in subsection 3.2.1, the $\Delta\%R_0$ distributions can be explained by the initial negative and then positive deviation of the $\%R_0$ temperature-dependence trends for the Basin$\%R_0$ and Easy$\%R_0$DL maturity models relative to the $\%R_0$ temperature-dependence trend for the Easy$\%R_0$ maturity model used for the base case (see figure 2.27). The key values of the distributions in figure 3.12 are shown in table 3.5. In the table, the negative values for minimum and maximum $\Delta\%R_0$ can be understood as the maximum and minimum negative deviations, respectively.
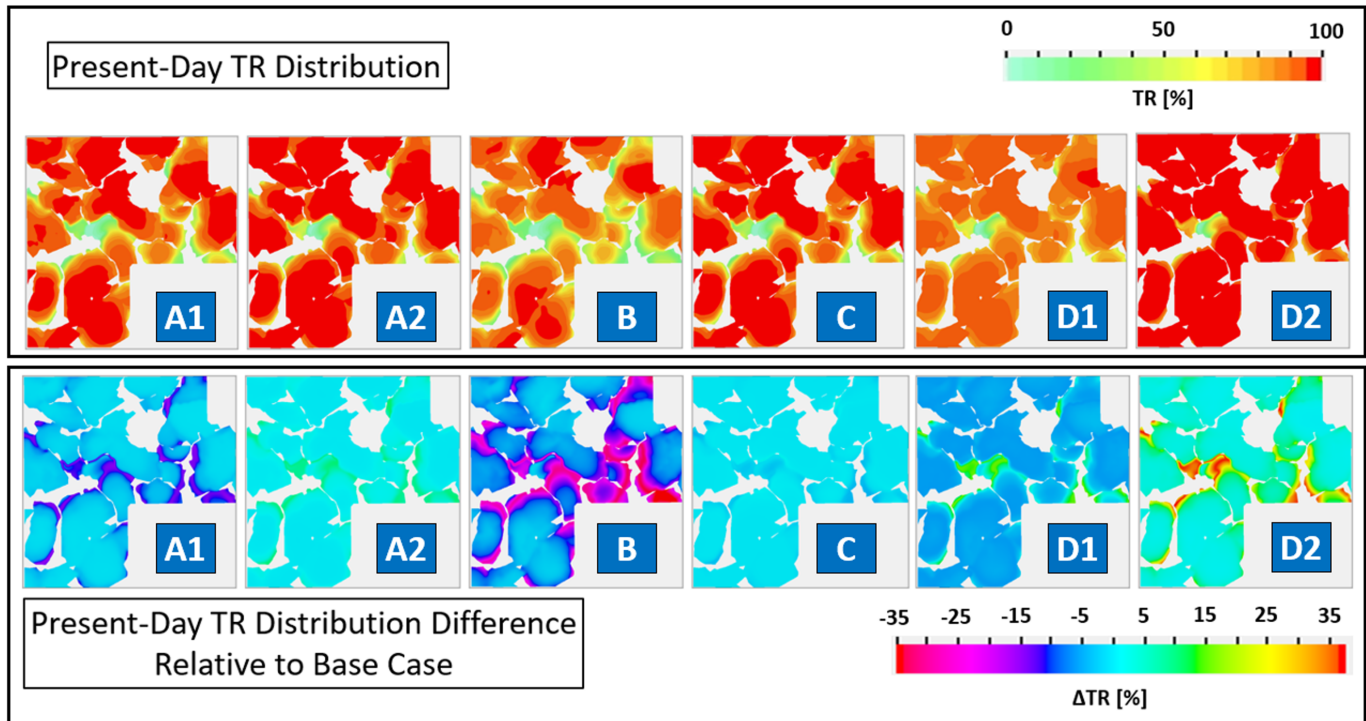
Figure 3.13: Top: **Present-day TR distribution across the (top of) the J100 source rock for all sensitivity cases except cases D1 and D2.** The TR distributions for cases D1 and D2 mimic that of the base case (see figure 3.5).
Bottom: **The difference between the present-day TR distribution for the sensitivity cases (except cases D1 and D2) and the base case TR distribution at each location across the AOI (referred to as ΔTR).** Note: The interpolated regions for the K100 surface (used for J100 top and base surfaces) were removed for all TR and ΔTR distributions shown.

Sensitivity Analyses Cases							
	A1	**A2**	**B**	**C**	**D1**	**D2**	**Base Case, E1, E2**
Max. TR	98.8	99.2	97.7	99.1	95.6	99.9	99.0
Min. TR	1.1	2.7	1.1	1.7	1.1	3.9	2.0
Avg. TR	87.9	92.6	80.8	91.0	87.3	97.2	91.0
Max. ΔTR	-0.3	11.7	-0.9	3.2	15.6	37.8	NA
Min. ΔTR	-16.7	0.1	-36.8	-4.2	-5.9	0.9	NA
Avg. ΔTR	-3.1	1.7	-10.2	0.0	-3.7	6.2	NA

Table 3.6: **Minimum, maximum, and average values for the present-day TR and ΔTR distributions shown for the (top of the) J100 source rock for all cases in figure 3.13.** NA = Not Applicable. All values in this table are percentages (%).

The present-day TR distributions at the (top of the) J100 source rock for all cases except cases E1 and E2 are shown in the top sub-figure of figure 3.13. Additionally, the bottom sub-figure in the figure shows the difference between the present-day TR values for the sensitivity cases and the base case TR values at each location across the AOI; from hereon, this difference is referred to as ΔTR. With an average TR of approximately 97 % across the AOI, case D2 has the highest average ΔTR of approximately 6 % in the area, with ΔTR values reaching as high as 37.8 %. In contrast, case B has the lowest average TR of approximately 81 % across the AOI, with an average ΔTR of -10.2 %; the lowest ΔTR value for this case reached is -36.8 %. Table 3.6 highlights the present-day average, minimum and maximum TR and ΔTR values across the AOI for the two aforementioned cases in addition to cases A1, A2, C and D1; the table values can be understood in conjunction with figure 3.13 for a clear overview of the TR and ΔTR distributions.

3.3   Summary of Results

Owing to the extensive nature of the results, a summary of the key points from the results is deemed useful.

1. Vitrinite Reflectance ($\%R_0$):

   - At the C-1 well location, the $\%R_0$ values from the base case and the OAT sensitivity case results indicate that the J100 source rock is in the wet gas generation window at the location in the present day. The source rock entered the oil window between 41 - 27 Ma (late Eocene-Oligocene), entering the wet gas window between 6 - 0.5 Ma (Late Miocene to Pleistocene).

   - Across the wider AOI, the source rock present-day $\%R_0$ values predominantly indicate the presence of late oil to wet gas generation windows, with most of the source rock across the AOI having emerged into the oil generation window between 23 Ma and 11.6 Ma (Lower to Middle Miocene), all sensitivity cases results considered.

   - With respect to the base case $\%R_0$ output values, largest variations in $\%R_0$ values were observed for sensitivity case B (testing relatively thinner J60 autochtonous salt thickness) and sensitivity cases E1 and E2 (testing Basin$\%R_0$ and Easy$\%R_0$DL maturity models, respectively.)

2. Transformation Ratio (TR):

   - At the C-1 well location, present-day TR values in the approximate range of 95 % to near 100 % based on the base case and the OAT sensitivity cases results indicate that most of the source rock kerogen has already been converted into hydrocarbons by the present. Kerogen conversion at this well location began between approximately 55 - 48 Ma (Early Eocene).

   - Across the wider AOI, the results indicate average present-day TR values in the range of 81 % to 97 %.

   - With respect to the base case TR output values, largest variations in TR values were observed for sensitivity case B (see text above) and sensitivity cases D1 and D2 (testing maturity kinetics for Type-II and Type-IIS kinetics from Pepper & Corvi (1995)).

The summary implicitly assumes that source rock maturation timing (and extent) has been "fully constrained" via the OAT sensitivity analyses. This is of course realistically not the case, and the summary is only presented in this way for simplicity and to provide meaningful takeaways. A further discussion regarding this is provided in subsection 5.1.1.

3.4   Implications of Results

3.4.1   Highest Sensitivities - Implications

For both the $\%R_0$ and TR maturity parameters, significant deviations from the base case values were observed based on the uncertainties in the J60 salt sequence thickness (case B). To limit the uncertainties in the maturity parameter values from this end, it is recommended to revisit the gravity inverse modelling scheme and utilize the available base of J60 surface from seismic interpretation (despite interpolations in some regions indicating lack of seismic constraints) in the geological model (see subsection 1.2.4) instead of using a 1000 m shifted base of upper crust surface (see subsection 2.3.2). With this approach, the introduction of the base of J60 surface in the model would at least be more geologically constrained. The base of J60 surface can then be iteratively updated for its geometry as a part of the gravity inverse modelling scheme to attain a better fit between the calculated free-air gravity anomalies with the measured anomalies. Moreover, to limit uncertainties in the modelled $\%R_0$ values pertaining to the use of a particular maturity model (cases E1 and E2), measured $\%R_0$ data from geochemical analyses of core samples from (ideally) multiple wells across the AOI would be needed, particularly for depths corresponding to temperatures ca. 120 °C or higher (see figure 2.27). A comparison between the simulated $\%R_0$-depth trends using the three maturity models (Easy$\%R_0$, Basin$\%R_0$ and Easy$\%R_0$DL) relative to the measured (true) $\%R_0$ values could be made, which would help determine which of the three maturity models offers the best predictions of the %R0 distributions across the area of interest.
Similarly, to limit uncertainties in the modelled TR values pertaining to the use of source rock maturity kinetics (cases D1 and D2), source rock samples would be needed (ideally) from multiple well locations distributed across the AOI, which can then be geochemically analyzed to derive maturity kinetics specific for the J100 source rock in the AOI.

3.4.2   Petroleum System Elements and Processes Timing – C-1 well location

According to Shann et al. (2020), *"probably the most important aspect of the petroleum system(s) [in the Sureste Basin] to understand is the regional timing of maturity of the Tithonian source rock"*. This is because the maturation/generation and expulsion timing of a source rock needs to play out favorably with regards to the deposition of other petroleum systems elements, such as carrier bed(s), reservoir bed(s) and seal bed(s), as well as the occurrence of petroleum systems processes, such hydrocarbon migration, trap formation, and accumulation (Magoon & Dow, 1994). Using the study results for source rock maturation timing and extent across the AOI and, in particular, at the C-1 well location, a general, qualitative analysis can be done to assess the possibilities of hydrocarbon accumulations given available information regarding timing of other elements and processes from literature.

As a preface to the analysis, some background information is necessary. For the offshore Campeche slope hosting the AOI, Shann et al. (2020) identified eight main reservoir intervals involving the Jurassic (J80‑J90), Upper Jurassic (J100), Cretaceous (K80‑K100), Eocene-Oligocene (T30‑T40), Lower Miocene (T52), Middle Miocene (T55), Upper Miocene (T50) and Pliocene (T90); each of these intervals have *"proven oil in representative oil discoveries across the Sureste Basin"*. The timing of depositions of these intervals is well constrained in terms of geological timescales, as is evident by the naming of these intervals. Additionally, the timing of various seals for these reservoir intervals is also important. Shann et al. (2020) stated that for the Mesozoic reservoir units in the Sureste Basin, the shales within the J100 source rock layer act as an *"excellent seal"*. For the Cretaceous reservoir intervals, the T20 sequence regional shale seal exists (see subsection 1.1.3). For the Cenozoic/Tertiary (T) reservoir intervals, the shaly constituents in the sequences themselves have a proven seal capacity, as is evident by the large Cantarell and Zama fields (Shann et al., 2020) (see Preface I and subsection 1.1 in chapter 1). The main/abundant trap types associated with all eight reservoir intervals are salt-flank related traps as well as structural thrust and folding related traps (though stratigraphic-combination traps with structural elements are also present) (Shann et al., 2020; Shann, 2021). The thrusting and folding-related structural traps formed through multiple deformation events within for the AOI, the first of which was the Laramide-related compressional event (see subsection 1.1.2). According to Shann et al. (2020), this event led to folding and thrusting of the Mesozoic sequences in addition to the syn-depositional Eocene (T30) sequence, thereby leading to *"early [structural] trap formation ... likely to be critical [for capturing] an earlier charge for Tithonian source rocks"*. The Chiapaneco compressional event (Middle Miocene - 13.8 Ma to 11.6 Ma; see subsection 1.1.2) triggered extensive vertical allochtonous salt movement, resulting in trap formation in the Sureste Basin. Structural traps formed for the Oligocene-Lower Miocene pre-kinematic intervals, and onlap traps and salt-flank related traps formed for the syn-kinematic Middle Miocene interval (Shann et al., 2020). Since the vertical salt movement (once triggered by the event) continued till the present, salt-flank and salt drape related traps for the post-kinematic Upper Miocene and Pliocene intervals also formed (indicated by the brown arrow in figure 3.14) (Shann et al., 2020). Using this information, a petroleum system elements and process timing chart for the C-1 well location was created to visualize and compare the timing of events; this is shown in figure 3.14. Based on the sensitivity results, oil generation at the well location and its vicinity areas could have begun between middle-late Eocene to Late Oligocene (see table 3.2). By this time window, the Jurassic and Cretaceous reservoir intervals had already been deposited alongside the respective sealing layers for the intervals, as described earlier. Also, by this time, the Laramide-related trap formation is likely to already have occurred as the Laramide compressional event approached its tail end. Considering these aforementioned factors, and also considering the fact that the Jurassic (J80-J90) and Cretaceous (K80-K100) reservoir intervals lie adjacent to the source rock in depositional sequence, there does exist a possibility of oil accumulations - as suggested by Shann et al. (2020) - in structural traps in the Jurassic and Cretaceous reservoir intervals in the vicinity of the C-1 well location. The trap formation related to the Chiapaneco compressional event occurred well within the oil window timing constrained by the sensitivity cases in this study, suggesting the possibility of oil accumulations from the late oil charge from the J100 source rock in the vicinity of the C-1 well location in the Oligocene-Eocene (T30-T40) interval, Lower Miocene (T52) interval, as well as the Middle Miocene (T55) interval in various structural/salt-flank traps; the likelihood of shale-driven sealing capacity and hence accumulations of oil within the reservoir intervals would be higher with the deeper buried intervals due to more compaction of the shale seal beds. The possibility of the post-kinematic Upper Miocene reservoir interval in the vicinity of the C-1 well location also being charged with oil from the J100 source rock can also not be ruled out based on source rock maturation timing (assuming the availability of traps), since the timing of the late oil window (sensitivity cases considered) still coincides with the deposition of the reservoir deposition, though the overlap occurs on the tail end of the oil window. Lastly, if at all, the Pliocene (T90) would more likely be charged with (wet) gas as opposed to oil, though the possibility of oil charge cannot be ruled out completely if the maturation of the source rock occurred similar to the description from case B (wet gas entry at 0.5 Ma; see table 3.2) or a migration lag is considered (see discussion below). For accumulations in both the Upper Miocene (T55) and Pliocene (T90) intervals, sufficient compaction of the shale beds within the sequences would need to have occur due to sufficient overburden sediment deposition while the reservoir intervals are being charged with oil or gas.

Though already mentioned in section 3.3, it is imperative to reiterate that the analysis above assumes the OAT sensitivity analyses cases to have "fully constrained" the possible variations in the timing of the various hydrocarbon windows, this is realistically not true; this is discussed in section 5.1.1. The discussion also assumes the availability of impediment-free migration pathways from the source rock to the reservoir, with negligible migration lag on geological timescales (i.e. the time it takes for the expelled hydrocarbons to reach a trap); both of these assumptions may not hold true in geologically realistic scenarios and may inhibit or limit accumulations. With regards to the assumption regarding the migration lag, He (2016) suggested that such lags "*in many cases ... [have] been estimated to be between 5 and 20 million years*" and "*may take about 10 % to 20 % of the entire duration of the hydrocarbon generation window*". The discussion also assumes no compromises in seal integrity while also assuming trap retention till the present; again, both these assumptions may not hold true, with the latter being a key risk factor with salt-flank related traps due to continuing vertical migration of some allochtonous salt bodies even in the present (figure 2.2).

While a discussion of the assumptions introduces uncertainties regarding the possibility of oil/gas accumulations, the analysis done is still useful. This is because it suggests that potential hydrocarbon accumulations in the C-1 well vicinity in various traps associated with various reservoir intervals cannot be ruled out based simply on maturity timing considerations. This prompts the need for realistically assessing all aforementioned assumptions in order to place more realistic constraints on the possibility of accumulations; a brief discussion on how this can achieved is provided in section 5.1.
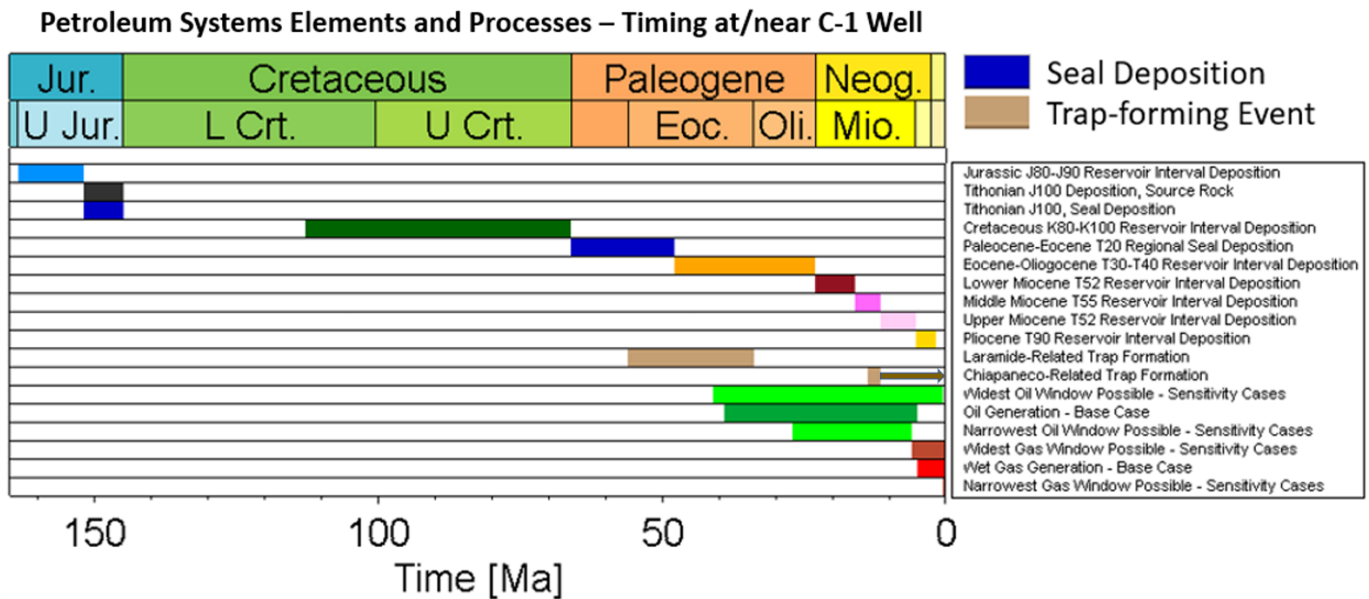

Figure 3.14: **Comparison of the timing of the J100 source rock entering into the oil and gas windows at the C-1 well location relative to the timing of other key petroleum system elements and processes in the vicinity.**

Chapter 4

Discussion

4.1 Literature Comparisons – Base Case

4.1.1 Vitrinite Reflectance (%R_0) Distribution

In the case of availability of core samples from multiple wells across the AOI that have been geochemically analyzed to obtain true %R_0 values, the simulated present-day %R_0 distribution can be compared (and calibrated - see modelling workflow in figure 2.11) to validate the present-day simulation %R_0 results. Since such data was not available, reported maturity distributions for the Tithonian J100 source rock in literature studies had to be relied on to get an indication as to whether the base case model simulation results are in the right order.

Shann et al. (2020) suggested that towards the western parts of the offshore Campeche slope in the Sureste Basin where the Tithonian source rock is buried at depths of 10-12 km and the temperatures exceed 250 °C, present-day dry gas maturity windows exist. This is generally in agreement with the modelling results, since the source rock in the AOI is buried shallower in the present at depth ranges of 7-9 km on average; this results in present-day temperatures generally in the order of 180-200 °C across the source rock in the AOI (see figure 14 in the appendix), and yields maturities in the late oil (1.0-1.3 %R_0) to wet gas windows (1.3-2.0 %R_0). Moreover, Santamaria Orozco (2000) also provided regional-scale average present-day %R_0 values for the source rock for a study area towards the east of the AOI (see figure 4.1). As can be interpreted from the figure, %R_0 values in the order of 1.0-1.3 %R_0 (late oil window) were observed for samples in the depth range of 5-6 km. This again supports the suggestion that simulated maturity distributions for the source rock at the depth ranges in the AOI are in a realistic range.

4.1.2 Present-Day Heat Flow, Geothermal Gradient, and Thermal Conductivities

The basal heat flow distribution for the base case model was calculated in the range of 39-44 mW/m^2 for the present-day (see subsection 2.2.5 and figure 2.20). These values show very good agreement with the range of present-day heat flow values reported by Rosales-Rodriguez et al. (2014), who reported values in the range of 40-45 mW/m^2 where the AOI is located. This is shown in figure 4.2.

Moreover, a general reasonability of the simulated geothermal gradient at the C-1 well location is indicated by the calibration of the present-day simulated temperature-depth trend at the well location with temperature calibration data at the well location (sub-figure A in figure 2.17) as well as by the reasonable fit between the aforementioned simulated temperature-trend with the regional temperature data till a depth of approximately 5.5 km (sub-figure B in figure 2.17). Similarly, at all other locations across the AOI, reasonable fits between the simulated temperature-depth trends and the regional temperature data were also observed, thereby indicating general reasonabilities of the geothermal gradients across the wider AOI. For visual demonstration, such fits are shown at three random locations across the AOI in figure 15 in the appendix.

The reasonabilities of the calculated basal heat flow distribution and geothermal gradients then implicitly point to the general reasonability of the thermal conductivities values assigned to the various layers of the base case model as well (again, see governing relationship based on Fourier's Law, equation 2.13), despite these values being derived solely on the basis of the lithological mixes assigned (see subsection 2.2.2) and not being constrained by any further data. It is important to note that the focus of this discussion is, however, only to make a qualitative assessment of the reasonability of the thermal conductivities assigned; to provide a more quantitative insight into the deviation of the calculated values with respect to the *true* thermal conductivities, more data would indeed be needed. This is discussed in subsection 4.2.2.
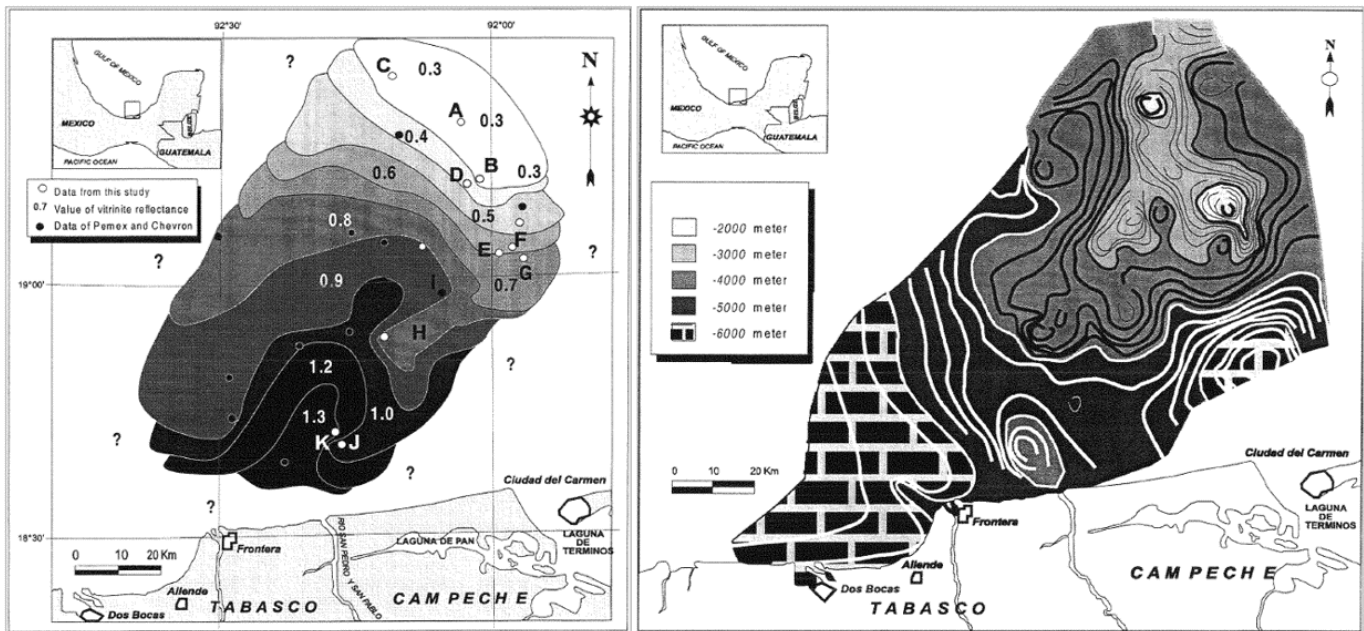
Figure 4.1: **%R₀ values (left) at their corresponding depths (right) for a study area east of this study's AOI.**
Modified from: Santamaria Orozco (2000).
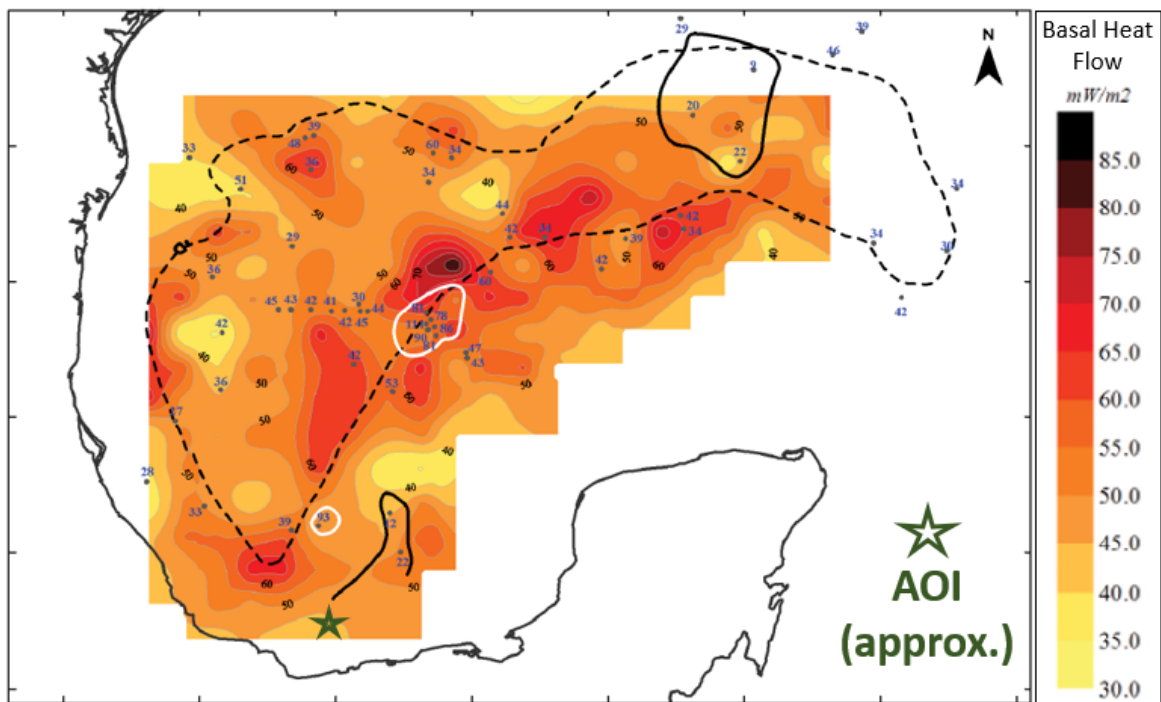
Figure 4.2: **The basal heat flow distribution across the Gulf of Mexico. The location of the AOI has been approximated with a green star symbol**. The coordinates have been hidden for confidentiality reasons.
Modified from: Rosales-Rodriguez et al. (2014).

4.2 Further Uncertainty Sources - Model Inputs

Beyond the uncertainties in the source rock maturities from uncertainties in the inputs addressed in section 2.3, further unquantified sources of uncertainties (in the context of this study) in the source rock maturity results can be identified that pertain to simplifications and assumptions associated with the inputs, as well as to the limited or unavailable well data. These at least warrant a qualitative discussion, which is the main focus of this section.

4.2.1   Seismic Interpretation

Lack of Seismic-Well Ties   To facilitate more accurate horizon identification during seismic interpretation, seismic-well ties at well locations in a region of interest are typically generated as a fundamental step in the interpretation process, since they link subsurface properties measured directly at the well location through various logs to the remotely acquired seismic dataset (Cho & Nordin, 2014). While structural and stratigraphic constraints employed to identify key horizons indeed are necessary even with seismic-well ties available in a region of interest (in particular for a regional-scale study of this type), these constraints alone leave room for uncertainties with regards to the exact feature of a seismic trace picked for a horizon - i.e. peak, trough, z-crossing (peak to trough crossing), or s-crossing (tough to peak crossing) - within a depth range constrained by structural and stratigraphic information. This then introduces uncertainties in interpreted depths, at the very least, based on whether a horizon is interpreted at a peak, an adjacent trough, or any of the z- or s-crossings; such uncertainties are further exacerbated at deeper depths as vertical resolutions decrease. Such uncertainties regarding interpreted depths for this study in some local areas were actually higher since the structural and stratigraphic constraints for the horizons of interest did not allow for limiting the depth ranges within which the horizon(s) could be interpreted to a single set of a peak and its adjacent trough; rather, the depth ranges defined covered multiple adjacent peaks and troughs, and any feature within the ranges which could have been interpreted as the horizon of interest (except for K100 and T30, which needed to be interpreted at peaks; see subsection 2.1.3). A visual example for this is provided in figure 16 in the appendix. This in turn introduces uncertainties in the depositional thicknesses of the layers and burial histories simulated by the thermal model with respect to the geologically *true* scenario, as well as introducing uncertainties in, for example, thermal conductivities with depth at each location across the AOI; the latter in turn impacts other thermal parameters including source rock maturity indicators. Therefore, ideally, the availability of seismic-well ties at multiple well locations and till greater depths across the AOI would add more certainty to structural inputs of similar thermal models for the AOI. In particular, for the horizons that could not be identified based on structural and stratigraphic constraints, availability of seismic-well ties at their corresponding depths would allow their interpretation on the seismic dataset. This would limit the uncertainties in the thermal model structural input otherwise associated with the pseudo-surfaces.

Neglection of Allochtonous Salt   The lack of consideration of allochtonous salt bodies (and their corresponding spatial migration through time) also is a source of uncertainty in the study results based on two factors: 1) a structural and 2) a thermal factor.

1. Since the thermal model for the study is a deposition-only model, the burial histories of the layers in this model locally vary from the geologically true scenario. For instance, in the depositional model, the areas across the AOI where the layers are shallow due to uplift by nearby protruding allochtonous salt bodies in the present-day are considered by the model to have been deposited at even shallower depths in past times. However, in reality, deeper burial of these layers in these local areas is likely true before vertical salt migration and protrusion caused their uplift starting the middle Miocene. Quantifying the impact on source rock maturities from such local discrepancies regarding the burial histories in the modelled versus geologically true case cannot be done with only the information at hand.

2. Salt has a thermal conductivity two to four times greater than that of other sedimentary rocks, with values potentially reaching $5\text{-}6\,\mathrm{W\,m^{-1}K^{-1}}$ (Čermák & Rybach, 1982). Thus, salt bodies in sedimentary settings act as "conduits" for heat transport, generally providing a cooling effect (lower temperature anomalies) in sedimentary layers lying underneath salt bodies while providing a heating effect (higher temperature anomalies) in sedimentary layers overlying the salt bodies (Magri et al., 2008). The magnitude and spatial extents of such anomalies are dependent on the sizes of the salt bodies themselves (Cedeño et al., 2019). Furthermore, in regions where multiple salt bodies exist, as is the case with the AOI, the thermal effects of these bodies are mutually interfering in terms of their impact on temperature distributions on sedimentary layers. According to Yu et al. (1992), in the Gulf of Mexico in the present, *"there could be as much as a 30°C anomaly above [mutually thermally interfering] salt bodies due to the focusing of heat by salt, and as much as 50°C temperature contrast between internal salt positions and sediments external to the salt in the deeper parts of the section"*. Since source rock maturation is heavily temperature-dependent, understanding the timing of salt movement and changes in the shape/size of salt domes over time are very important in order to simulate the correct thermal and maturity history in the vicinity of thermally interfering salt bodies (Magri et al., 2008).

   It is critical to mention that it is this very timing factor of salt movement, based on which Mello et al. (1995) argued that maturation in the Gulf of Mexico is likely relatively less sensitive to the Miocene-Pliocene stage of salt mobilization; this is because the time interval since salt mobilization relative to the total deposited duration of source rock is *"too short"* to significantly stunt maturation via the cooling effect (Mello et al., 1995). What

this entails in quantitative terms for the J100 source rock maturity in the AOI cannot be determined given the limited information at hand.

To quantify the impact of both the structural and thermal factors on source rock maturation, studies focused on accurate seismic interpretation involving detailed salt body delineation as well as palinspatic structural restoration studies would be needed; the results from such studies may then be used as input for further advanced studies discussed in section 5.1.

Neglection of Compressional Events and Vertical Stacking The point regarding a need for palinspatic structural restoration studies also ties into the discussion regarding compressional events and vertical stacking that were unaccounted for in this study due to reasons already highlighted in subsection 2.1.6. Such a lack of consideration leads to local discrepancies between the burial history simulated in the model versus the true burial history of the sedimentary strata in the AOI subsurface. A clear example of such a discrepancy has been provided in subsection 2.1.5 and figure 2.7; here, the T20 layer thickness is in fact neither representative of the actual present-day structural scenario, nor does it lead to reasonable approximations of the true T20 thickness during earlier times in these localized areas during model simulation. Once again, palinspatic structural restoration studies can help in limiting such simplifications by evaluating how the floating block (vertical stacking) evolved through time; how the output of such studies can be used as input in further advanced studies to be done in the area is discussed in section 5.1.

4.2.2   Thermal Modelling

Lack of Well Data Beyond the lack of available data to limit uncertainties from the input maturity models as well as from the input source rock maturity kinetics (see subsection 3.4.1), lack of well data also inhibited constraining the assigned thermal conductivities and radiogenic element concentrations (calculated via lithological mixes; see subsection 2.2.3) by (true) values available for actual subsurface layers.

Since source rock maturity is very sensitive to changes in the thermal conductivity (Elison, 2015), reducing uncertainties in the thermal conductivity values would lead to a reduction in uncertainties in the maturity results. For example, this can be achieved by obtaining core samples and/or drilled cuttings and analyzing them for their thermal conductivities at various temperatures through laboratory experiments (for example, see Mottaghy et al. (2011)). The resulting temperature-dependent thermal conductivity values could be used to calibrate (via adjustment of lithological mixing) or override the calculated thermal conductivities in the model. In case of unavailable core samples or cuttings, predictive models for computing thermal conductivities using various logs (e.g. gamma ray logs, neutron porosity logs, and sonic logs) can be employed (Hartmann et al., 2005), assuming such log data is available; such models can be considered fairly reliable since they have been tested to yield thermal conductivity values with an accuracy of $\pm 0.3 \, \mathrm{W \, m^{-1} K^{-1}}$ (Hartmann et al., 2005). These models do not, however, allow for a determination of the temperature-dependence of the predicted thermal conductivities.

The values assigned to the various layers in the thermal model for the concentrations of the radiogenic elements (U, Th, and K) were also not constrained by any field data. According to McKenna & Sharp (1998), radiogenic heat production within the sedimentary section of Gulf of Mexico basin is a significant source of heat, and *"may contribute up to 26 % of the overall surface heat-flow density for an area in south Texas"*. If such a similar radiogenic heat contribution is true for the southern Gulf of Mexico as well, then a significant influence on temperature distributions and hence source rock maturity from radiogenic heat can be inferred. This points to the need for constraining the radiogenic element concentrations assigned to the thermal model in this study in order to limit uncertainties in source rock maturities simulated. To this end, (spectral) gamma ray logs at well locations would prove to be useful since they provide continuous logs of the element concentrations (for example, see Drake et al. (2018)).

Neglection of the J50 Layer As stated in subsection 2.2.2, the J50 layer was accounted for in the model since the base of the layer was neither available from prior interpretive work in the AOI (see section 1.2), nor could it be mapped on the seismic dataset for this study due to poor imaging quality at depths that would likely correspond with this sedimentary sequence. Hence, the top of the upper crust was assumed at the base of the J60 autochtonous salt sequence. If it is assumed that the base of J60 horizon is in fact the base of the J50 horizon i.e. the J60 layer in the model in this study in fact represents the thicknesses of the J50 and J60 sequences combined, then the simulated maturity results can be expected to be (slightly) overestimated, the extent to which cannot be commented on with the information at hand. This is because the sand-prone red beds (see subsection 1.1.3) of the J50 sequence would have thermal conductivities lower than the overlying salt, thereby leading to lower temperature distributions in the shallower sequences. However, if the J50 sequence actually exists at depth intervals at which the shallowest regions of the upper crust is assumed to exist in this model, then the present-day crust would in fact be thinner than considered for the base case model (or sensitivity case B model, for that matter). Such a scenario, assuming the thickness distribution of

the J50 layer is known, would require a revision of the crustal modelling workflow adopted for this study (subsection 2.2.5) for the re-determination of the basal heat flow lower thermal boundary condition.

Paleo-Water Depth (PWD) Trend   Uniform PWD values across the AOI were assigned to all paleo-times except for the present-day (see table 2.5). With the exception of the Cretaceous period, the aforementioned uniform values were based on qualitative descriptions regarding paleo-depositional environments (see subsection 2.2.4). However, 1) these uniform values assigned could potentially lie outside of the range of true PWD values across the AOI at paleo-times, and 2) assuming that the uniform values do indeed fall within the aforementioned range, the true PWD distributions at different paleo-times might depict a large variation in values across the AOI; this means that uniform values may deviate from these true values at various locations by a few hundred meters and hence may not provide reasonable approximations. To provide some context for the latter point, the PWD in the present-day (equal to the depth of the top of T100 surface) ranges from ca. 980 m to 450 m (see figure 1.8 for indication); for example, had a uniform value of 715 m (average of 980 m and 450 m) been assigned for the present-day PWD across the AOI, a discrepancy of 265 m from the aforementioned extreme-end values would be observed at their corresponding locations. Such a discussion regarding the uncertainty in the PWD value assignment is critical since it directly impacts the sediment-water interface temperature (SWIT) calculated, which serves as the upper thermal boundary condition (see subsection 2.2.4). To compensate, PWD depths can be estimated from biostratigraphic analyses focused on fossil content evaluation (Lucas, 2021); to enable such analyses across the AOI, core samples would be required at multiple well locations for sedimentary strata from different geological ages.

4.2.3   Crustal Modelling

For the crustal model evolution, the mantle lithospheric thickness for time steps from and including 93.9 Ma to the present-day was overridden with the known present day mantle lithospheric thickness (see subsection 2.2.5). This implied relatively slow thickening of the mantle lithosphere until 100 Ma, after which a sharp increase in thickness till 93.9 Ma occurred (end thermal relaxation; see figure 2.19). Such a thickening trend deviates from the known phenomenon of post-rifting exponential decay in the thermal anomaly (Cacace et al., 2008), which implies faster rates of mantle lithospheric thickening immediately after the rifting event compared to later. Since rifting was set up to end at 163 Ma, the aforementioned deviation/discrepancy suggests that the J100 source rock (deposited from 152.1 Ma to 145 Ma; see table 2.2) was exposed to higher LAB-uplift related thermal anomaly, and hence relatively higher temperature conditions during the initial and middle periods of the thermal relaxation stage than would have been the case had a geologically more reasonable LAB re-equilibration been simulated. While the effect of this on the source rock maturity cannot be quantified with the information at hand, it can be argued from a qualitative standpoint that this effect would be relatively minimal. This is so because source rock maturation is directly dependent on its burial depth and the thickness of the overlying sedimentary packages since deeper burial leads to higher temperature exposure. By 93.9 Ma, only 400 m of the Cretaceous package would overlie the J100 source rock (tables 2.2 and 2.1), and therefore most of the maturation would occur with the deposition of the thicker tertiary sequences after 66.6 Ma, which is past the thermal relaxation phase. This claim is corroborated by the J100 source rock %R_0 trend in figure 3.2.

It is critical to mention that the inability of the McKenzie model to yield mantle lithospheric thicknesses at the end of the defined thermal relaxation period in the order of the known present-day thicknesses was an unexpected result, since it was expected that the model would yield post-thermal relaxation LAB depth that was equal to the pre-rift LAB depth (i.e. 175 km) (McKenzie, 1978; Cacace et al., 2008). An explanation for such an observation is not straightforward, and would require further investigation.

4.3   Crustal Modelling - Suitability of McKenzie Model

According to J. Pindell et al. (2003) and Hudec et al. (2013), the Gulf of Mexico underwent asymmetric stretching during the Pangaean breakup rifting event. Simple shear models developed to explain such asymmetric rifting, such as the qualitative Wernicke (1985) or the quantitative Issler et al. (1989), suggest that the fundamental difference between asymmetric and symmetric rifting is that the former involves a lateral displacement between regions of maximally thinned crust and regions of maximally thinned mantle lithosphere. In contrast, pure shear models developed to explain symmetric rifting, such as the McKenzie (1978) model, involve an overlap of the crustal and mantle lithospheric regions with maximal thinning during stretching. Indeed, the reconstructed thermal histories on a regional tectonic scale would vary significantly depending on whether symmetric or asymmetric rifting models are considered. However, for the significantly smaller AOI whose spatial scale can be understood as a "point" in relation to the tectonic scale, the use of the *non-uniform* (finite duration and depth-independent) implementation of the McKenzie (1978) model

(see subsection 2.2.5) suffices. This is because for a lithospheric evolution model of such a small spatial scale, the main relevant factor to consider is that the stretching or thinning factors for both the crust and mantle lithosphere represent asymmetric stretching i.e. they are different. While the original uniform McKenzie (1978) would not allow this, the non-uniform implementation of the model does. Therefore, the McKenzie model implementation as such was considered fit for purpose.

Chapter 5

Conclusions and Outlook

The aim of this study was to utilize a thermal modelling workflow to acquire initial estimates for the maturity parameters Vitrinite Reflectance ($\%R_0$) and Transformation Ratio (TR). The study was focused on estimating these parameters for the J100 Tithonian source rock for an area of interest (AOI) in the frontier exploration region of offshore Sureste Basin in the southern Gulf of Mexico. Particular focus was placed on maturity indicator values in the present-day and through (geological) time at the C-1 well location as well as at the wider AOI. *One-at-a-time* sensitivity analyses were also undertaken to assess the variability in output maturity values based on the varying individual input parameter values in isolation. This was done to identify which of these key parameters yielded the greatest variability in the simulated source rock maturity values.

At the C-1 well location, the $\%R_0$ values from the base case and the OAT sensitivity cases results indicate that the J100 source rock is in the wet gas generation window at the location in the present day. The source rock entered the oil window between 41 - 27 Ma (late Eocene-Oligocene), entering the wet gas window between 6 - 0.5 Ma (Late Miocene to Pleistocene). Across the wider AOI, the source rock present-day $\%R_0$ values predominantly indicate the presence of late oil to wet gas generation windows, with most of the source rock across the AOI having emerged into the oil generation window between 23 Ma and 11.6 Ma (Lower to Middle Miocene), all sensitivity cases results considered. With respect to the base case $\%R_0$ output values, largest variations were observed for sensitivity case B (testing relatively thinner J60 autochtonous salt thickness) and sensitivity cases E1 and E2 (testing Basin$\%R_0$ and Easy$\%R_0$DL maturity models, respectively.)

At the C-1 well location, present-day TR values in the approximate range of 95 % to near 100 % based on the base case and the OAT sensitivity cases results indicate that most of the source rock kerogen has already been converted into hydrocarbons by the present. Kerogen conversion at this location began between approximately 55 - 48 Ma (Early Eocene). Across the wider AOI, the results indicate average present-day TR values in the range of 81 % to 97 %. With respect to the base case TR output values, largest variations were observed for sensitivity case B (see above paragraph) and sensitivity cases D1 and D2 (testing maturity kinetics for Type-II and Type-IIS kinetics from Pepper & Corvi (1995)).

The timing of maturation of the J100 source rock at the C-1 well location - assumed to have been constrained by the OAT sensitivity analyses results for simplicity - in relation to the timing of other petroleum system elements and processes in the well vicinity, indicates that hydrocarbon accumulations in the eight reservoir intervals from the source rock are *possible* i.e. presence of hydrocarbon accumulations cannot be ruled out based purely on maturation timing considerations. For further constraints on the possibility of such accumulations, further advanced studies are needed (see section 5.1).

5.1   Gateways for Further Work

5.1.1   Global Sensitivity Analyses and Uncertainty Quantification

The *one-at-a-time* (OAT) sensitivity analyses approach as undertaken in this study is to be understood as a deterministic scenario assessment approach. Such an approach, as already stated in section 2.3, firstly involved disregarding the interdependence of the assorted parameters when assessing the impact of varying the values of the individual parameters in isolation on the maturity results. Secondly, not all inputs that had associated uncertainties were tested using this approach, since the uncertainties in many of these inputs were not easily quantifiable (see section 4.2). Therefore, the range of source rock maturity values obtained as a result of the base case model and the sensitivity analyses does *not* represent the full range of all source rock maturity values that are possible given the uncertainty in the input parameters' values, even though the discussion earlier in this chapter (see text above) and in subsection

3.4.2 assume this for simplicity purposes. Moreover, the OAT approach also does not enable any assessment of the likelihood of the various maturity values simulated.

To address the two aforementioned limitations in further work, *uncertainty quantification* can be conducted through a probabilistic approach by using, for instance, Monte Carlo simulations (Al-Hajeri et al., 2009). Such simulations involve assignment of not a deterministic value to input parameters, but rather a suitable probability distribution (Dumont, 2015). Instead of yielding unique answers, such simulations provide a range of possible output parameter values with their corresponding likelihoods (probabilities) (Al-Hajeri et al., 2009). Such simulations can then be used to define confidence intervals e.g. range of output values above a defined probability threshold. Elison (2015) serves as a useful example study to understand how such an approach can be utilized; in the study, the effect of uncertainty in thermal conductivity on simulated source rock maturity and hydrocarbon generation was assessed. While such an approach can in theory be extended to account for uncertainties in multiple input parameters, computational expenses may become too high. To this end, global sensitivity analyses can be conducted as a pre-step to determine the most influential model input parameters (Degen et al., 2020); once identified, uncertainty quantification can then be proceeded with by considering these parameters.

5.1.2 Palinspatic Reconstruction and Multi-z Modelling

Palinspatic reconstruction studies can be conducted to understand the timing of various compression-related events relevant for the AOI that could not be accounted for in the modelling workflow in this study. Specifically, understanding how/when various reverse/thrust faulting events occurred - particularly, faulting events leading to floating block formation and vertical stacking - would be of interest. Moreover, palinspatic reconstruction studies to account for the timing as well as spatial position and sizes of various allochtonous salt bodies could also be conducted. Such studies, as mentioned in subsection 4.2.1, would require detailed salt body delineation via seismic interpretation in the present-day.

The results from such palinspatic reconstruction studies can then be used as input into a multi-z model, which would allow for the consideration of the above-described complex structural evolution through time. A multi-z basin and petroleum system modelling study can then be conducted, which would enable the consideration of the structural and thermal effects of allochtonous salt bodies (see subsection 4.2.2) as well as the structural effect of local vertical stacking on the J100 source rock maturities. Such studies would also enable further analyses in the AOI, such as:

1. The assessment of the total hydrocarbon generation potential of the J100 source rock in the AOI, assuming seismically mapped surfaces for the source rock are available. This was not possible with the model in this study since the total source rock volume over which such a generation potential would have been calculated was not seismically constrained i.e. it was a pseudo layer. Additionally, the pseudo layer itself was continuous (due to interpolations) and did not account for gaps in the source rock spatial extent due to protruding allochtonous salt bodies.

2. Further constraining the possibility of hydrocarbon accumulation and retention beyond analyses based only on maturation timing (subsection 3.4.2) by actually simulating the emergence of petroleum system elements and the occurrence of petroleum system process across the AOI (particularly, the formation of compression-related structural traps and salt-related traps).

References

Alegret, L. & Thomas, E. (2005). Cretaceous/paleogene boundary bathyal paleo-environments in the central north pacific (dsdp site 465), the northwestern atlantic (odp site 1049), the gulf of mexico and the tethys: The benthic foraminiferal record. *Palaeogeography, Palaeoclimatology, Palaeoecology*, *224*(1-3), 53–82.

Al-Hajeri, M. M., Al Saeed, M., Derks, J., Fuchs, T., Hantschel, T., Kauerauf, A., . . . others (2009). Basin and petroleum system modeling. *Oilfield Review*, *21*(2), 14–29.

Allen, P. A. & Allen, J. R. (2013). *Basin analysis: Principles and application to petroleum play assessment*. John Wiley & Sons.

Ambrose, W., Wawrzyniec, T., Fouad, K., Talukdar, S., Jones, R., Jennette, D., . . . others (2003). Geologic framework of upper miocene and pliocene gas plays of the macuspana basin, southeastern mexico. *AAPG bulletin*, *87*(9), 1411–1435.

Angeles-Aquino, F. & Cantu-Chapa, A. (2001). Aapg memoir 75, chapter 14: Subsurface upper jurassic stratigraphy in the campeche shelf, gulf of mexico.

Aquino-López, J. A. (2004). *Sureste basin, méxico and associated sub-basins: An update and future potential*. Retrieved 2021-06-07, from `https://www.searchanddiscovery.com/documents/abstracts/2004intl_cancun/extended/A91517.pdf`

Arendt, W. & Warma, M. (2003). Dirichlet and neumann boundary conditions: What is in between? In *Nonlinear evolution equations and related topics* (pp. 119–135). Springer.

Arzate, S. O., Soriano, E., Romero, C., Rosales, J., Bahena, E., Hernandez, S. & Cárdenas, A. (2009). Two-dimensional and three-dimensional numerical simulation of petroleum systems approaching the deep-water gulf of mexico (kayab area, campeche sound, mexico): Definition of thermally mature and prospective areas.

Athy, L. F. (1930). Density, porosity, and compaction of sedimentary rocks. *Aapg Bulletin*, *14*(1), 1–24.

Baur, F. U. M. & Littke, R. (2010). *Quantification of heat and fluid flow through time by 3d modeling: an example from the jeanne d'arc basin, offshore eastern canada* (Tech. Rep.). Fachgruppe für Geowissenschaften und Geographie.

Beardsmore, G. R., Cull, J. P., Cull, J. P. et al. (2001). *Crustal heat flow: a guide to measurement and modelling*. Cambridge University Press.

Benson, G. S. (2015). Estimation of arithmetic permeability from a semi-log poro/log10perm regression. In *Aapg annual convention and exhibition*.

Bird, D. E., Burke, K., Hall, S. A. & Casey, J. F. (2005). Gulf of mexico tectonic history: Hotspot tracks, crustal boundaries, and early salt distribution. *AAPG bulletin*, *89*(3), 311–328.

Bird, P. (1998). Kinematic history of the laramide orogeny in latitudes 35–49 n, western united states. *Tectonics*, *17*(5), 780–801.

Brown, A. (2019). Pspetroleum expulsion and formation of porosity in kerogen. *Organic geochemistry*, *22*(1), 39–50.

Brown, D. (2018). *Mexico's sureste basin: An archetype of a 'super basin'*. Retrieved 2021-06-03, from `https://explorer.aapg.org/story/articleid/44481/mexicos-sureste-basin`

Buffler, R. T. & Sawyer, D. S. (1985). Distribution of crust and early history, gulf of mexico basin.

Burnham, A. (2016). *Evolution of vitrinite reflectance models.* Retrieved 2021-07-09, from `https://www.youtube.com/watch?v=rOYNujm80uU`

Burnham, A. K. (2017). *Advances needed for kinetic models of vitrinite reflectance* (Tech. Rep.). Technical Report, December 2017, Stanford University.

Cacace, M., Bayer, U., Marotta, A. & Lempp, C. (2008). Driving mechanisms for basin formation and evolution.

Cant-Chapa, A. & Ortuo-Maldonado, E. (2003). The tithonian (upper jurassic) edzna formation, an important hydrocarbon reservoir of the campeche shelf, gulf of mexico.

Cantu-Chapa, A. (2009). Upper jurassic stratigraphy (oxfordian and kimmeridgian) in petroleum wells of campeche shelf, gulf of mexico.

Cedeño, A., Rojo, L. A., Cardozo, N., Centeno, L. & Escalona, A. (2019). The impact of salt tectonics on the thermal evolution and the petroleum system of confined rift basins: insights from basin modeling of the nordkapp basin, norwegian barents sea. *Geosciences*, *9*(7), 316.

Čermák, V. & Rybach, L. (1982). Thermal conductivity and specific heat of minerals and rocks. *Landolt-Börnstein: Numerical Data and Functional Relationships in Science and Technology, New Series, Group V (Geophysics and Space Research), Volume Ia,(Physical Properties of Rocks), edited by G. Angenheister, Springer, Berlin-Heidelberg*, 305–343.

Cho, D. & Nordin, D. (2014). How much can I stretch and squeeze? *Recorder*, *39*(10).

Chopra, S. & Marfurt, K. (2014). *Autotracking your way to success.* Retrieved 2021-07-30, from `https://explorer.aapg.org/story/articleid/13226/autotracking-your-way-to-success`

Christeson, G., Van Avendonk, H., Norton, I., Snedden, J., Eddy, D., Karner, G. & Johnson, C. (2014). Deep crustal structure in the eastern gulf of mexico. *Journal of Geophysical Research: Solid Earth*, *119*(9), 6782–6801.

Clegg, H., Wilkes, H., Oldenburg, T., Santamaría-orozco, D. & Horsfield, B. (1998). Influence of maturity on carbazole and benzocarbazole distributions in crude oils and source rocks from the sonda de campeche, gulf of mexico. *Organic Geochemistry*, *29*(1-3), 183–194.

Cohen, K., Harper, D., Gibbard, P. & Fan, J.-X. (2021). ICS international chronostratigraphic chart 2021/05. *International Commission on Stratigraphy, IUGS*.

Cole, G., Requejo, R., DeVay, J., Yu, A., Peel, F., Taylor, C., ... Brown, S. (2001). The deep water gom petroleum system: Insights from piston coring defining seepage, anomalies, and background. In *Proceedings of the 21st annual gcs-sepm foundation research conference–petroleum systems of deep-water basins: Global and gulf of mexico experience. sepm, houston, tx.*

Cole, G., Requejo, R., Yu, A., DeVay, J., Taylor, C., Dougherty, P., ... others (1999). The geochemical and basin modeling aspects of the jurassic to lower cretaceous sourced petroleum system, deepwater to ultra-deepwater gulf of mexico, offshore louisiana: 3rd amgp. *AAPG, Extended Abstracts*, *1*(8).

Comisión Nacional de Hidrocarburos. (2019). *Prospective resources of mexico: Perdido area, mexican ridges and saline basin, deepwater gulf of mexico.* Retrieved 2021-06-04, from `https://www.gob.mx/cms/uploads/attachment/file/527025/Deepwater_Prospective_Resources_of_Mexico_Publishing_2019_DGEPP_low.pdf`

Davison, I. (2019). *Presentation: Campeche salt basin, mexico.* Retrieved 2021-06-07, from `https://www.youtube.com/watch?v=GRlBEImG-mc` (The Chicxulub event can be seen numerically modelled and visualized starting 28:00.)

Davison, I., Pindell, J. & Hull, J. (2021). *The basins, orogens and evolution of the southern gulf of mexico and northern caribbean.* Geological Society of London.

Degen, D., Cacace, M., Spooner, C., Scheck-Wenderoth, M. & Wellmann, F. (2021). Benefits of global sensitivity analysis and reduced order modeling for basin-scale process simulations. In *Egu general assembly conference abstracts* (pp. EGU21–7036).

Degen, D., Veroy, K., Cacace, M., Scheck-Wenderoth, M. & Wellmann, F. (2020). How well do we know our models? In *Egu general assembly conference abstracts* (p. 10482).

Dow, W. G. (1977). Kerogen studies and geological interpretations. *Journal of geochemical exploration*, *7*, 79–99.

Drake, W. R., Longman, M. W. & Moses, A. (2018). Assessment of the woodford shale petroleum system within a deep subbasin on the central basin platform, permian basin. *AAPG Article*, 1–25.

Dumont, A. (2015). Global sensitivity analysis and monte carlo analysis of swiss design method applied to flexible pavements.

Elison, P. (2015). *Influence of uncertainty in thermal conductivity on thermal basin modelling* (Unpublished master's thesis). IDEA League, Faculty of Georesources and Material Engineering, RWTH Aachen.

English, J. M. & Johnston, S. T. (2004). The laramide orogeny: What were the driving forces? *International Geology Review*, *46*(9), 833–838.

Fryklund, B. & Stark, P. (2020). Super basins—new paradigm for oil and gas supply. *AAPG Bulletin*, *104*(12), 2507–2519.

Fuchs, S., Schütz, F., Förster, H.-J. & Förster, A. (2013). Evaluation of common mixing models for calculating bulk thermal conductivity of sedimentary rocks: correction charts and new conversion equations. *Geothermics*, *47*, 40–52.

Gardner, G., Gardner, L. & Gregory, A. (1974). Formation velocity and density—the diagnostic basics for stratigraphic traps. *Geophysics*, *39*(6), 770–780.

Garduno, D. (2020). *Zama: A potential success story in mexico.* Retrieved 2021-07-19, from `https://ihsmarkit.com/research-analysis/zama-a-potential-success-story-in-mexico.html`

Grajales-Nishimura, J., Murillo-Muetn, G., Rosales-Domnguez, C., Cedillo-Pardo, E. & Garca-Hernndez, J. (2003). Heterogeneity of lithoclast composition in the deep-water carbonate breccias of the k/t boundary sedimentary succession, southeastern mexico and offshore campeche.

Hales, A. L. (1969). Crustal and upper mantle structure in the region of the gulf of mexico. *Boletín de la Sociedad Geológica Mexicana*, 63–70.

Hamza, V. & Vieira, F. (2012). Global distribution of the lithosphere-asthenosphere boundary: a new look. *Solid Earth*, *3*(2), 199–212.

Hantschel, T. & Kauerauf, A. I. (2009). *Fundamentals of basin and petroleum systems modeling.* Springer Science & Business Media.

Hartmann, A., Rath, V. & Clauser, C. (2005). Thermal conductivity from core and well log data. *International Journal of Rock Mechanics and Mining Sciences*, *42*(7-8), 1042–1055.

He, Z. (2016). Migration lag–what is it and how it affects charge risk and fluid properties. In *Aapg hedberg conference, the future of basin and petroleum systems modeling*.

Horner, D. R. (1951). Pressure build-up in wells. In *3rd world petroleum congress*.

Hudec, M. R. & Norton, I. O. (2019). Upper jurassic structure and evolution of the yucatán and campeche subbasins, southern gulf of mexico. *AAPG Bulletin*, *103*(5), 1133–1151.

Hudec, M. R., Norton, I. O., Jackson, M. P. & Peel, F. J. (2013). Jurassic evolution of the gulf of mexico salt basin. *AAPG bulletin*, *97*(10), 1683–1710.

Iglesias, A., Atienza, V. C., Shapiro, N., Singh, S. & Pacheco, J. (2001). Crustal structure of south-central mexico estimated from the inversion of surface-wave dispersion curves using genetic and simulated annealing algorithms. *Geofísica Internacional*, *40*(3), 181–190.

Issler, D., McQueen, H. & Beaumont, C. (1989). Thermal and isostatic consequences of simple shear extension of the continental lithosphere. *Earth and planetary science letters*, *91*(3-4), 341–358.

Jackson, M. P. & Talbot, C. J. (1986). External shapes, strain rates, and dynamics of salt structures. *Geological Society of America Bulletin*, *97*(3), 305–323.

Jarvie, D. M. & Smyth, J. (2016). *Upper jurassic, tampico-misantla basin, onshore mexico: Unconventional resource potential.* Retrieved 2021-06-11, from `https://www.searchanddiscovery.com/pdfz/documents/2016/80558jarvie/ndx_jarvie.pdf.html`

Jarvis, G. T. & McKenzie, D. P. (1980). Sedimentary basin formation with finite extension rates. *Earth and Planetary science letters*, *48*(1), 42–52.

Jaupart, C., Mareschal, J.-C. & Iarotsky, L. (2016). Radiogenic heat production in the continental crust. *Lithos*, *262*, 398–427.

Kneller, E. A. & Johnson, C. A. (2011). Plate kinematics of the gulf of mexico based on integrated observations from the central and south atlantic.

Littke, R., Bayer, U., Gajewski, D. & Nelskamp, S. (2008). *Dynamics of complex intracontinental basins: the central european basin system.* Springer Science & Business Media.

Lucas, S. G. (2021). Biostratigraphy. In *Encyclopedia of geology (second edition)* (Vol. 3, p. 89-95). Elsevier Inc.

Magoon, L. B. & Dow, W. G. (1994). The petroleum system: chapter 1: Part i. introduction.

Magri, F., Littke, R., Rodon, S., Bayer, U. & Urai, J. (2008). Temperature fields, petroleum maturation and fluid flow in the vicinity of salt domes. *Dynamics of Complex Intracontinental Basins: The Central European Basin System*, 323–344.

McKenna, T. E. & Sharp, J. M. (1998). Radiogenic heat production in sendimentary rocks of the gulf of mexico basin, south texas. *AAPG bulletin*, *82*(3), 484–496.

McKenzie, D. (1978). Some remarks on the development of sedimentary basins. *Earth and Planetary science letters*, *40*(1), 25–32.

Mello, U. T., Karner, G. D. & Anderson, R. N. (1995). Role of salt in restraining the maturation of subsalt source rocks. *Marine and Petroleum Geology*, *12*(7), 697–716.

Mitra, S., Duran Gonzalez, J. A., Hernandez, J. G., Garcia, S. H. & Banerjee, S. (2006). Structural geometry and evolution of the ku, zaap, and maloob structures, campeche bay, mexico. *AAPG bulletin*, *90*(10), 1565–1584.

Mottaghy, D., Pechnig, R. & Vogt, C. (2011). The geothermal project den haag: 3d numerical models for temperature prediction and reservoir simulation. *Geothermics*, *40*(3), 199–210.

Nguyen, L. C. & Mann, P. (2016). Gravity and magnetic constraints on the jurassic opening of the oceanic gulf of mexico and the location and tectonic history of the western main transform fault along the eastern continental margin of mexico. *Interpretation*, *4*(1), SC23–SC33.

Nielsen, S., Clausen, O. & McGregor, E. (2017). Basin% ro: a vitrinite reflectance model derived from basin and laboratory data. *Basin Research*, *29*, 515–536.

Orr, W. L. (1986). Kerogen/asphaltene/sulfur relationships in sulfur-rich monterey oils. *Organic geochemistry*, *10*(1-3), 499–516.

Oviedo-Perez, A. (1996). *Evolución neógena de las cuencas terciarias del sureste* (Unpublished doctoral dissertation). Master's thesis, Universidad Nacional Autonoma de Mexico, Mexico City, Mexico.

Padilla y Sánchez, R. (2014). *Tectonics of eastern mexico–gulf of mexico and its hydrocarbon potential: Aapg search and discovery article 10622.* Retrieved 2021-06-06, from `https://www.searchanddiscovery.com/pdfz/documents/2014/10622padilla/ndx_padilla.pdf.html`

Padilla y Sánchez, R. J. (2007). Evolución geológica del sureste mexicano desde el mesozoico al presente en el contexto regional del golfo de méxico. *Boletín de la Sociedad Geológica Mexicana*, *59*(1), 19–42.

Pepper, A. S. & Corvi, P. J. (1995). Simple kinetic models of petroleum formation. part i: oil and gas generation from kerogen. *Marine and petroleum geology*, *12*(3), 291–319.

Perez Gutierrez, C. M. (2007). *Structural kinematics and salt evolution in the "kuzam" area ; offshore southeast gulf of mexico : implications for petroleum prospectivity* (Master's thesis, Colorado School of Mines, Department of Geology and Geological Engineering). Retrieved 2021-06-07, from `https://www.semanticscholar.org/paper/Structural-kinematics-and-salt-evolution-in-the-%3B-%3A-Gutierrez-Miguel/beb0b8ff1dab282b37f8dfe8d6378bddcdf662ed#extracted`

Peters, K. E., Burnham, A. K., Walters, C. C. & Schenk, O. (2018). Guidelines for kinetic input to petroleum system models from open-system pyrolysis. *Marine and Petroleum Geology*, *92*, 979–986.

Pindell, J., Kennan, L., Watts, T., Roberts, H., Rosen, N., Fillon, R. & Anderson, J. (2003). Asymmetric rifting and the northern gulf of mexico suprasalt platform: Implications for the initial depositional setting of texas-louisiana tertiary clastic systems. In *Shelf-margin deltas and linked down slope petroleum systems: Global significance and future exploration potential: 23rd annual gulf coast section-sepm foundation bob f. perkins research conference, houston, texas* (pp. 135–138).

Pindell, J. & Miranda, E. (2011). Linked kinematic histories of the macuspana, akal-reforma, comalcalco, and deepwater campeche basin tectonic elements, southern gulf of mexico.

Pindell, J., Weber, B., Elrich, W.-H., Cossey, S., Bitter, M., Molina, R., . . . Erlich, R. (2019). Strontium isotope dating of evaporites and the breakup of the gulf of mexico and proto-caribbean seaway. In *2019 aapg annual convention and exhibition:*.

Pindell, J. L. (1993). Regional synopsis of gulf of mexico and caribbean evolution. In *Mesozoic and early cenoizoic development of the gulf of mexico and caribbean region: A context for hydrocarbon exploration, gulf coast section, semp foundation 13th annual research conference: Houston, texas, semp (society for sedimentary geology) foundation, 1993* (pp. 251–274).

Pindell, J. L. & Kennan, L. (2009). Tectonic evolution of the gulf of mexico, caribbean and northern south america in the mantle reference frame: an update. *Geological Society, London, Special Publications*, *328*(1), 1–55.

Renne, P. R., Deino, A. L., Hilgen, F. J., Kuiper, K. F., Mark, D. F., Mitchell, W. S., . . . Smit, J. (2013). Time scales of critical events around the cretaceous-paleogene boundary. *Science*, *339*(6120), 684–687.

Rodríguez-Domínguez, M., Pérez-Campos, X., Montealegre-Cázares, C., Clayton, R. W. & Cabral-Cano, E. (2019). Crustal structure variations in south-central mexico from receiver functions. *Geophysical Journal International*, *219*(3), 2174–2186.

Rodríguez del Ángel, U. d. J. (2012). *Structural modelling of salt structures in bolol area and implications in hydrocarbon prospectivity* (Unpublished master's thesis). Royal Holloway University of London, Department of Earth Sciences.

Rosales-Rodriguez, J., Lee Bandy, W. & Centeno-Garcia, E. (2014). Depth of the base of the magnetic source and thermal structure of the gulf of mexico. *Revista mexicana de ciencias geológicas*, *31*(2), 190–202.

Royden, L. & Keen, C. (1980). Rifting process and thermal evolution of the continental margin of eastern canada determined from subsidence curves. *Earth and Planetary Science Letters*, *51*(2), 343–361.

Rybach, L. (1973). *Wärmeproduktionsbestimmungen an gesteinen der schweizer alpen*. Kümmerly & Frey, Geograph. Verlag.

Salvador, A. (1987). Late triassic-jurassic paleogeography and origin of gulf of mexico basin. *AAPG Bulletin*, *71*(4), 419–451.

Salvador, A. (1991). The gulf of mexico basin: Geological society of america, the geology of north america. *v.J*, 1–12.

Sanford, J. C., Snedden, J. W. & Gulick, S. P. (2016). The cretaceous-paleogene boundary deposit in the gulf of mexico: Large-scale oceanic basin response to the chicxulub impact. *Journal of Geophysical Research: Solid Earth*, *121*(3), 1240–1261.

Santamaría-Orozco, D., Horsfield, B., Di Primio, R. & Welte, D. (1998). Influence of maturity on distributions of benzo-and dibenzothiophenes in tithonian source rocks and crude oils, sonda de campeche, mexico. *Organic Geochemistry*, *28*(7-8), 423–439.

Santamaria Orozco, D. M. (2000). *Organic geochemistry of tithonian source rocks and associated oils from the sonda de campeche, mexico* (Tech. Rep.). Publikationen vor 2000.

Schenk, O., Bird, K., Peters, K. & Burnham, A. (2017). Sensitivity analysis of thermal maturation of alaska north slope source rocks based on various vitrinite reflectance models. *AAPG Search and discovery article*, *42167*.

Schenk, O., Peters, K. & Burnham, A. (2017). Evaluation of alternatives to easy% ro for calibration of basin and petroleum system models. In *79th eage conference and exhibition 2017* (Vol. 2017, pp. 1–5).

Schneider, F., Potdevin, J., Wolf, S. & Faille, I. (1996). Mechanical and chemical compaction model for sedimentary basin simulators. *Tectonophysics*, *263*(1-4), 307–317.

Sekiguchi, K. (1984). A method for determining terrestrial heat flow in oil basinal areas. *Tectonophysics*, *103*(1-4), 67–79.

Shann, M. V. (2021). The sureste basin of mexico: its framework, future oil exploration opportunities and key challenges ahead. *Geological Society, London, Special Publications*, *504*(1), 119–146.

Shann, M. V., Vazquez-Reyes, K., Ali, H. M. & Horbury, A. D. (2020). The sureste super basin of southern mexico. *AAPG Bulletin*, *104*(12), 2643–2700.

Sharqawy, M. H., Lienhard, J. H. & Zubair, S. M. (2010). Thermophysical properties of seawater: a review of existing correlations and data. *Desalination and water Treatment*, *16*(1-3), 354–380.

Smith, R. B., Eaton, G. P. et al. (1978). *Cenozoic tectonics and regional geophysics of the western cordillera* (Vol. 152). Geological Society of America.

Snedden, J. W. & Galloway, W. E. (2019). *The gulf of mexico sedimentary basin: Depositional evolution and petroleum applications*. Cambridge University Press.

Snedden, J. W., Norton, I. O., Christeson, G. L. & Sanford, J. C. (2014). Interaction of deepwater deposition and aa mid-ocean spreading center, eastern gulf of mexico basin, usa.

Snyder, F. & Ysaccis, R. (2018). New offshore exploration opportunities within the salina del istmo basin, mexico. In *Aapg ace 2018*.

Sobota, T. (2014). Fourier's law of heat conduction, encyclopedia of thermal stresses (ed. r. hetnarski). *Springer*, 1769–1778.

Steckler, M. & Watts, A. (1978). Subsidence of the atlantic-type continental margin off new york. *Earth and planetary science letters*, *41*(1), 1–13.

Sweeney, J. J. & Burnham, A. K. (1990). Evaluation of a simple model of vitrinite reflectance based on chemical kinetics. *AAPG bulletin*, *74*(10), 1559–1570.

Teichmüller, M. (1989). The genesis of coal from the viewpoint of coal petrology. *International Journal of Coal Geology*, *12*(1-4), 1–87.

Touloukian, Y. S., Powell, R., Ho, C. & Klemens, P. (1970). *Thermophysical properties of matter-the tprc data series. volume 1. thermal conductivity-metallic elements and alloys* (Tech. Rep.). Thermophysical and Electronic Properties Information Analysis Center.

Valois, V. M. C., Valdes, M. d. L. C., Placencia, J. I. J., Ortiz, I. A., Jurado, M. M., Yanez, R. V., . . . Ghosh, S. (2009). A new multidisciplinary focus in the study of the tertiary plays in the sureste basin, mexico.

Wainwright, H. M., Finsterle, S., Jung, Y., Zhou, Q. & Birkholzer, J. T. (2014). Making sense of global sensitivity analyses. *Computers & Geosciences*, *65*, 84–94.

Walderhaug, O. (2000). Modeling quartz cementation and porosity in middle jurassic brent group sandstones of the kvitebjørn field, northern north sea. *AAPG bulletin*, *84*(9), 1325–1339.

Waples, D. & Tobey, M. H. (2017). Like space and time, transformation ratio is curved.

Wernicke, B. (1985). Uniform-sense normal simple shear of the continental lithosphere. *Canadian Journal of Earth Sciences*, *22*(1), 108–125.

Whaley, J. (2019). *Petroleum geology: What is a super basin?* Retrieved 2021-06-04, from `https://www.geoexpro.com/articles/2019/11/petroleum-geology-what-is-a-super-basin`

Winker, C. D. & Buffler, R. T. (1988). Paleogeographic evolution of early deep-water gulf of mexico and margins, jurassic to middle cretaceous (comanchean). *AAPG bulletin*, *72*(3), 318–346.

Wygrala, B. (1989). *Integrated study of an oil field in the southern po basin, northern italy* (Tech. Rep.). Publikationen vor 2000.

Yu, Z., Lerche, I. & Lowrie, A. (1992). Thermal impact of salt: Simulation of thermal anomalies in the gulf of mexico. *Pure and Applied Geophysics*, *138*(2), 181–192.

# Appendix A - Paleogeographic Maps
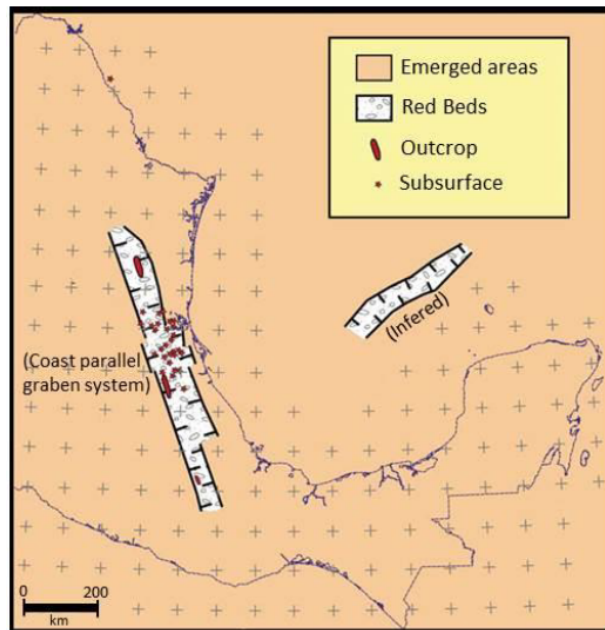
Figure 1: **Paleogeographic map for the J50 sequence.**
Source: Perez Gutierrez (2007); modified originally from R. J. Padilla y Sánchez (2007).
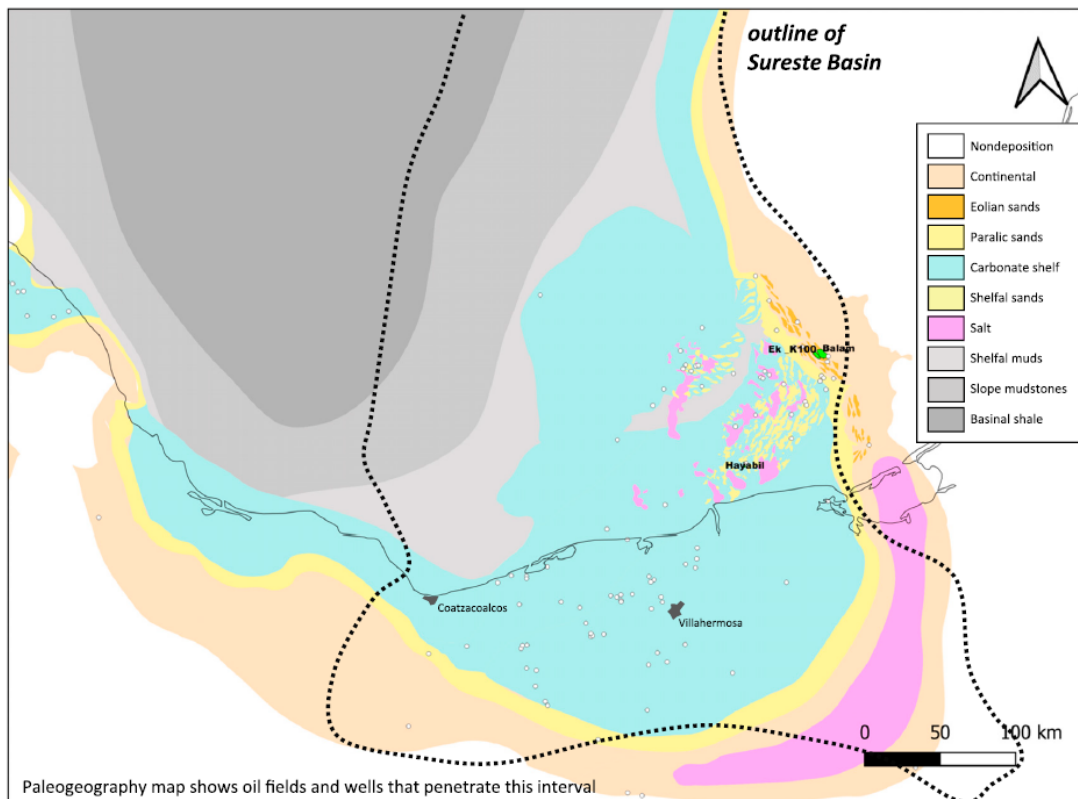
Figure 2: **Paleogeographic map for the J80 sequence.**
Source: Shann et al. (2020).
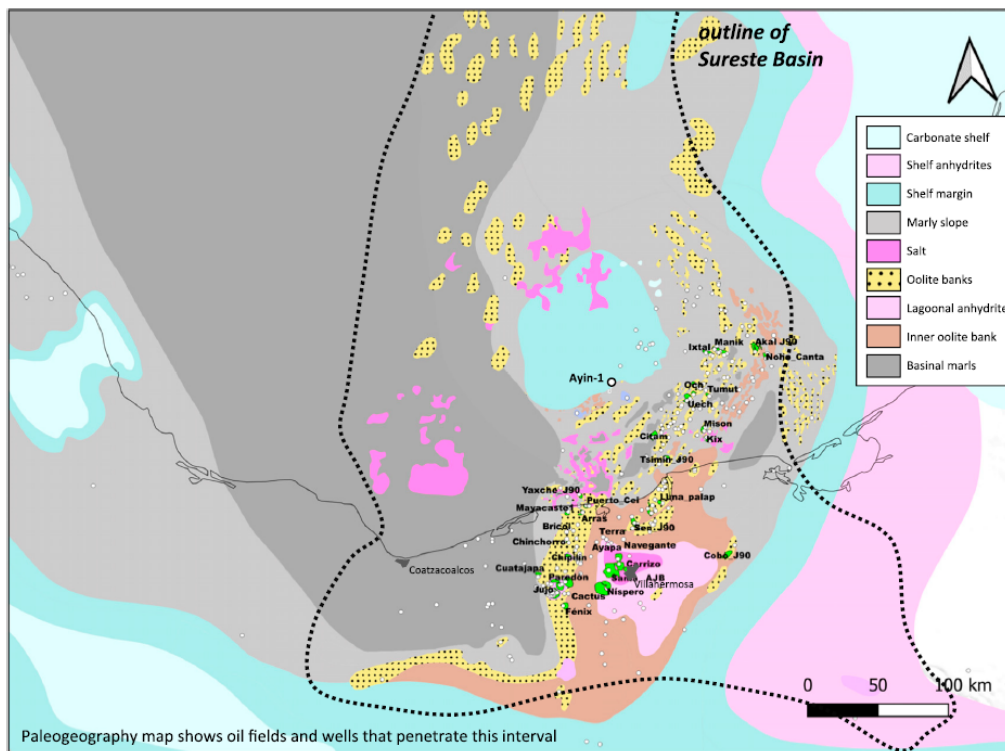
Figure 3: **Paleogeographic map for the J90 sequence.**
Source: Shann et al. (2020).
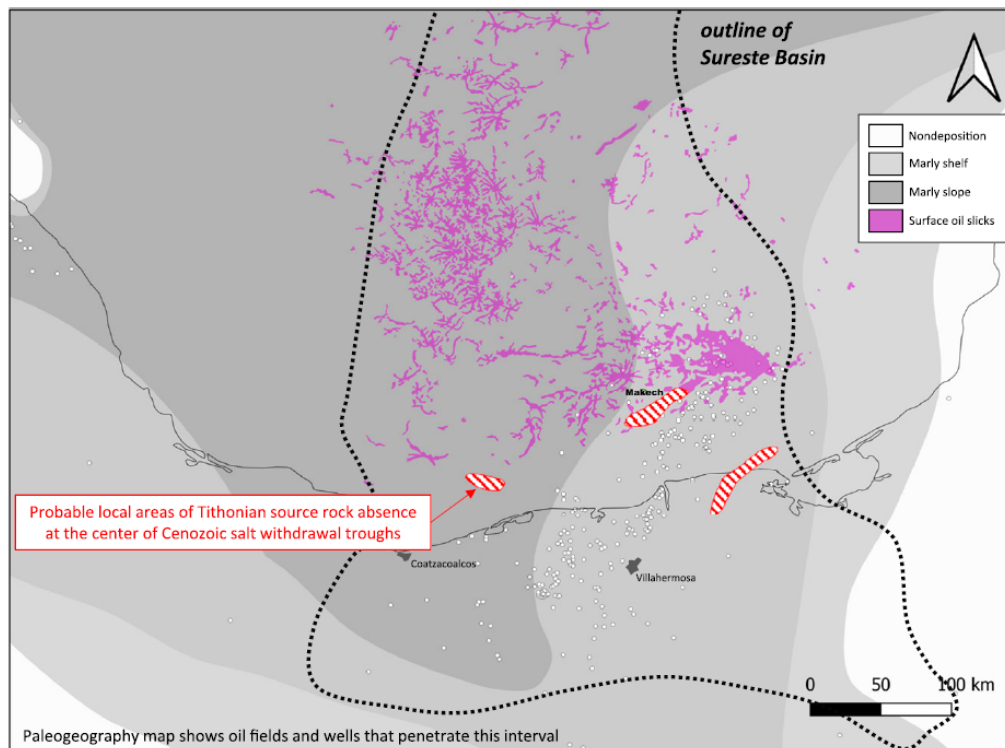
Figure 4: **Paleogeographic map for the J100 sequence.**
Source: Shann et al. (2020).
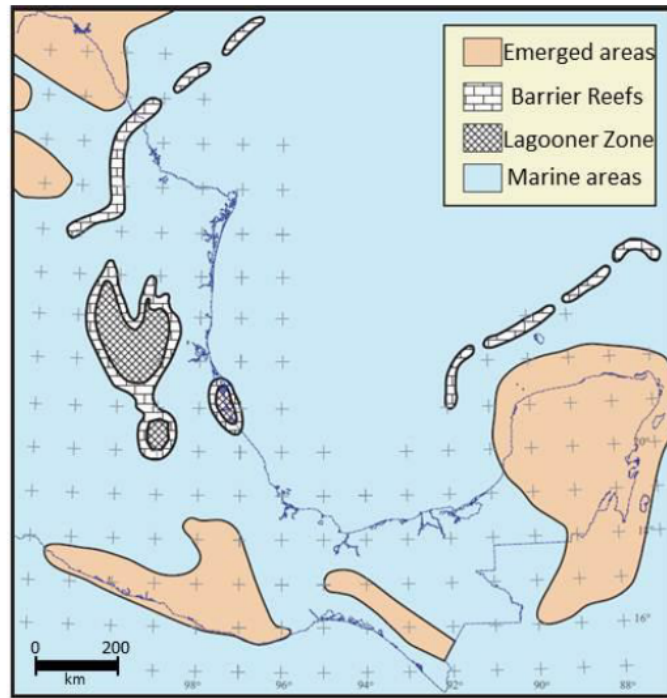
Figure 5: **Paleogeographic map for the K50 sequence.**
Source: Perez Gutierrez (2007); modified originally from R. J. Padilla y Sánchez (2007).
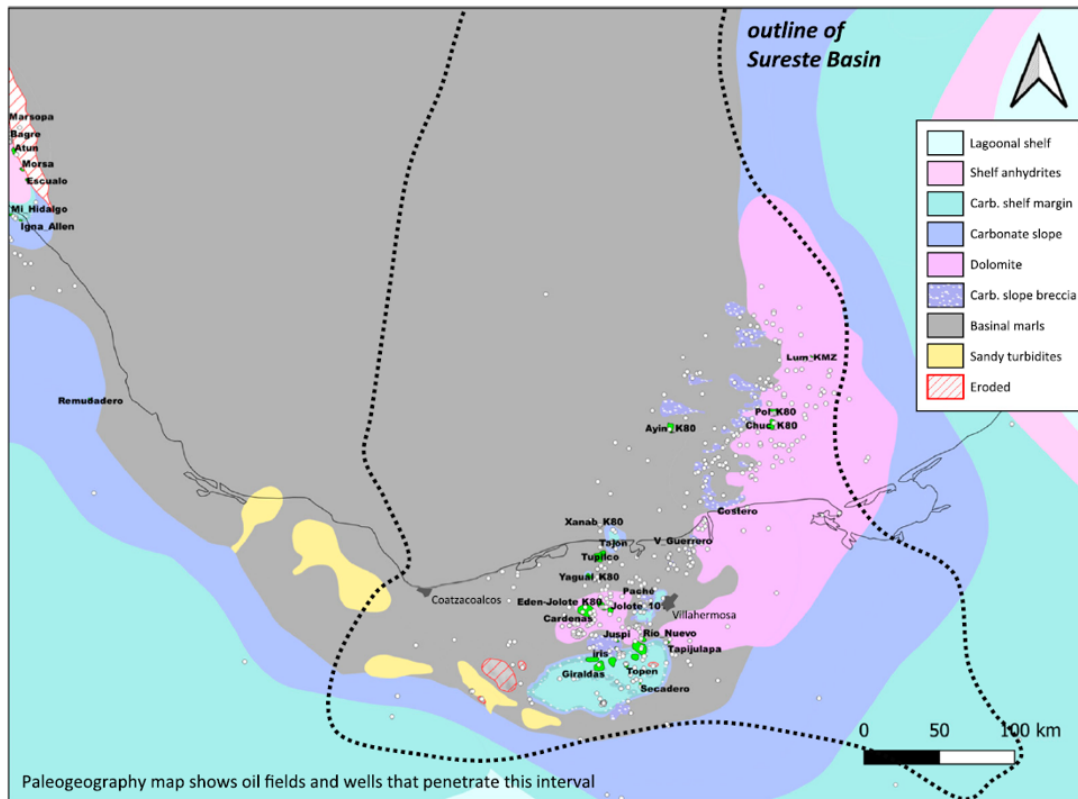
Figure 6: **Paleogeographic map for the K80 sequence.**
Source: Shann et al. (2020).

REFERENCES   79
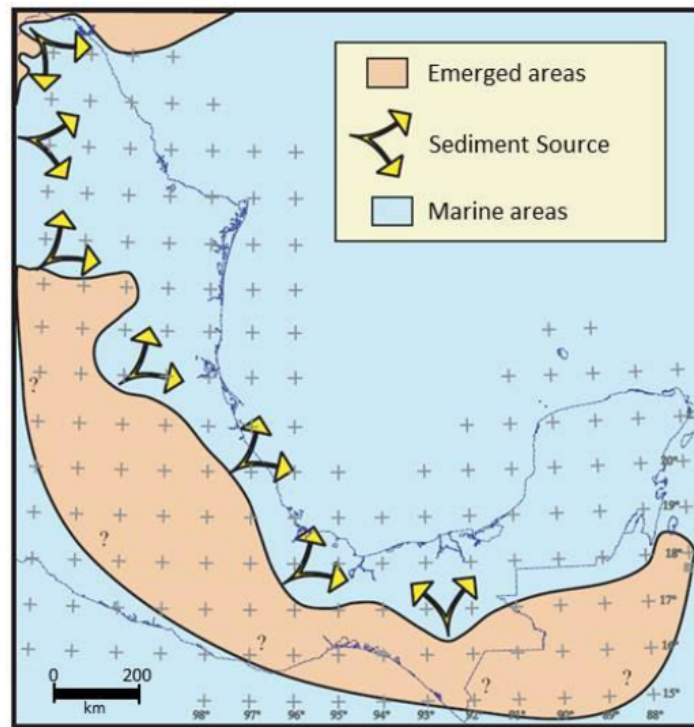
Figure 7: **Paleogeographic map for the K100 sequence.**
Source: Perez Gutierrez (2007); modified originally from R. J. Padilla y Sánchez (2007).
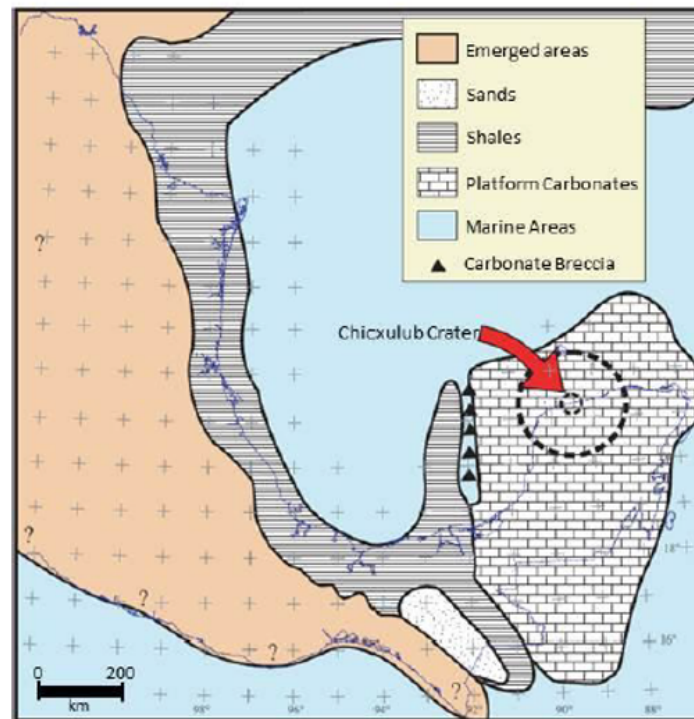
Figure 8: **Paleogeographic map for the T20 sequence.**
Source: Perez Gutierrez (2007); modified originally from R. J. Padilla y Sánchez (2007).
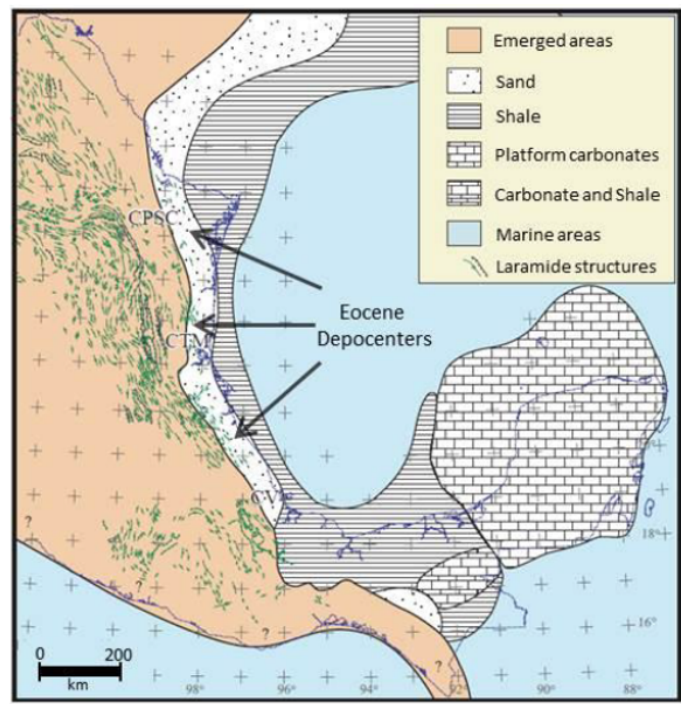
Figure 9: **Paleogeographic map for the T30 sequence.**
Source: Perez Gutierrez (2007); modified originally from R. J. Padilla y Sánchez (2007).
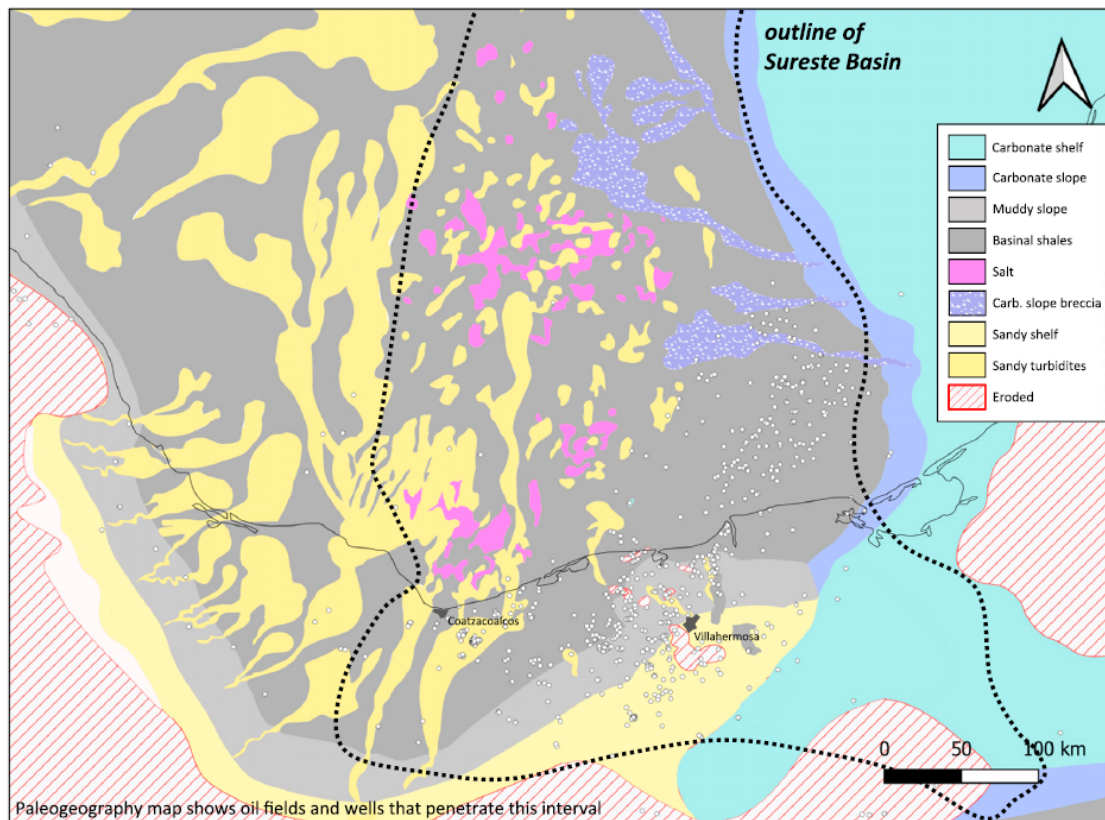
Figure 10: **Paleogeographic map for the T40 sequence.**
Source: Shann et al. (2020).
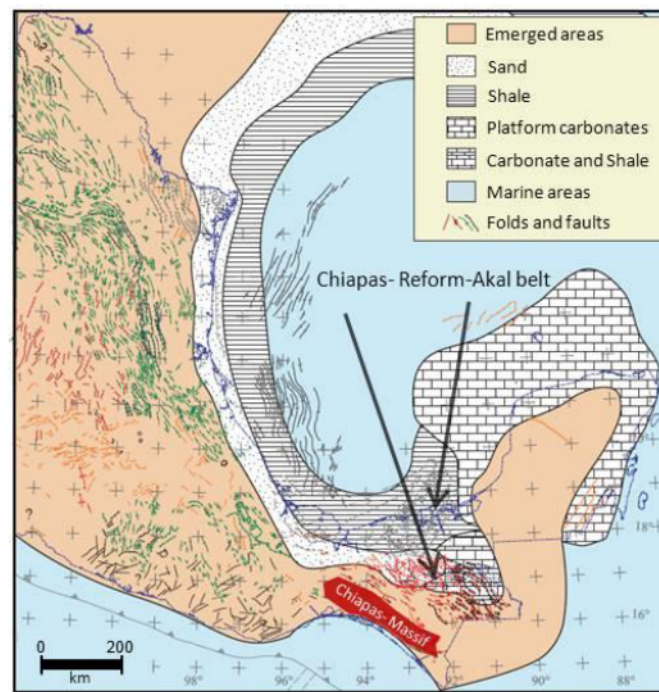
Figure 11: **Paleogeographic map for the T50 sequence.**
Source: Perez Gutierrez (2007); modified originally from R. J. Padilla y Sánchez (2007).

Appendix B - Maturity Model Parameters
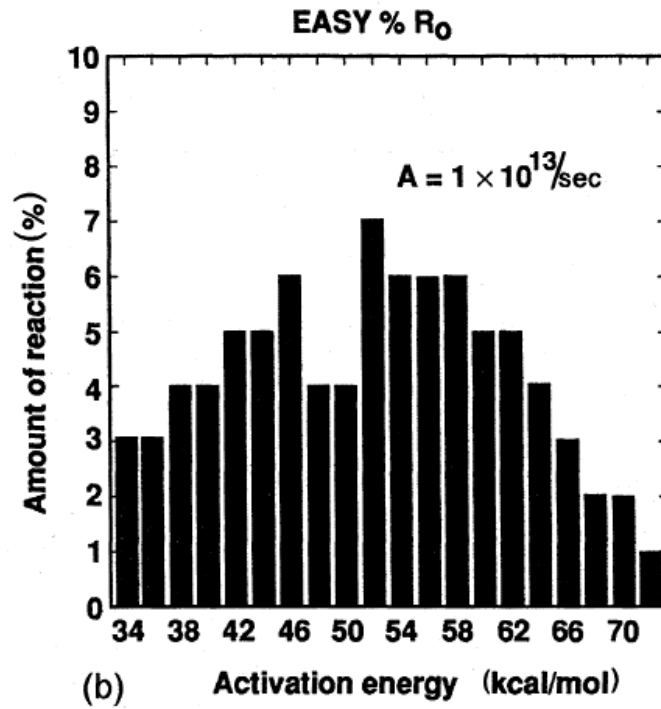
Figure 12: **Kinetic Parameters E_a and A for the Easy%R$_0$ maturity model.** Read Sweeney & Burnham (1990) for more details.
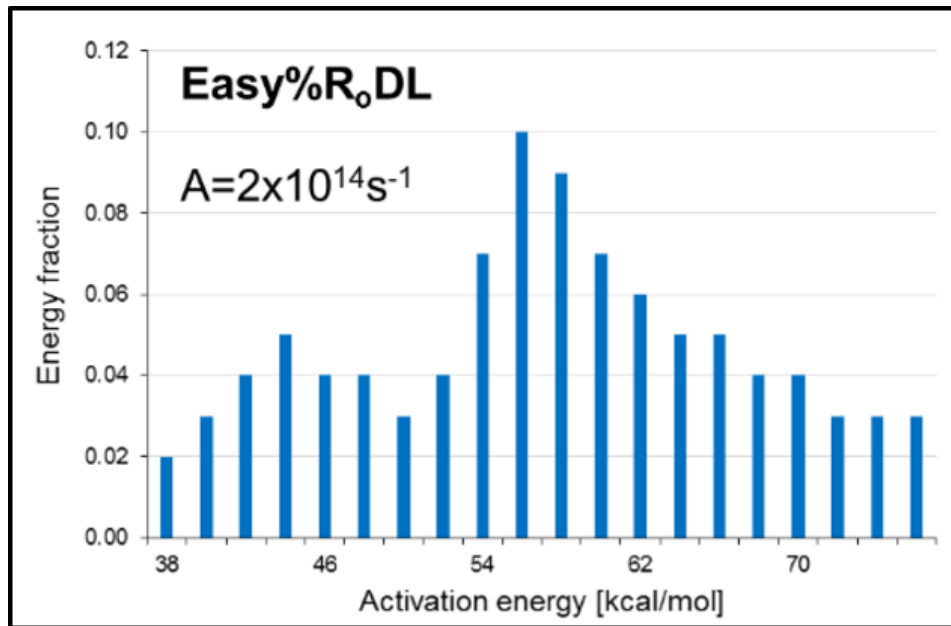
Figure 13: **Kinetic Parameters E_a and A for the Easy%R$_0$DL maturity model.** See A. Burnham (2016) and Schenk, Peters & Burnham (2017) for more details.

Appendix C - Further Supporting Figures
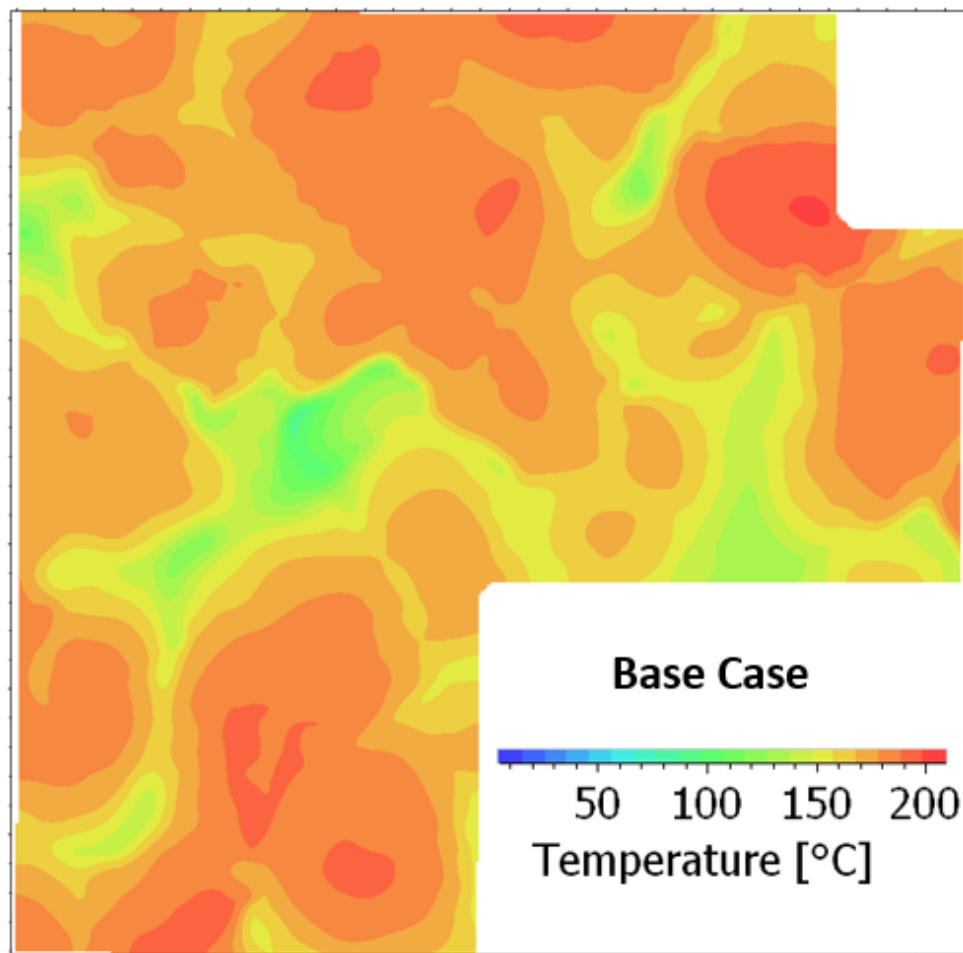
Figure 14: **Present-day Temperature Distribution at the base of the J100 source rock the base case.**
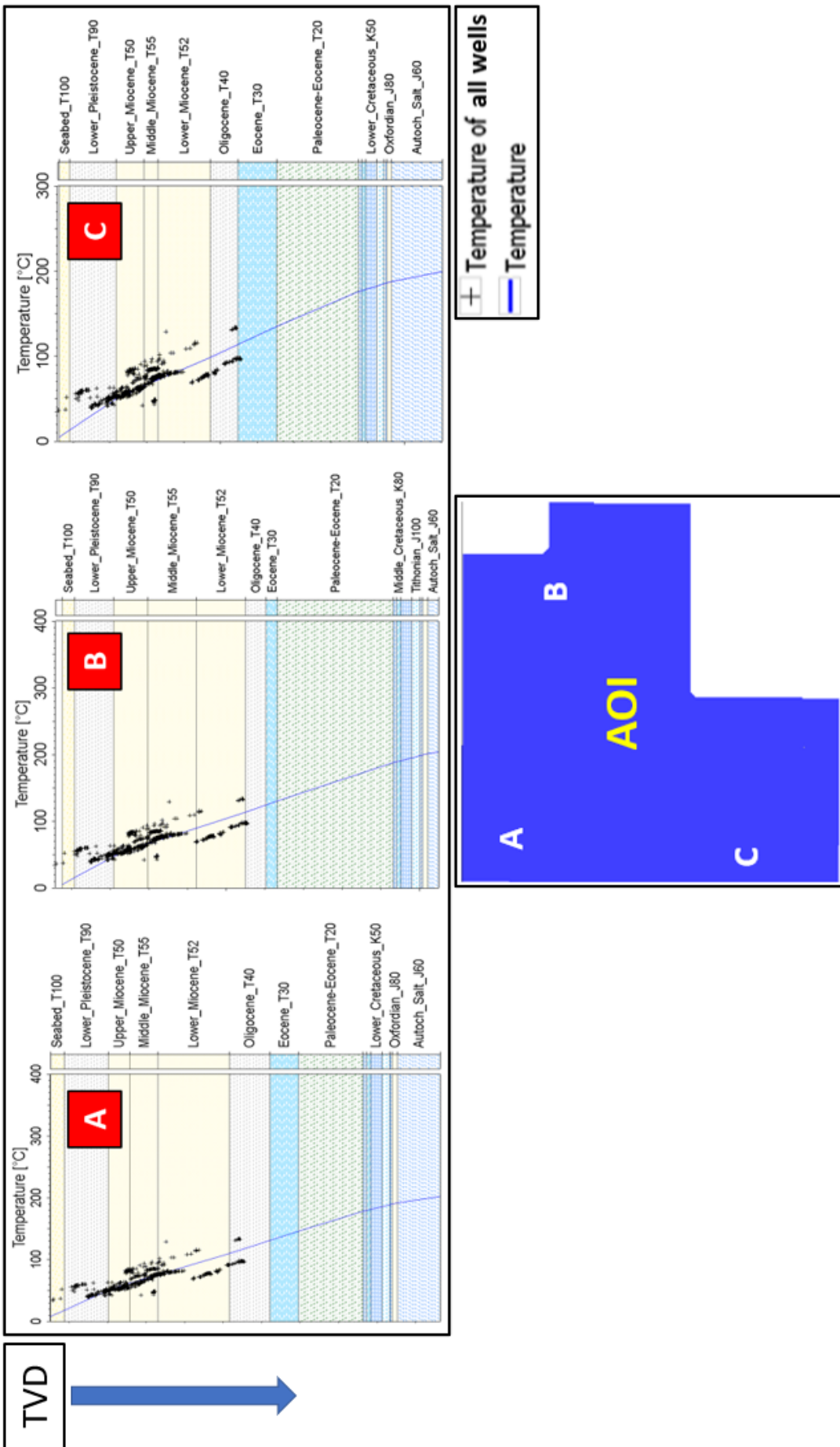
Figure 15: **Present-day temperature-depth trends at three locations across the AOI shown to match reasonably well with regional temperature data from all available wells.**

Note: The depth values have been hidden due to confidentiality requirements of Wintershall Dea GmbH and partners.
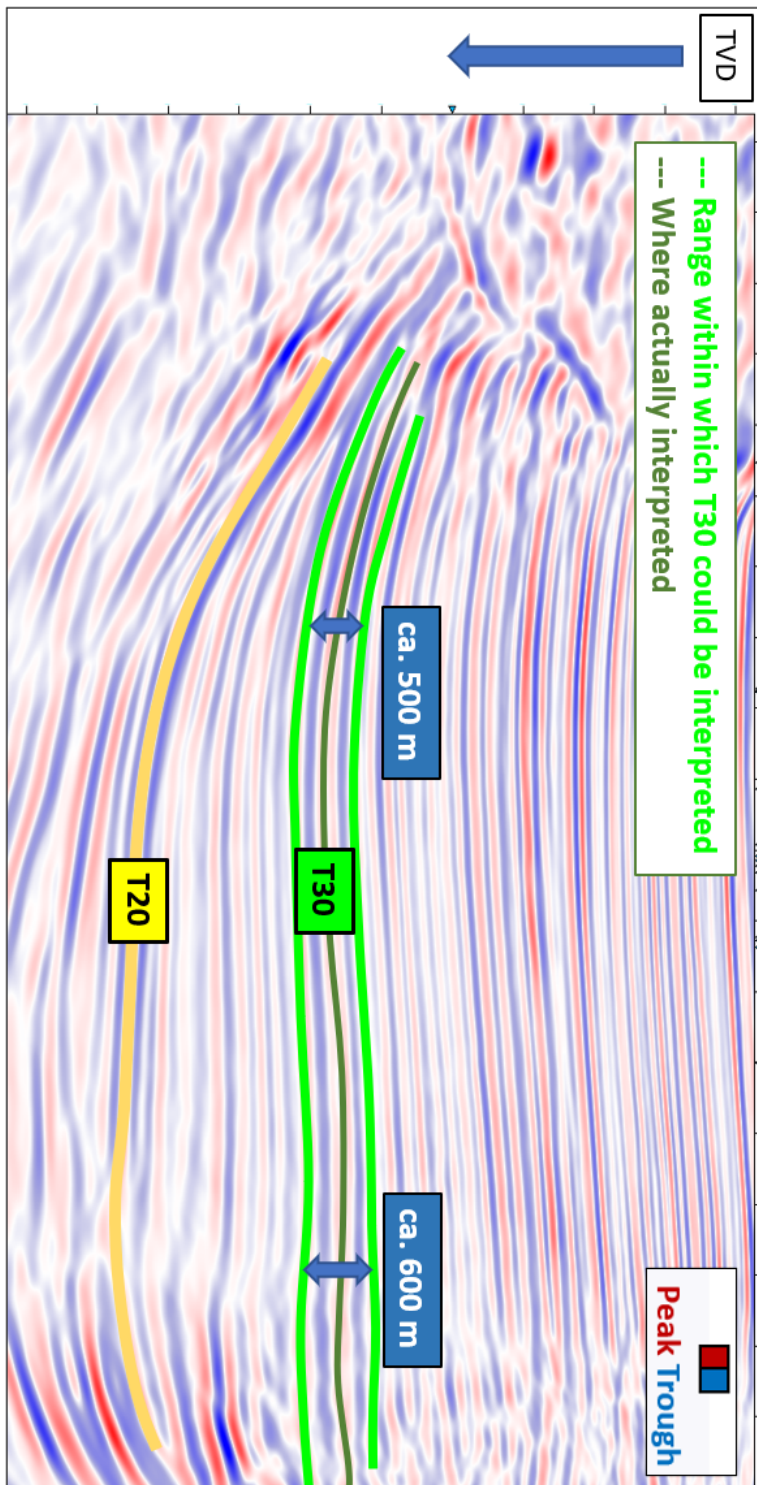
Figure 16: **Example of possible interpretations for the top of T30 horizon based on the identification of the end of the Laramide-related thickness variation.**
Note: The depth values have been hidden due to confidentiality requirements of Wintershall Dea GmbH and partners.